Implications and Limitations of Tremor as a Proxy for Slow Slip

Kelley Hall

A dissertation

submitted in partial fulfillment of the

requirements for the degree of

Doctor of Philosophy

University of Washington

2020

Reading Committee:

David Schmidt, Co-chair

Heidi Houston, Co-chair

Ken Creager

Program Authorized to Offer Degree:

Earth and Space Sciences

University of Washington

Abstract

Implications and Limitations of Tremor as a Proxy for Slow Slip

Kelley Hall

Chair of the Supervisory Committee:
Professor David Schmidt
Department of Earth and Space Sciences
Professor Heidi Houston
Department of Earth and Space Sciences

This thesis seeks to integrate geodetic and seismic observations to explore the relationship between tremor and slow slip on subduction zones. In particular, I evaluate the one-to-one relationship of tremor and slip in space and time, and test various hypotheses that describe their interaction and scaling. This work adds insight into the state of the Cascadia subduction zone and the slow-slip seismic cycle.

In the first chapter, I use the surface displacements measured by GPS stations to analyze six major episodic tremor and slip (ETS) events from 2007 to 2016 in northern Cascadia and invert for slip on a realistic plate interface. Tremor is typically constrained to a relatively narrow

band along dip that is downdip of the inferred locked megathrust. My results indicate that slow slip extends updip of tremor by about 15 km beneath the Olympic Peninsula. Additionally, I find that along-strike variations in the amount of slow slip updip of tremor correspond to changes in lithology of the overlying crust. In these ETS events, slow slip extends from the downdip portion of the tremorgenic region beyond the updip extent of tremor, although still downdip of the inferred locked megathrust. Slip updip of tremor is a persistent feature of all six ETS events at this along-strike location. Inversions that restrict slip to occur only in regions that generated tremor produced slip distributions with unphysical characteristics and unsustainable concentrations at the updip part of the tremor footprint. Updip slow slip without tremor may suggest that the gap between stress and strength widens updip above the observed limit of tremor. In these ETS events, the regions updip of tremor may undergo ductile failure surrounding potentially tremorgenic patches. A widening gap between stress and strength in the updip direction is consistent with an observed along-dip dependence of LFE occurrence and numerical simulations of slow slip. Alternatively, rheological properties in the region updip of tremor may favor stable slip and not permit seismic slip (i.e. tremor).

In the second chapter, I explore the evolution of slow slip on the Cascadia megathrust during two large ETS events and compare stress changes to the spatial evolution of tremor from PNSN tremor locations. I use displacement time series from GPS stations, along with the Extended Network Inversion Filter to solve for the time-dependent fault slip on the megathrust. The 2010 (Mw 6.8) and 2012 (Mw 6.8) slow slip events propagated northward and southward, respectively, allowing us to assess directional effects on slip behavior. I observe that tremor occurs on the leading edge of propagating slipping regions, well ahead of the highest slip rates, independent of the along-strike propagation direction. Using the tremor distribution to generate synthetic surface displacement data, resolution tests show that the result of peak tremor rates leading peak slip rates is not due to biases introduced by temporal smoothing. Calculated stress changes due to the time-dependent fault slip distributions imply that tremor is sensitive to kPa of stress, consistent with studies of tidally-triggered tremor. Within the resolution of our model, these results are consistent with the hypothesis that significant tremor is triggered by stresses ahead of the highest slip rates. I also observe ongoing slip continuing several days after tremor has passed. Our observations are consistent with some numerical models of tremor patches that suggest that this behavior can be explained by densely packed asperities, which act to widen the length scale of the slip pulse, rather than a narrow slip pulse.

In the third chapter, I explore small slow slip events (SSEs), with Mw < 6.0, and assesses whether fault slip and tremor detections scale linearly. Under the assumption that tremor and slip are spatially and temporally related during slow slip events, I develop a scaling relationship between tremor counts and slip based on known large slow slip events (SSEs) in Cascadia. I use the existing tremor catalog in Cascadia to cluster tremor detections into distinct events that can be scaled into slip distributions. Using this scaling relationship on a clustered tremor catalog, I obtain event magnitudes that range from Mw 4.5 to 6.5. We also find that the larger (Mo > $3*10^{17}$ Nm) clustered events follow a Mo ~ T scaling. This catalog partially fills the long-standing observational gap between seismically detectable events and geodetically detectable events. GPS and strainmeters are used as an independent check of the scaling relationship. Using this clustered catalog as a guide, I identify a patch of repeating events beneath the Olympic Peninsula that produces frequent small SSEs. We stack the daily GPS time series for seven small slow slip events, aligning each record on peak tremor activity. We then estimate the average surface displacement and find the average moment. The GPS-based average moment for events in this patch is Mw 5.5 with peak fault slip reaching 0.6 cm and only 30% of the tremoring area slipping, compared to Mw 5.8 predicted by scaling the number of tremor detections. For further validation of our scaling relationship, I compare the scaled-tremor models to observed strainmeter records. We find that our empirical scaling relationship for large SSEs accurately predicts the strain for several small SSEs.

TABLE OF CONTENTS

LIST OF FIGURES

LIST OF TABLES

ACKNOWLEDGEMENTS

Thank you to my committee for all of your guidance and feedback on this dissertation. All tremor locations come from the Pacific Northwest Seismic Network. GPS time series were processed at the Pacific Northwest Geodetic Array and include data from GPS stations in the Plate Boundary Observatory (PBO). Strainmeter data used in this work also comes from PBO. Thank you to the USGS and the NSF for the financial support for this work; specific grants are noted within each chapter.

DEDICATION

This dissertation is dedicated to my loving family. Whether it was a delicious meal or words of encouragement, I could not have done this without your support. Also thank you to all of my wonderful friends. You have all kept me sane throughout this journey. Lastly, thank you to my committee for your guidance and advice throughout the my doctorate.

Chapter 1. INTRODUCTION

Faults have been shown to accommodate relative plate motions in different ways, from steady aseismic creep to sudden dynamic rupture of a typical earthquake, both of which represent end member modes of fault slip. A typical earthquake slips quickly (>1 km/sec) and generates seismic waves in the elastic medium that radiate out from the fault (Aki & Richards, 2002). Under certain conditions, slip is unable to reach dynamic velocities; instead low-amplitude, low-frequency energy is released, referred to as slow slip phenomena. On the continuum of slip modes, slow-slip phenomena lie somewhere between the stick-slip behavior of typical earthquakes and the steady aseismic creep at plate rate (Peng and Gomberg, 2010). Examples of these slow-slip phenomena include tremor, low-frequency earthquakes, and slow-slip events (SSEs).

Large SSEs release a significant amount of strain, often produce measurable surface displacement observed by GPS stations (Dragert et al., 2004) and range in magnitude from Mw 6.0 to 7.2 (Meade and Loveless, 2009). SSEs have been reported in subduction zones across the world including in southwest Japan (Obara et al., 2004, Kato et al., 2012), Mexico (Kostoglodov et al., 2010), Costa Rica (Outerbridge et al., 2010), Alaska (Fu and Freymueller, 2013), Chile (Kato and Nakagawa, 2014), and New Zealand (Wallace & Beavan, 2010). SSEs are commonly accompanied by episodes of increased tectonic tremor, together referred to as episodic tremor and slow slip or “ETS”. On seismograms, tremor appears as low-amplitude noise with frequencies between 1-5 Hz (Rogers & Dragert, 2003). The tremor signal has an emergent waveform, and can be identified by coherent envelopes across several stations that are up to kilometers apart. Slow slip phenomena, such as SSEs and tremor, occur in the transition zone between the up-dip locked zone and the down-dip creeping zone, and are expected to play a key role in the earthquake cycle of subduction zones (Wech and Creager, 2011).

My research builds on previous findings that have established a relationship between tremor and slow slip. Rogers and Dragert showed in their 2003 paper that there is a large coherent transient signal in GPS records on Vancouver Island that are contemporaneous with increased tremor activity, suggesting some common process or relationship. It has been observed that slow slip and tremor migrate in tandem along several subduction zones at about 7 to 12 km/day in large ETS events (Obara et al., 2004, Wech et al., 2009, Houston et al., 2011). This was further developed by Aguiar et al. (2009), who showed that there is a linear relationship between duration of tremor and moment release rate.

My work seeks to test the limits of tremor as a proxy for slow slip by using geodetic and seismic observations. One well-established theory is that tremor is generated by slow shear slip on the plate interface (Shelly et al., 2006, Ide et al., 2007) and could serve as a proxy for slip during ETS events. It is useful to use a schematic to better understand what each method is measuring and what signals are being measured. In this dissertation, I use the “chocolate chip cookie” model presented by Chestler & Creager (2017b) to illustrate the heterogeneity of the shear zone. For the purposes of this metaphor, we will describe the array of seismically detectable phenomena as brittle failure. In the chocolate chip cookie model, stronger more brittle patches (the chocolate chips) are embedded within ductile matrix (the cookie). Seismometers are sensitive to the brittle failure of the chocolate chips, recorded as tremor or low-frequency earthquakes (LFEs). GPS stations, conversely, capture the aseismic strain release of the surrounding ductile matrix. In the simplest of assumptions, the slipping and deformation of the surrounding ductile matrix causes brittle failure of the tremorgenic patches. Therefore, we would expect that seismic activity is an indication of active slip. The actual nuances of this relationship serve as the motivation for the work presented here.

This dissertation will focus on SSEs in the Cascadia subduction zone, which stretches ~1,000 km from Vancouver Island all the way down to the Mendocino triple junction. The Cascadia subduction zone is a large scale thrust fault that accommodates the subduction of the Juan de Fuca and Gorda plates beneath continental North America. The fault has been shown to host large tsunamigenic earthquakes Mw 8.0-9.0 every 500+ years (Goldfinger et al., 2012), which pose major threats to life and infrastructure along the whole west coast. Cascadia makes an ideal test case for SSE behavior for several reasons: significant long-term instrumentation and numerous well recorded events. In order to compare tremor and slow slip, it is necessary to have seismic and geodetic data sets to compare. For this dissertation, I use Pacific Northwest Seismic Network real-time tremor catalog, which uses the Wech detection method (Wech, 2010) and spans the whole subduction zone. This catalog extends as far back as 2009 in some locations. Additionally, there is an extensive GPS network run by PANGA and UNAVCO as part of the Plate Boundary Observatory (PBO), as well as a more limited array of borehole strainmeters. The GPS data extend as far back as 1997 for some stations. Beyond sufficient instrumentation, Cascadia plays host to numerous observable slow slip events, including 16 events from 2003 - 2019 with magnitudes ranging from Mw 6.1-6.8 (Bartlow et al., 2011, Hall et al., 2018, Schmidt and Gao 2010, Szeliga et al., 2008). This catalog of events provides a rich data set to observe patterns in slow slip behavior.

In this dissertation, I will show that 1) there is persistent slip up-dip of tremor during large ETS events beneath the Olympic Peninsula, 2) tremor is concentrated on the leading edge of the propagating slip during large ETS events, and 3) it is possible to empirically scale tremor detections to fault slip distributions with a linear scaling relationship and apply this relation to small-to-moderate SSEs.

There are three related research projects presented in this dissertation. Chapter 2 is published in the *Journal of Geophysics, Geochemistry, and Geosystems* entitled "Spatial Comparisons of Tremor and Slow Slip as a Constraint on Fault Strength in the Northern Cascadia Subduction Zone" (Hall et al., 2018). In the paper, I present slip distributions for a catalog of six major ETS events from 2007 to 2016 in northern Cascadia. I find that slow slip extends about 15 km updip of tremor beneath the Olympic Peninsula. Based on these observations, I propose that along-strike variations in lithology of the overlying crust correspond to along-strike variations in slow slip updip of tremor.

Chapter 3 is published in the *Journal of Geophysics, Geochemistry, and Geosystems* under the title "Peak Tremor Rates Lead Peak Slip Rates During Propagation of Two Large Slow Earthquakes in Cascadia" (Hall et al., 2019). In this paper, I compare tremor and time-dependent slip inversions of the large 2010 and 2012 ETS events in northern Cascadia. I find that during the along-strike propagation of the event, peak tremor rates occur up to 25 km ahead of the peak slip rate. Additionally, this work shows that ongoing aseismic slip persists several days after the main tremor front has passed over a given fault patch.

Chapter 4 will also be submitted for publication to the *Journal of Geophysics, Geochemistry, and Geosystems* under the title "Empirical Scaling Relationship for Small Slow Slip Events in Northern Cascadia". In this chapter, I address the question of whether small (Mw < 6.0) SSEs have a similar scaling between tremor and slow slip as large SSEs. For this work, I use the catalog of slip distributions for large SSEs in northern Cascadia from Chapter 2 (Hall et al., 2018) to calculate an empirical scaling relationship between tremor detections and fault slip.

I then cluster the tremor catalog created by Wech (2010) and maintained by the Pacific Northwest Seismic Network (PNSN) into distinct slow slip events. Using this clustered catalog, I scale tremor detections to predicted slip distributions and compare the predicted surface displacements and strains from these slip distributions to observations in order to validate the scaling relationship for small slow slip events that are near the detection limit.

Chapter 2. SPATIAL COMPARISONS OF TREMOR AND SLOW SLIP AS A CONSTRAINT ON FAULT STRENGTH IN THE NORTHERN CASCADIA SUBDUCTION ZONE

The content of this chapter is published in:

Hall, K., Houston, H., & Schmidt, D. (2018). Spatial Comparisons of Tremor and Slow Slip as a Constraint on Fault Strength in the Northern Cascadia Subduction Zone. *Geochemistry, Geophysics, Geosystems*, *19*(8), 2706–2718. https://doi.org/10.1029/2018GC007694

2.1 INTRODUCTION

Faults accommodate relative plate motions at plate boundaries in many different ways, from steady aseismic creep to sudden dynamic rupture of a regular earthquake. These behaviors represent end-member mechanisms of slip. Slip in regular earthquakes propagates near shear wave speeds, radiating strong seismic waves. Under certain conditions, slip is unable to reach dynamic velocities, and propagates more slowly, on the order of km/d (Obara et al., 2004). These events are referred to as slow slip events (SSEs). SSEs have been reported in subduction zones across the world including southwest Japan (Obara et al., 2004), Mexico (Kostoglodov et al., 2010), Costa Rica (Outerbridge et al., 2010), and New Zealand (Wallace & Beavan, 2010). SSEs can release a significant amount of strain, and when large enough, produce measurable surface displacement (Dragert et al., 2004). In Cascadia, detected SSEs range in magnitude from M_w 6.2 to 6.8 (Gomberg, 2010; Bartlow et al., 2011). Important fault properties such as friction on the fault and effective stress may be major factors in controlling the modes of slip on a given fault (Scholz, 1998). Commonly, SSEs occur at the transition zone between stable and unstable frictional properties along the fault and can transfer stress updip into the locked zone (Ozawa et al., 2001).

During SSEs in Cascadia, as well as in many other subduction zones, some fault regions emanate low-amplitude, low-frequency energy (1-5 Hz) in the form of tremor (Rogers & Dragert, 2003) or low-frequency earthquakes (LFEs) (Shelly et al., 2007b). SSEs are commonly accompanied by episodes of increased tectonic tremor, and together are referred to as episodic tremor and slip or “ETS”. In northern Cascadia, ETS events recur every ~11 to 22 months (Brudzinski & Allen, 2007), occur in a confined strip along the plate interface, and have a relatively distinct updip boundary (Wech et al., 2009). It has been observed that tremor migrates along the subduction zone at 7 to 12 km/day in large ETS events (Obara et al., 2004; Wech et al., 2009; Houston et al., 2011). Time dependent inversions of GPS data have shown that slow slip propagates along the subduction zone with tremor (Bartlow et al., 2011). The leading hypothesis suggests that tremor is generated by shear slip on the plate interface (Shelly et al., 2006; Ide et al., 2007) and that tremor can serve as a proxy for slip during ETS events (Aguiar et al., 2009). Recent studies have used this proxy relationship between tremor/LFEs and slow slip to discover increasingly smaller signals of surface deformation on strainmeters (Hawthorne & Rubin, 2013) and in stacked GPS time series (Frank et al., 2015).

Although there is a clear, correlation between tremor and slow slip (Wech et al., 2009; Bartlow et al., 2011; Frank et al., 2015; Hawthorne & Rubin, 2013), tremor has been shown to be an imperfect proxy for slow slip, with several cases of slow slip occurring in apparent absence of tremor. In places such as New Zealand and the Boso Peninsula of Japan, slow slip occurs at very shallow depths (~10 to 20 km) collocated with microseismicity instead of tremor (Wallace & Beavan, 2010). In a few cases in Cascadia, the slip inferred from GPS data has been shown in individual events to extend beyond the footprint of the seismically-detected tremor. Wang et al., (2008) found that a small inter-ETS event in Cascadia (November 2006) produced slip that was shifted updip of tremor. Additionally, during the 2011 ETS event that propagated from Oregon northward into Washington, Wech & Bartlow, (2014) inferred a two-week period during which slip continued to propagate without tremor. The detailed relationship between the two processes is not fully understood. There has not been a systematic study to determine whether there must be a spatial correlation between tremor activity and slip on the fault.

Comparing almost a decade's worth of ETS events, we find persistent patterns in the spatial and temporal relationships between slow slip and tremor. To the extent that tremor is a complete proxy for slip, we would expect that tremor and slip would be collocated and contemporaneous. Less close correlation between tremor and slow slip indicate that conditions that allow for slow slip do not necessarily generate tremor.

Here, we examine the spatio-temporal relationship between tremor and slow slip for six large and well-recorded ETS events in northern Cascadia from 2007 to 2016. We compare two geodetic slip inversions: 1) an unrestricted inversion (URI) where slip is allowed anywhere on a broad regional fault grid; 2) a tremor-restricted inversion (TRI) where slip is only allowed on subfaults where tremor was detected. By comparing the fit of these two slip models we can evaluate whether the restricted tremor footprint can adequately fit the data. This would imply that tremor is a complete spatial proxy for slow slip and that all slow slip during ETS events is tremorgenic. By testing the limits of tremor as a proxy for slow slip, we can begin to probe conditions on the fault that allow for tremor or for slow slip.

2.2 DATA & METHODS

For this analysis, we used cleaned and detrended geodetic data from GPS stations in the Pacific Northwest Geodetic Array (PANGA) and the Plate Boundary Observatory (PBO). We utilize the tremor catalog from the Pacific Northwest Seismic Network (PNSN) (Wech, 2010). Our analysis used ~80 GPS stations ranging from North Vancouver Island to Southern Washington, depending on noise levels and station coverage during a given ETS event (Table 1). Event windows were determined by tremor activity recorded by the PNSN and the number of extra days needed to optimize our offset selection method (see Appendix A). The three major ETS events in northern Cascadia in 2009, 2013, and 2014 were either too small or too noisy to be included in this analysis. Only horizontal components of the GPS data are analyzed due to significant noise in the vertical components.

Our first step was to quantify the net surface displacement at the GPS stations, which appears as an offset in the time series. There are several different techniques to quantify this offset, including using cross-correlation and linear regression (Dragert et al., 2004), and wavelets (Szeliga et al., 2008). For this analysis, we implemented the technique of Principal Component Analysis (PCA) (Jolliffe, 2014) to automatically determine the direction and magnitude of a displacement vector. For our particular implementation of PCA, individual stations are considered separately. Assuming that a given station is only subject to the perturbations due to the slow slip during an ETS event, the data would form two clear clusters (the starting position and the ending position). There exists an ellipse encompassing these two clusters; the major axis of the ellipse would lie along a clear vector connecting these two clusters (Figure 2.1). This vector represents displacement due to the transient signal of slow slip. Spread in the data from this vector could be due to propagation effects, station noise, or large atmospheric signals. We assume that the maximum axis selected by the PCA corresponds to an offset in a time series and reflects the surface displacement due to slow slip at depth from an ETS.

PCA determines the axis of the ellipse by finding the eigenvectors of the covariance matrix of the data matrix. The data matrix X is composed of column vectors of the demeaned time series for the East and North components with M observations:

$$C = \frac{1}{M} X^T X$$

The eigenvector and corresponding largest eigenvalue of the covariance matrix C, represent the direction and magnitude of maximum variance. Projecting the eigenvector scaled by the corresponding eigenvalue into the East and North components, respectively, provides the magnitude of the displacement in each direction, and thus the offset in the time series on a given component (Figure 2.1). See appendix A for further details on the PCA method.

In order to estimate the error in the PCA results, a Monte Carlo analysis was performed where the observations are resampled within their 1σ uncertainties. We ran the PCA method on this new time series and calculated the offset. This process was run 300 times for each station to get the spread of the displacement vector for each station. We then calculated the 95%

confidence ellipse for the 300 offsets picked by the PCA of the resampled data. See appendix A figures A1.3 and A1.4.

The offsets determined by the PCA provide the input for a least squares inversion for slip on the plate interface. We use the McCrory et al., (2012) plate model and discretize the plate interface into 8-by-8 km subfaults. This model incorporates dipping, curving and bending along strike. We chose an 8 by 8 km subfault size to adequately represent the plate model geometry and the irregular shape of the tremor footprint for each ETS. Green's functions for each of the given subfaults are calculated by using an elastic half-space dislocation model (Okada, 1992) that solves for the surface displacement for unit slip on a given subfault, assuming a Poisson's ratio of 0.25 and a rigidity of 40 GPa. The rake on each subfault is constrained to be anti-parallel to plate convergence, using the pole determined by Wells & Simpson, (2001). Second-order Tikhonov regularization was imposed on our slip inversion to minimize fault roughness, misfit, and slip on the edges of the plate interface model.

2.2.1 *Resolution Tests*

To assess the spatial resolution of our data and plate geometry, we performed checkerboard tests (Figure 2.4). For these tests, we calculated the displacements due to a checkerboard pattern of slip on the same station distribution as the 2010 event, then inverted those displacements for slip. We tested a range of sizes of checkerboards to see what scales of features our model resolved by calculating the misfit between the inverted slip distribution and the input checkerboard model (Figure 2.5). This shows that smaller features were below the resolution of the inversion and resulted in a high misfit, largely due to the smoothing effect of the elastic crust overlying the deep plate interface. We found that features smaller than 32 km x 32 km were significantly smoothed in the inversion. We also found that there was less resolution (i.e. greater smearing) of all checkerboards farther downdip due to the greater natural filtering of the earth's crust.

Our half-space Green's functions assume uniform crustal elasticity, although subduction zones likely boast more complex 3-D structures. The resolution tests demonstrate that the linear elastic inversion does not appreciably shift slip towards the updip direction. Furthermore, a study by Williams & Wallace, (2015) inverting GPS displacements in the New Zealand subduction zone found no appreciable spatial shifts due to the assumption of a 1D versus a more realistic 3D structure. They found, however, that for deep, well-instrumented slip, the use of a more realistic heterogeneous elasticity structure led to about 20% less slip than uniform elasticity.

2.3 RESULTS

In the unrestricted inversion (URI), areas of high slip generally collocate with the highest density of tremor (Figure 2.2). For most of the ETS events, the slip is concentrated in two larger patches located beneath southern Vancouver Island/northern Olympic Peninsula and the Puget Sound. Additionally, the contour plots (Figure 2.2) indicate that there is more than 2 cm of slip extending updip of the tremor beneath the Olympic Peninsula (Figure 2.2). If we compare the extent of cumulative slow slip in our results (Figure 2.6), we find that slip extends as shallow as the ~22 km depth contour, which approaches the 20% locking contour from Schmalzle et al., (2014). These results suggest that significant slow slip occurred updip of tremor during the SSEs we studied.

To further probe the robustness of the slow slip updip of tremor, we also performed tremor-restricted inversions (TRI), in which slip was restricted to the subfaults where tremor was detected during each ETS individually. In order to be included in the TRI, a subfault patch needed at least 6 tremor detections. In these inversions, the slip model does not fit the data as well in as the URI. Table 1 shows the residuals from both inversions. It should be noted that the URI and TRI have significantly different numbers of model parameters, which complicates the direct comparison of their residuals. We performed F-tests in order to determine whether the fits for the URI and TRI were significantly different on several ETS events. F-tests confirmed the findings of the residual norm, and that residual norm was a robust statistic for comparing model fit between the two inversions (see section S2).

The TRI results produced upwards of 8 cm of slip concentrated on the updip edge of the slip model (Figure 2.3), implying relatively high strains. The plate convergence rate in northern Cascadia is ~4 cm/yr, and the recurrence interval of major ETS events in northern Cascadia is ~14 months (Dragert et al., 2004). Thus, ~8 cm of slip would exceed the maximum potential amount of accumulated strain between events. Additionally, the slip concentrated along the updip edge suggests that the data prefer a broader footprint than that of tremor.

2.4 DISCUSSION

Our results show that aseismic slip extends updip of tremor during large ETSs in Cascadia. For the six northern Cascadia ETSs studied here, most of the slip updip of tremor is located beneath the Olympic Peninsula and Southern Vancouver Island, with very little observed near southern Puget Sound (Figure 2.2). Figure 2.6 shows a spatial comparison of the cumulative slip compared to the cumulative tremor density. The highest cumulative tremor densities, 4 counts/km^2, are concentrated in the middle of the slip. However, beneath the Olympic Peninsula and into the Strait of Juan de Fuca there is significant slip updip of tremor. This is emphasized by two cross-sections in Figure 2.6. Beneath Puget Sound (B-B’) there is no offset between the cumulative tremor and slow slip. However, beneath the Olympic Peninsula (A-A’), there is ~10 km offset between the updip edge of the slow slip and the updip edge of tremor. This observation of along-strike changes in the cumulative behavior of slow slip and tremor shows a persistent pattern in the along-dip slip behavior.

2.4.1 *Implications of Aseismic Slip Updip of Tremor*

Combining our observations of aseismic slow slip updip of tremor with those of local low frequency earthquakes (LFEs), we explore the relationship between tremor and slow slip, in the context of both along-dip and along-strike variations. It is thought that tremor is comprised of numerous superimposed LFEs (Shelly et al., 2007b), and that LFEs can provide physical constraints on the underlying mechanism generating tremor. Several researchers have used regional seismic arrays, CAFE and the Array of Arrays, to create catalogs of LFEs (Ghosh et al., 2015; Sweet et al., 2014; Chestler & Creager, 2017a). Along the Olympic Peninsula, there are many different “families” of LFEs. An LFE family represents a specific patch on the plate interface that slips repeatedly, creating similar waveforms. LFE families vary in their recurrence intervals along-dip (Sweet et al., 2019) in a manner similar to tremor (Wech & Creager, 2011). The deepest known patch (termed LFE 4) fails every 8 to 15 days and is shown to be sensitive to small changes in stress (on the order of 0.5 kPa) as evidenced by its sensitivity to the tides (Sweet et al., 2014). The shallowest family of Sweet et al., (2019) (LFE 1) is only active during the largest ETS events and becomes sensitive to tides only after 1 to 2 days of slow slip, as is also the case for ETS tremor (Houston, 2015). This decrease in frequency of occurrence of LFEs and tremor towards the updip region, together with our observed aseismic slow slip updip of tremor, suggests two possible explanations of the lack of LFEs and tremor in the presence of slow slip: 1) fault strength increases updip requiring larger stress perturbations (not yet attained in the limited observational period) to generate brittle failure, or 2) the rheology of the region updip of tremor renders it incapable of seismic failure (i.e., LFEs and tremor). We will discuss the first explanation in the context of Coulomb failure strength, and the second in the context of rate and state frictional fault stability that increases updip and has permanently suppressed tremorgenic failure in the region.

In the first scenario, the difference between the strength of the LFE patches and the state of stress is greater farther updip. A greater difference between strength and stress requires much larger perturbations in stress (such as those from a propagating ETS slip pulse) to generate seismic failure on the locked patches. Figure 2.7 shows a conceptual diagram of how stress and strength vary along dip, and how this could lead to less frequent tremor activity on the updip edge. Chestler & Creager, (2017b), present the ductile matrix model as a physical explanation for the generation of LFEs. In this explanation, a patch comprises more strongly locked sub-patches that generate LFEs, which are surrounded by a ductile matrix that slips aseismically. Combining the ductile matrix model with the inference of increasing fault strength updip suggests a physical mechanism for along-dip variations in aseismic slip versus seismic slip. Fault strength is dependent on friction and effective normal stress.

$$\tau_s = \tau_0 + \mu\left(\sigma_n + P_f\right)$$

The fault strength scenario, then, would suggest that properties that control fault strength (friction and effective normal stress) would have the strongest control of tremor and slow slip.

In the second scenario, one or more physical properties that varies along-dip causes patches to transition from stable, aseismic, ductile deformation updip to unstable, seismic, brittle deformation downdip. One way to express fault stability is through fault stiffness. Laboratory experiments on slow slip phenomena show that the generation of slow earthquakes is controlled by the stiffness of the fault (Leeman et al., 2016; Kodaira et al., 2004). Specifically, they found episodic slow slip could occur when the local fault stiffness (*k*) is only slightly less than the critical stiffness (k_c):

$$k_c = (b - a)(\sigma_n - P_f)/D_c$$

In a rate and state friction framework, stiffness is affected by rate and state frictional parameters (b-a) and D_c, or effective normal stress (σ_n - P_f). We would again expect that changes in frictional properties (due to changes in temperature) or changes in effective normal stress (due to changes in permeability) would produce the trend of less stable fault patches and more frequent LFEs downdip and more stable fault patches with only aseismic failure updip.

To assess these two scenarios, we can compare their predicted behaviors with our six ETS events. The fault strength scenario predicts that larger shear stress perturbations caused by larger slow slip events would be more likely to generate seismic failure on the stronger updip patches. Therefore, we might expect to see more updip tremor during larger ETS events. In contrast, in the fault stability scenario, the seismic behavior of the tremor fault patch is independent of the size of the ETS event. Comparing updip tremor in our largest event, 2010, to that in our smallest event, 2011, we find no discernable along-dip difference in the amount of tremor. However, this study includes only a narrow range of event magnitudes. It is possible that the stresses from our largest event, and even the accumulated stresses from all six events, are still below the strength for patches updip of tremor, and thus have not yet generated tremor or LFEs far updip.

Other subduction zones host long-term SSEs with recurrence times on the order of several years, including Japan (Obara, 2011), Mexico (Husker et al., 2012), and New Zealand (Wallace et al., 2012). These long-term SSEs are characterized by large amounts of slow slip lasting months to years. Typically, most of the slip is extends well-updip of tremor. A long-term SSE has yet to be observed in Cascadia, but numerical simulations suggest that recurrence times there could be several decades (Matsuzawa et al., 2013). Long-term SSEs are generally shallower than short-term SSEs, and despite their large slip generally do not trigger tremor shallower than that triggered by the short-tern SSEs. This comparison with other subduction zones appears more consistent with our second scenario in which regions updip of the tremor in short-term ETSs are incapable of generating tremor or LFEs.

2.4.2 *Controls on Fault Strength and Fault Stability*

The scenarios presented above posit that either fault strength or fault stability have a strong control over where LFEs and tremor are present along dip, but these two mechanisms are not independent end-member behaviors. Ikari et al. (2011) showed that there is a systematic relationship between absolute frictional strength and fault stability in a wide range of materials. It is plausible that the strongest control over frictional variations is the along-dip temperature change and that the strongest control over effective normal stress is the trapping of fluids released at the mantle wedge corner (Audet et al., 2009; Kitajima & Saffer, 2012). Both strength and stability are controlled by friction and effective normal stress, therefore systematic changes in these properties can be consistent with either explanation.

We observe persistent slow slip updip of tremor in one region (the Olympic Peninsula) and a lack of such slip updip of tremor elsewhere along-strike. This suggests a property or properties specific to the Olympic Peninsula constant over a time scale of at least years and absent or weaker elsewhere along-strike. This along-strike variability in the updip behavior of slow slip may correspond to large-scale changes in lithology and composition of the overlying crust. It has been demonstrated that tremor is sensitive to the structure (Wells et al., 2017) or lithology of the overlying crust (Brudzinski & Allen, 2007), although it should be noted that the mechanism for how the overlying structure controls tremor is still under debate (Chen et al., 2015; Schmalzle et al., 2014; Tauzin et al., 2017; Wells et al., 2017), there is some consensus that elevated tremor corresponds to high v_p/v_s ratios and increased fluid content. Processes such as temperature-dependent silica deposition or permeability reduction can act as mechanisms for slow slip and are strongly controlled by overriding crustal composition (Audet & Bürgmann, 2014). We hypothesize that lateral variations in material properties of the overlying crust of either thermal conductivity and permeability along-strike could lead to variations in fault strength and thus slow slip behavior along-dip.

In northern Cascadia, there is a transition from the accretionary complex of the Olympics (Brandon et al., 1998) to the Crescent Terrane basalts (Babcock et al., 1992). Our results in Figure 2.6 (c) suggest that the slip updip of tremor coincides with the gravity low from the Olympic Accretionary Complex. In particular, we are interested in variations in northern Cascadia that are spatially similar to our offset between tremor and slow slip. We consider the material properties of the two lithologies and examine the literature to determine the impact of changes in either temperature or permeability separately to assess which is the more dominant control over along-strike changes in slow slip/tremor.

2.4.3 *Influence of Temperature*

Temperature plays a key role in the friction on a fault. In particular, it is thought that the ‘a’ term of rate and state friction (b-a) is primarily controlled by temperature (Scholz, 1998; Rice et al., 2001). When $b-a < 0$ the fault is considered velocity strengthening, which promotes aseismic slip. Variations in tremor have been linked to the along-strike variations in the thermal structure of the incoming plate of the Hikurangi subduction zone (Yabe et al., 2014). In Cascadia, there have been several heat-flow and temperature modeling efforts (Oleskevich et al., 1999; Hyndman & Wang, 1993; Wada et al., 2008; Peacock, 2009) that show an along-strike change in the rate of warming beneath the Olympic Peninsula. This is due primarily to a shallowing of the incoming plate due to a change in dip. However, beneath the Olympic Peninsula there is also a significant change in lithology from the surrounding Crescent terrane basalts to the moderately metamorphosed sediments of the accretionary complex (Orange et al., 1993; Blakely et al., 2005). The contrast in lithologies corresponds to our observations of slow slip updip of tremor.

We created a first-order model of heat flow between three blocks of contrasting thermal conductivities to test if thermal conductivity of the overlying crust could produce sufficient changes in temperature to allow for regional downdip variation in fault behavior (see appendix A). Our modeling results show a change in temperature of 30° C over ~25 km region. This is on the same scale as our observations of updip slow slip and is within a reasonable range to cause changes in frictional behavior. This suggests that it is possible that the contrasting heat conduction could lead to regional differences in slow slip updip of tremor. Though our results suggest that it is possible for temperature to control slow slip behavior, several studies, including (Saffer & Wallace, 2015; Peacock, 2009), note that slow slip occurs at a broad range of temperatures. Saffer & Wallace (2015) also observe very shallow (i.e. at relatively low temperature) slow slip in areas of high pore pressure without any tremor in New Zealand. Examples like this may imply that tremor is more sensitive to pore pressure than temperature.

2.4.4 *Influence of Permeability*

In contrast to heat flow, pore pressure is a much more heterogeneous system with the formation of new hydrofractures dramatically changing the localized pore pressure (Nakajima & Uchida, 2018). A modeling exercise that explores the permeability evolution and resulting pore pressure within the fault zone, similar to our temperature model above, is beyond the scope of this paper. Instead, we present a review of the current literature on the effects of permeability on slow slip and tremor in the context of our observations of slip updip of tremor. A leading conceptual model for the physical mechanism generating slow slip and tremor is the trapping of quartz-rich fluids from the dehydrating subducting oceanic crust. While tremor is found at a variety of temperatures around the world, the common depth corresponds roughly to the basalt-to-eclogite boundary (Audet & Kim, 2016). This transition is the source of the secondary release of water in subduction zones and the likely source for the quartz-rich fluids causing elevated pore pressures (Wada et al., 2008). These fluids are trapped at the plate boundary leading to a building of pressure followed by release of that pressure via slip and hydrofracturing (Audet et al., 2010).

Similar to (Frank et al., 2015), Audet & Bürgmann (2014) posit that slow fault slip leads to transient changes in the permeability through rapid dissolution-precipitation creep processes (Fisher & Brantley, 2014; Giger et al., 2007). Faster healing leads to a faster reduction in permeability and thus faster recharge/overpressurization. The up-dip edge, which is farther from the fluid source, experiences less silica enrichment (Audet & Bürgmann, 2014). This would lead to a smaller reduction in permeability of the overriding crust, and therefore, a relatively larger effective stress compared to the downdip edge. A reduction of fluid cycling and silica enrichment provides a potential mechanism for explaining why tremor may be less abundant on the updip edge relative to the slow slip due to along-dip variations in fault strength.

Additionally, we observe slow slip updip of tremor beneath the Olympic Peninsula but not elsewhere along strike. The direct physical mechanism behind this along-strike change in slip behavior is less clear. Tremor and slow slip have been shown to be sensitive to the bulk composition of the overriding crust (Audet & Bürgmann, 2014; Brudzinski & Allen, 2007).

Audet & Bürgmann (2014) compiled v_p/v_s ratios for both the low velocity zone (LVZ) and overriding forearc crust in multiple subduction zones around the world. They found no correlation between the v_p/v_s ratios of the LVZ and ETS recurrence time, suggesting processes within the oceanic crust do not control the behavior of ETS. Conversely, they found a linear relationship between the v_p/v_s ratio of the overriding forearc crust and the recurrence interval of numerous subduction zones.

By examining results from other subduction zones, we may begin to find a common pattern in the relationship between slow slip behaviors and pore pressure. The Guerrero region of Mexico is another subduction zone with an along-dip offset between slow slip and tremor/LFEs. Guerrero differs from Cascadia because of its flat slab subduction, which may accentuate certain slow slip behaviors. Several studies have shown that in Guerrero the large SSEs are located well up dip of the "sweet spot" where the majority of the seismic energy is concentrated (Kostoglodov et al., 2010; Husker et al., 2012). Similar to the LVZ in Cascadia, the slow slip in Guerrero is concentrated beneath an Ultra Slow-Velocity Layer (USL) (Kostoglodov et al., 2010). A USL is associated with high pore fluid pressures and fluid release from the melting of meta-basalts (Song et al., 2009). It is thought that the transient changes in pore pressure modulate the slow slip behavior (Frank et al., 2015b), suggesting that elevated pore pressures can lead to slow slip in the absence of tremor.

Focusing on the Cascadia subduction zone, Brudzinski & Allen (2007) attribute along-strike variations in ETS recurrence intervals to variations in the composition of the overlying crust. Lowry & Pérez-Gussinyé (2011) use receiver functions to determine v_p/v_s ratios for the Western US and find that there is a strong along-strike variation in v_p/v_s ratios along the Cascadia subduction zone, which strongly matches the gravity anomaly (Figure 2.6). It has been shown that high bulk silica content leads to low v_p/v_s ratios Christensen (1996) due to localization of strain on the relatively weaker quartz rich materials. Audet & Bürgmann (2014) hypothesize that variations in the absolute silica enrichment within the overriding forearc crust along-strike would control the mechanisms of failure, such as dissolution-precipitation creep. The dominant controls on slow slip behavior remains unclear, but there is a demonstrable link between overriding crustal composition and slow slip.

Alternatively, Wells et al. (2017) propose that the structure of the overriding plate via crustal faults may control the permeability of the overlying crust. More crustal faults would increase their permeability of the overriding crust, and therefore mute the tremor in specific areas along the margin. The lack of deep crustal faults beneath the Olympic Peninsula would mean the overriding crust would act as an impermeable cap for fluids along the fault and decrease the effective pore fluid pressure. While this may affect the occurrence of tremor by weakening the fault, the implications for slow slip are unclear.

Our results demonstrate an along-strike variation in the updip extent of slow slip. This along-strike variation corresponds to strong variations in composition and structure of the overriding crust. We suggest that this variation in slow slip behavior could be explained by spatial variations in the properties of the overriding crust. However, our observations are unable to distinguish between composition or structure as the primary mechanism that controls the slow slip behavior. Further laboratory experiments are needed to differentiate between the effect of composition versus the effect of permeability of the surrounding rock on creep behaviors associated with slow slip and tremor.

2.5 CONCLUSION

The slip distributions obtained here delineate relationships between tremor, slow slip, and important fault properties. We found consistent slow slip updip of tremor occurred during six large ETS events between 2007 and 2016 beneath the Olympic Peninsula. Our tremor-restricted inversions showed that the footprint of tremor appears too narrow in the along-dip direction to produce the observed displacements at GPS stations. The localized areas with persistent slip updip of tremor beneath the Olympic Peninsula suggest that some fault properties unrelated to the propagation of the event lead to along-strike variations in strength, allowing slow slip to occur there. Specifically, we note a relationship between the updip slip and the lithology of the overriding crust, with more updip slip occurring beneath the metamorphosed sediments of the Olympic Accretionary Complex. We suggest that the relative change in permeability of the overriding crust from metamorphosed sediments to basalts could alter the strength or mechanical behavior of tremorgenic patches in the region, muting potential tremor while still allowing for aseismic slip.

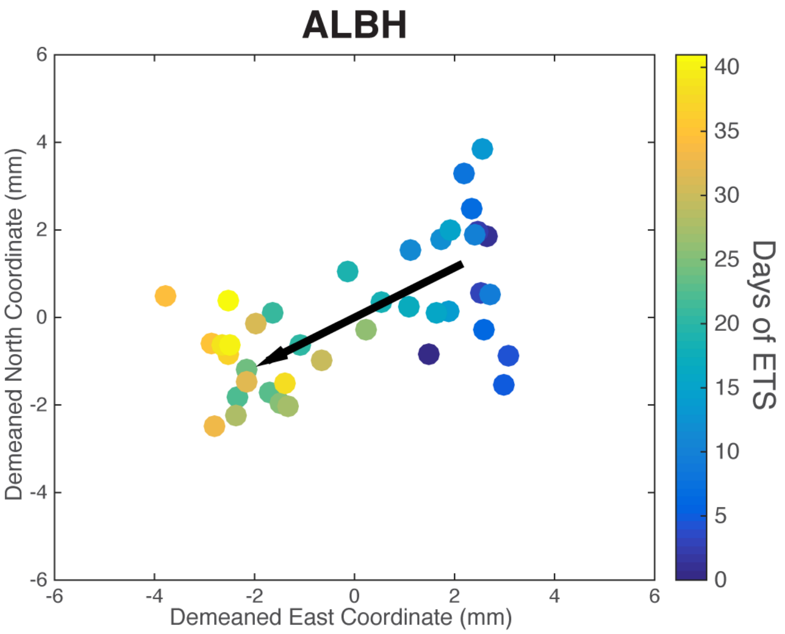

Figure 2.1 Example of the determination of GPS displacements. A map view plot of the demeaned 40-day position time series for station ALBH during the 2010 ETS event with the resulting PCA displacement vector.

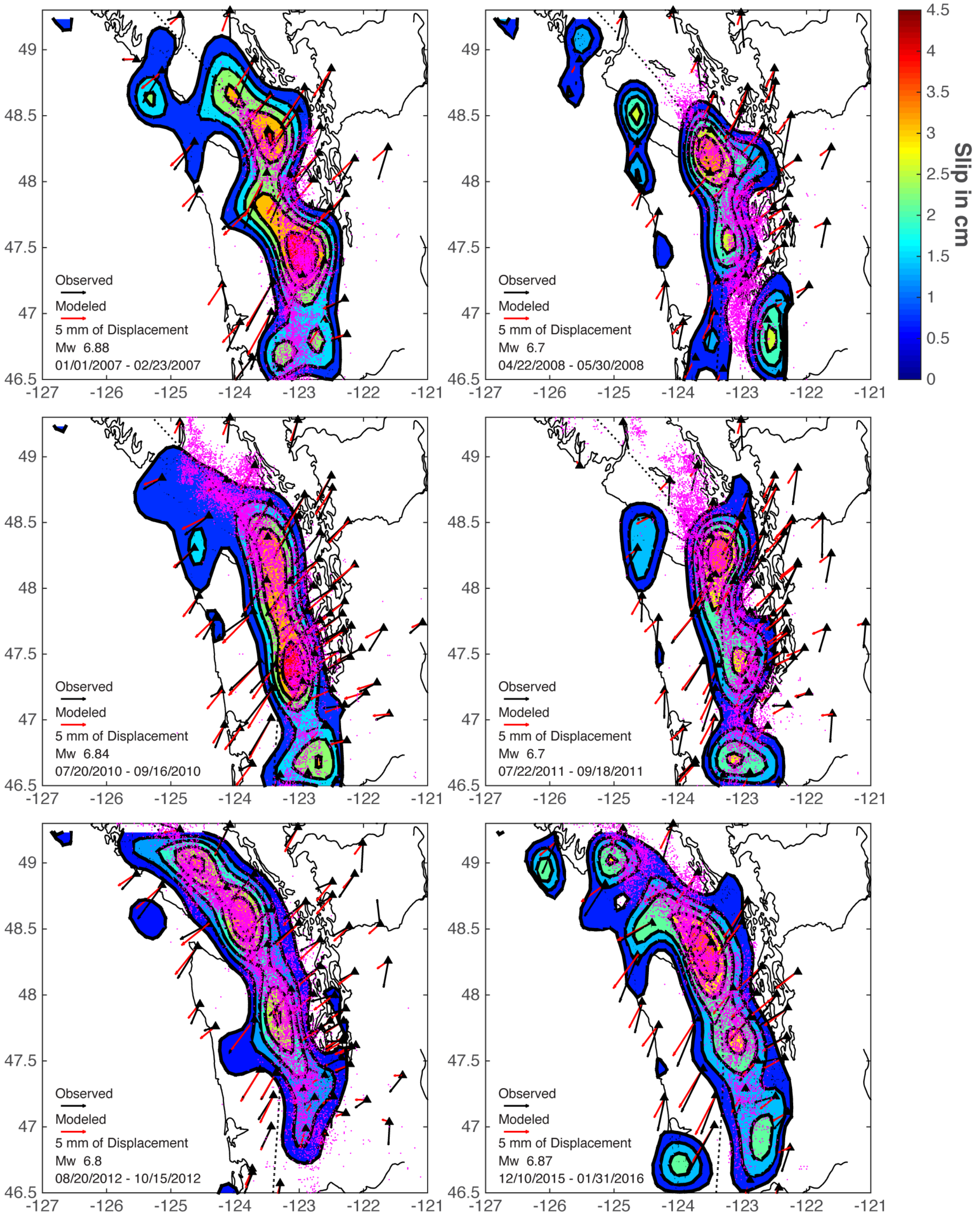

Figure 2.2 Slip distributions from unrestricted inversions (URI) of slow slip from ETSs between 2007 and 2016, with contours every 1 cm. Arrows show modeled (red) and observed (black) surface displacements. Tremor locations from the PNSN catalog (pink dots). Dashed black line represents the 35 km depth contour of the plate interface.

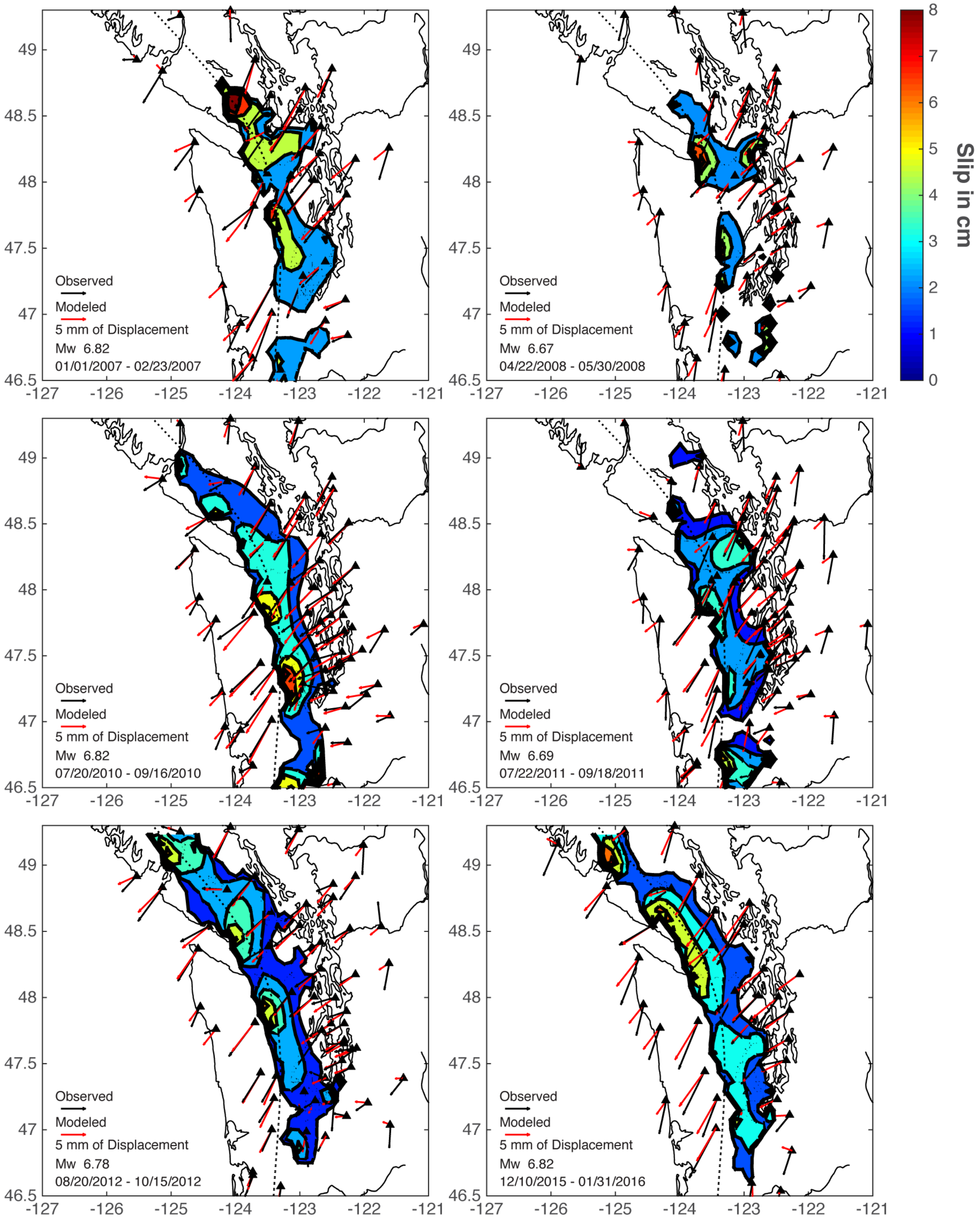

Figure 2.3 Slip distributions from tremor restricted inversions (TRI) of slow slip from ETSs between 2007 and 2016, with contours every 1.5 cm. Slip restricted to subfault patches with at least six tremor events in the given ETS. Arrows show modeled (red) and observed (black) surface displacements. Tremor locations from the PNSN catalog (pink dots). Dashed black line represents the 35 km depth contour of the plate interface.

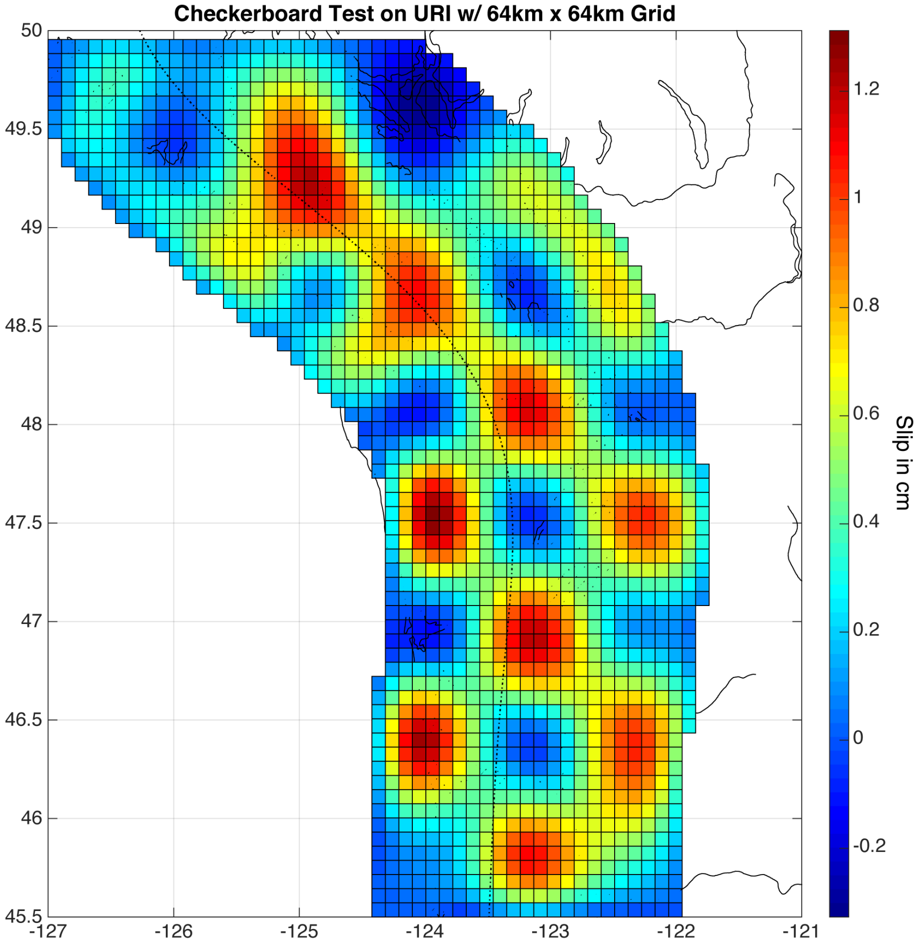

Figure 2.4 Slip distribution resulting from the inversion of the displacements of a synthetic checkerboard slip model, using the station distribution of the 2010 ETS event. The input slip distribution consists of a checkerboard with a 64 km x 64 km (8 subfaults x 8 subfaults) grid with 1 or 0 cm of slip. Dashed black line represents the 35 km depth contour of the plate interface.

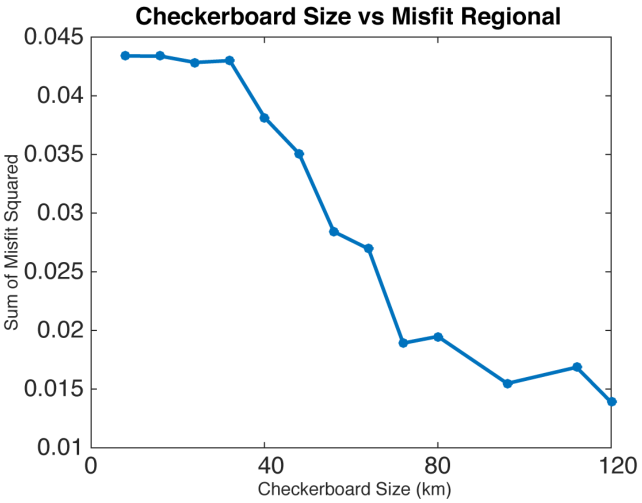

Figure 2.5 Size of checkerboards on synthetic model versus the RMS misfit between the input and inverted slip distributions. Each checkerboard consists of 8 km x 8 km subfault elements assembled to make a grid of square regions of slip and no slip. Smaller features are significantly smoothed in the inversion, resulting in a high misfit.

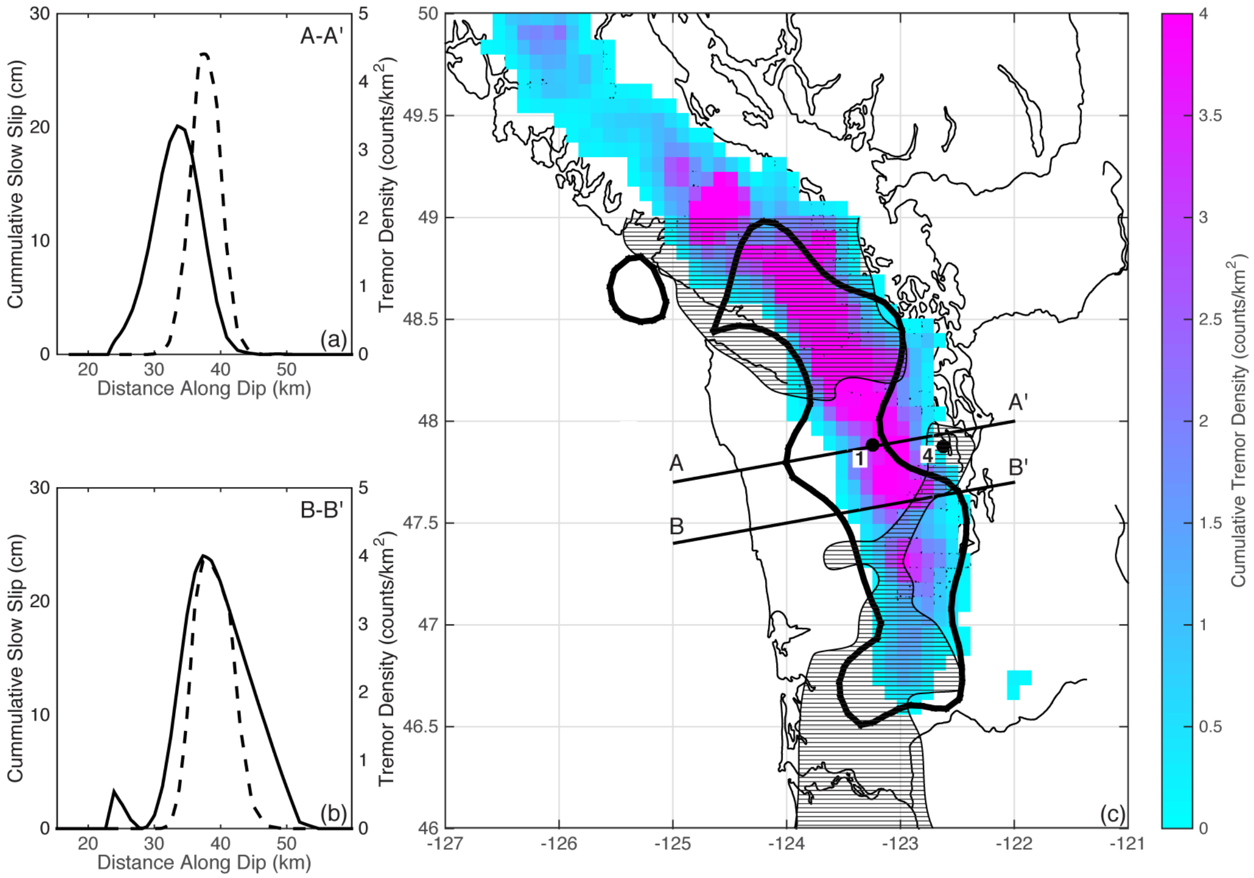

Figure 2.6 Cross-sections of cumulative slip (solid line) and tremor density (dashed line). (a) A-A' cuts through the Olympic Peninsula and indicates that there is about 10 km offset between the updip edge of slip and tremor. (b) B-B' cuts through the Puget Sound and shows little to no offset between slip and the updip edge of tremor. There is an apparent offset on the downdip edge due to scaling of the tremor density. (c) Map of tremor density (aqua to pink) and a contour of 9 cm of cumulative slow slip (solid black line). Gray shaded region denotes the (Blakely et al., 2005) gravity high marking the Crescent terrane, showing the correlation between slow slip updip of tremor and the gravity *low* associated with the Olympic Accretionary Complex.

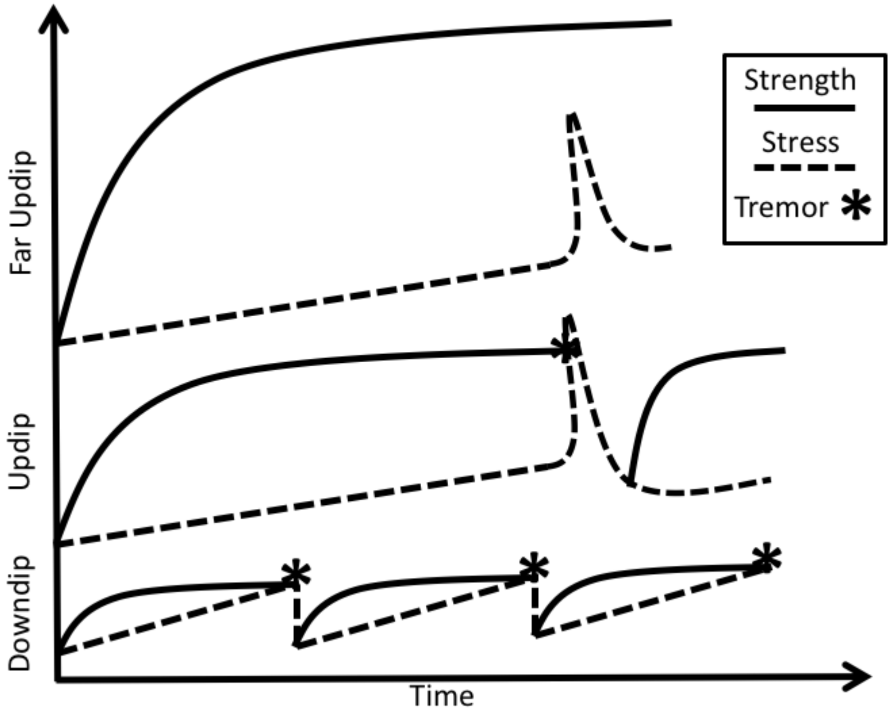

Figure 2.7 An idealized cartoon of proposed along-dip relationship between stress, strength and tremor. Intersection of stress due to tectonic loading (dashed line) and the growing, time-dependent strength of a fault patch (solid line) generates seismic failure in the form of tremor or LFEs (asterisk). The maximum separation between stress and strength increases moving updip.

Table 2.1 *A Summary of Slip Models for Six Cascadia ETS Events*

Year	**Time of Event**	**Mw**	**URI Residual**	**TRI Residual**
2016	12-10-2015 - 01-31-2016	6.87	0.069	0.102
2012	08-25-2012 - 10-15-2012	6.80	0.159	0.163
2011	07-22-2011 - 09-18-2011	6.70	0.192	0.207
2010	07-20-2010 - 09-16-2010	6.84	0.058	0.068
2008	04-22-2008 - 05-30-2008	6.70	0.234	0.278
2007	01-01-2007 - 02-23-2007	6.88	0.086	0.133

Chapter 3. PEAK TREMOR RATES LEAD PEAK SLIP RATES DURING PROPAGATION OF TWO LARGE SLOW EARTHQUAKES IN CASCADIA

The content of this chapter is published in:

Hall, K., Schmidt, D., & Houston, H. (2019). Peak tremor rates lead peak slip rates during propagation of two large slow earthquakes in Cascadia. *Geochemistry, Geophysics, Geosystems*, *20*, 4665-4675. https://doi.org/10.1029/2019GC008510

3.1 INTRODUCTION

Episodic tremor and slip (ETS) events occur in subduction zones around the world including Cascadia (Rogers & Dragert, 2003), southwest Japan (Obara et al., 2004), and Costa Rica (Outerbridge et al., 2010), and manifest as various slow earthquake phenomena, from aseismic slip (Rogers & Dragert, 2003) to tremor or low frequency earthquakes (LFEs) (Shelly et al., 2007). In Cascadia, ETS events occur in the transition zone between the updip locked seismic portion of the plate and the downdip, aseismically slipping portion (Obara, 2011). A single ETS event in Cascadia can last up to weeks and have a substantial moment magnitude, from Mw 6.2 to 6.8 (Hall et al., 2018). Thus, ETS events release significant amounts of stored strain, playing a key role in the state of stress in the transition zone between the seismic and aseismic regions of a subduction zone.

It is commonly thought that tremor only occurs when a fault is already near failure (Rubinstein et al., 2009) and therefore only a small stress perturbation is necessary to cause seismic failure. Bartlow et al., 2011 explored whether tremor was generated ahead of the main slip front in the Mw 6.8 2009 Oregon ETS. They concluded that within the resolution of their model tremor propagated with slow slip rather than ahead of it. We explore this same issue farther north in Cascadia where large slow slip events generate abundant tremor and GPS datasets. Numerical models describing ETS as a slip pulse propagating along-strike (Ando et al., 2010; Nakata et al., 2011) have shown the stresses from a distant slip pulse can be sufficient to generate seismic failures (i.e. LFEs or tremor) on the stronger, more brittle patches. Laboratory experiments have also shown tremor-like-signals ahead of stick-slip failure (Zigone et al., 2011), and similarly, suggest that this is caused by temporary increases of stress induced by the rupture front propagation.

Although tremor is closely related to slow slip, it has been shown that tremor and slow slip are not perfect proxies for each another (Hall et al., 2018); specifically, slow slip has been shown to occur in the absence of tremor (Hall et al., 2018; Wech & Bartlow, 2014). This suggests that although tremor is most likely driven by slow slip, the actual generation of tremor depends on the relative levels of stress and strength of the fault. An outstanding question in the field of slow slip and tremor is, how does the stress from propagating slow slip drive tremor. For example, are peak tremor rates coincident with peak slip rates? And does slip induce tremor in not-yet-slipping regions ahead of the propagating slip pulse? Here we incorporate both geodetic and seismic observations to compare the spatio-temporal evolution of slow slip and tremor to address these questions.

3.2 DATA & METHODS

We explore the temporal and spatial relationships between tremor and slow slip by performing time-dependent geodetic inversions of two major ETS events in northern Cascadia.

For this study, we examined two large events in the northern Cascadia subduction zone: 2010, 6.84 Mw and 2012, 6.80 Mw (Hall et al., 2018). All tremor locations come from the Pacific Northwest Seismic Network (PNSN) (Wech, 2010). The 2010 and 2012 ETS events propagate along-strike in opposite directions, northward and southward respectively, allowing us to test for the influence of propagation direction in our observations. Both events are relatively large for Cascadia, but the 2012 event is complicated by several days of stalled propagation on the southern tip of Vancouver Island. However, it was one of the few southward propagating events of its size with sufficient station density to compare to the 2010 event.

In order to determine the timing and location of slip, we perform a time-dependent inversion of all three components of GPS data, which were processed and cleaned by the Pacific Northwest Geodetic Array (PANGA) and include 72 or more PANGA and Plate Boundary Observatory (PBO) stations (Figure 1). The time series were windowed to include +/- 15 days around the peak tremor activity determined by the PNSN catalog. The stations span from northern Vancouver Island to northern Oregon. Each stations' time series are further cleaned by removing outliers that are greater than 2σ from a moving mean.

Our time-dependent inversion uses the Extended Network Inversion Filter (ENIF) (McGuire & Segall, 2003; Segall & Matthews, 1997). A Kalman filter-based inversion has been used in several tectonic settings to estimate slip transients on the Cascadia margin (McGuire & Segall, 2003; Schmidt & Gao, 2010; Bartlow et al., 2011), Japan (Miyazaki et al., 2003), as well as the San Andreas (Murray & Segall, 2005). Following the methods of Schmidt & Gao (2010), we use a triangular fault model based on the McCrory. et al., (2006) plate model of the Cascadia subduction zone and ignore the fault elements that are offshore, which are poorly constrained by terrestrial GPS. Each of these triangular fault elements is approximately 43 km^2. The Green's functions were calculated using a boundary element code, Poly3D, which allows for triangular dislocations in a homogeneous half-space (Thomas, 1993). Across northern Cascadia, the direction of plate convergence varies due to the plate curvature and the along-strike transition from subduction and rotation to pure subduction (Wells & Simpson, 2001). The rake of the slip on each fault element varies smoothly from the regional plate convergence direction in Southern Cascadia to that of northern Vancouver Island as determined by Wells & Simpson (2001).

The ENIF employs an extended Kalman filter, an iterative least-squares algorithm, that estimates slip and slip rate on a fault element constrained by three-component GPS time series of surface displacement. The ENIF models surface displacement to be a superposition of tectonic motion from fault slip, benchmark motion, and white noise. Hyperparameters, which define the noise models and other constraints on the slip model, are included within the state variable and optimized along with fault slip and slip rate. Those hyperparameters include white noise uncertainty (σ), benchmark motion (τ), temporal smoothing (α), spatial smoothing (ρ), and positivity (γ). Unlike the Network Inversion Filter (Segall & Matthews, 1997), the hyperparameters are included in the state variable in their natural logarithmic parameterization in order to enforce positivity (McGuire & Segall, 2003). The *a priori* white noise hyperparameter of 2 cm (σ) was selected as used in Bartlow et al., 2011. The optimal initial values for all other hyperparameters were selected via a systematic grid search. Figure 1 shows the fit of the ENIF to the 2010 time series for several key stations highlighted on the station map.

3.3 RESULTS

To test the effect of propagation direction on the relationship between slow slip and tremor, we examined two ETS events (2010, 2012) that propagate in opposite directions along the subduction zone. Below, we describe the finer details of each event and movies of each event can be found in the supplementary materials.

3.3.1 *2010 ETS Event*

The 2010 ETS event begins in July and continues through September, and the slip sums to a Mw 6.8 event. At the beginning of the event, the tremor is concentrated down dip beneath the Puget Sound. When the tremor is further down dip, there is no resolvable concentrated patch of slip corresponding to the tremor, but instead a broad low-amplitude signal. This could be due to diminishing fault slip resolution with depth or temporal smoothing of the transient signal. As the tremor activity becomes more vigorous it begins to move up dip and the ENIF begins to resolve slow slip geodetically. Although we are unable to resolve a spatial propagation of fault slip that correlates with this initial updip propagation of tremor, we do see a large increase in the magnitude of the slip (Figure 2). The tremor and slow slip propagate bilaterally along-strike together, but the majority of the tremor propagates northward. We resolve higher amounts of slow slip on the northward propagating limb of the event. During the propagation phase, we observe that the tremor is concentrated on the leading edge of the slipping patch. After the main tremor front has passed the slipping patch, we observe continued slipping on fault patches. Additionally, we observe that the slow slip beneath the Olympic Peninsula continues ~15 km up dip of the tremor cloud several days after the main tremor front (Figure 2). This is consistent with static slip inversions (Hall et al., 2018). Given the daily sampling and temporal smoothing of the GPS data, we are unable to geodetically resolve temporally finer features such as rapid tremor reversals or streaks which are known to occur behind the initial tremor front and may contribute to the ongoing slip on a patch (Houston et al., 2011). As the event ends, minor tremor activity continues with little resolvable slip (Figure 2).

3.3.2 *2012 ETS Event*

The 2012 ETS event begins in the middle of Vancouver Island, and similarly to the 2010 event (Figure 3), fills the width of the tremorgenic zone before bilaterally splitting and propagating along strike. Due to larger station spacing on northern Vancouver Island, we are unable to fully resolve the northward-moving slow slip. We do resolve the southward-moving slow slip. The 2012 event presents some unique challenges as the event stalled for several days on the southern tip of Vancouver Island before continuing southward. During this time, the slow slip and tremor are collocated. As the event begins to continue southward along strike, we again see tremor concentrated on the leading edge of the slipping region. We also observe slow slip up dip of the tremor beneath the Olympic Peninsula (Figure 3) as in the 2010 event, as well as in static inversions (Hall et al., 2018). Similarly to the 2010 event, the slow slip and tremor once again collocate before dying away, as the 2012 event terminates.

3.4 DISCUSSION

We can consider three different phases of the ETS event: initiation, propagation, and termination. During the initiation and termination phases, tremor and slow slip tend to be collocated. However, during the propagation phase, we observe tremor on the leading edge of the slip patch and ahead of the highest slip rates (Figures 2 & 3). It should also be noted that given the stopping and restarting of the 2012 ETS event, the different phases of the ETS event are more difficult to define. For 2012, tremor is most clearly leading the largest slipping patch in the 9/19 and 9/27 frames of Figure 3.

In order to further investigate this observation, we compare the slip front with the tremor density. Figure 4 shows the comparison of tremor density and slip rates along-strike at the 45-km contour in a 6-km wide swath at several time slices. The peak tremor rate leads the peak slip rate throughout the propagation phase of the ETS event, as indicated by the occurrence of the highest tremor densities near the leading edge of the high slip-rate patch. In addition, we also observe a distinct lack of tremor on the trailing edge of the propagating slip patch (Figure 2). We do not believe that either of these observations are due to biases in the tremor catalog itself, see Supplemental Materials.

3.4.1 *Resolution Tests*

Before considering the implications of the relative location of tremor and slow slip, it is essential to evaluate whether smoothing in the ENIF introduces biases into the location of inverted slow slip. Specifically, we wanted to check whether the filter introduces any temporal lag that could potentially explain the observed offset between the tremor front and the peak slip rates. We therefore created a synthetic model to test how much the temporal and spatial smoothing of the inversion affect the location and timing of the slip and to test the lower bounds of resolvable slip. We calculated daily tremor densities based on the 2010 ETS event on a grid of 8 x 8 km subfault patches on the McCrory et al. (2012) plate model. We then scaled the daily density maps into slip distributions such that the overall moment equaled moments from static inversions (Hall et al., 2018). At each time step, we forward modeled the surface displacement using the Okada (1992) Green's functions to generate synthetic time series. In order to better mimic time series, we added white noise and colored noise (random walk: 1 mm/√yr) noise to our synthetic time series, which are the two noise sources modeled by the ENIF. The white noise added to each synthetic time series of the predicted surface displacements used daily 1σ uncertainties as determined for each station and component from the data (typically ~2 mm on both the north and east components).

The resulting synthetic time series was processed through the same preprocessing procedure as the real data and then inverted, starting with the same initial hyperparameters as the 2010 event. Although the ENIF evolves the hyperparameters during the inversion process, our time series results fit the synthetic data to the same level of misfit as our results from the 2010 event. In Figure 5, the pink dots represent the tremor used to generate the synthetic time series and the black contour at 0.15 cm/day of slip rate highlights where the inversion infers that slip occurred. Additionally, in comparing tremor density and peak slip rates along strike (Figure 6), we find that in the synthetic model the tremor and slip rate peaks are aligned, unlike in the slip inverted from the actual GPS data. Spatial and temporal smoothing in the inversion produces some spatial smearing and damping of the input synthetic slip distributions, but minimal temporal lag or up-dip smearing of slip in the resolution test. Thus, this test provides confidence in the inversion's ability to recover the location of propagating slip.

3.4.2 *Timing of Updip Slow Slip*

Our resolution tests show that spatial smoothing impacts the along-strike direction more than the along-dip direction. There is very little smearing along-dip, which means that our along-dip observations of up-dip slow slip are robust. Static slip inversions (Hall et al., 2018) show that there is often significant slow slip updip of tremor in northern Cascadia. Our results for the 2010 ETS event show that updip slow slip is occurring several days after the main tremor front, Figure 2 (8/18 - 8/23). Rapid tremor reversals (RTRs) have been observed several hours to days behind the main tremor front and often extend farther updip than the main tremor front (Houston et al., 2011). Though we are unable to specifically resolve RTRs, the observation that RTRs occur behind the main front is indicative of ongoing strain release behind the main slip front. We suggest that this strain is due to ongoing aseismic slip that extends farther updip.

3.4.3 *Leading Tremor in Comparison to Slip*

Given the results of the resolution tests, we can discuss our observation of tremor concentrated on the leading edge of propagating slip. Figure 4 clearly shows that, as the slip patch propagates along strike, much or most of the tremor occurs around its leading edge. This asymmetric behavior of tremor can be broken into two observations: 1) tremor occurring ahead of peak slip rates, and 2) a lack of tremor at the center and trailing side of the inverted slip patch. In the following sections, we will consider existing numerical models, geologic investigations, and laboratory experiments to explain our observations of the spatiotemporal relationship between tremor and slip.

3.4.3.1 Driving Stresses Trigger Leading Tremor

The first observation we address is the initiation of tremor ahead of the peak slip rate. It has been demonstrated that tremor can be triggered by small stresses (on the order of kPa) such as teleseisms (Rubinstein, 2009) or tidal stresses (Houston, 2015). The relative along-dip seismic activities and recurrence behaviors of different LFE families have been proposed to indicate the relative strength/stability of those patches (Sweet et al., 2019) and suggests that some of the tremorgenic patches (the farther downdip ones) are closer to failure. Our observed results fall somewhere between the end member behaviors shown in Figure 1 of Bartlow et al. (2011). We hypothesize that small amounts of tremor ahead of the slip front are triggered by shear stresses ahead of the propagating slip pulse, after which tremor may continue for a few days driven by initial low rates of slip. By the time peak slip rates occur, tremor activity is often dying away (Figure 4).

That tremor could be induced ahead of actual slip is supported by both laboratory observations and numerical models. Laboratory studies have observed tremor-like-signals ahead of slip events (Zigone et al., 2011). They suggest that these tremor-like-signals are due to an increase of stress induced by the propagation of the rupture front on patches where the stress state is near failure. This is also consistent with numerical modeling efforts, which predict that tremor can be induced by driving stresses ahead of the slip front (Nakata et al., 2011).

To explore how driving stresses ahead of the propagating slip pulse could trigger tremor, we calculated the stress on each fault element using Green's functions generated by a boundary element code Poly3D (Thomas, 1993) and slip rates from our time-dependent inversions. For these results, we only considered shear stresses in the dip-slip direction due to a slip pulse propagating along strike. This is a reasonable approximation given that the slip is almost entirely in the dip direction (depending on the direction of plate convergence). Thus, the majority of the driving stress is in the dip-slip direction. Our resulting peak stresses are on the order of 2 to 3 kPa/day (Figure 4) with total static stress drops of about 20 kPa. During the times of peak tremor density, stresses are on the order of 1 to 2 kPa/day. The stress release rates we calculate are similar in amplitude to the tidal and teleseismic stresses that are sufficient to generate tremor (Houston, 2015; Rubinstein et al., 2009). These latter mechanisms also likely operate by generating aseismic slip that loads tremor patches, and the amount of that aseismic slip depends directly on the level of stress. Therefore, the stresses produced by our inverted slip are also sufficient to generate tremor. In fact, the actual stresses from ETS slip are probably several times larger due to the smearing by the inversion. In addition, the stresses on small tremor patches are likely geometrically concentrated in any case (ETS slip, tidal, or teleseismic stresses), but it would be very hard for us to say by how much, and beyond the scope of our analysis, as the size of tremor patches is poorly known.

We find that peak tremor density occurs near the leading edge of peak stress release rate during the propagation phase of the event and that the majority of seismic failure in the form of tremor typically occurs before the maximum stress release rates (Figure 4). This suggests that small initial stress release from the onset of propagating slip are sufficient to trigger tremor and that once tremor asperities have failed seismically, they become less sensitive to continuing stresses. Given the spatial and temporal smoothing in our inverted slip model, we are unable to resolve spatial features in the slip distribution smaller than 15 km in diameter. The offset between peak slip rate and peak tremor density is at its maximum 25 km and therefore near the observational threshold, as determined by static inversions in Hall et al., (2018). We cannot discern how far ahead of the actively-slipping region tremor is triggered by driving stresses.

3.4.3.2 Reduced Tremor Behind the Slip Front

As discussed above, we find that peak tremor rates lead peak stress rates. Given that tremor can be triggered by relatively small stresses (kPa) (Rubinstein et al., 2009; Houston, 2015), we would expect significant tremor to continue in the presence of significant slip/stresses. However, our results show that during the propagation phase, ongoing aseismic slip persists well after the main tremor front has passed over a given fault patch (Figure 2).

We can consider numerical models of tremor and slow slip to help explain this behavior. Nakata et al., (2011) used a numerical model based on Ando et al., (2010) to test the influence of several different parameters (such as LFE patch density and distance between patches) on rupture model behaviors. In their model, tremorgenic patches experience initial stress ahead of the propagating slip front as well as during times of active slip. In certain model runs, Nakata et al. found that when the patch density was high and the distance between patches was low, initial failure concentrated on the tremorgenic asperities during the main slip front, generating seismic failure. After the initial front passed, they observed ongoing slip, which was broadly distributed and not concentrated on the asperities. They interpreted this broadly-distributed slip as aseismic slip.This is similar to our observation of continued aseismic slip behind the active tremor front. It is important to note that the Nakata et al. work modeled tremorgenic patches within a theoretical large LFE family; however their model is non-dimensional, and we expect that it should scale up to our larger, full-event observations. Nakata et al. suggested that this continuing slip behind the propagation front and the triangular moment rate functions that they obtained, are indicative of crack-like rather than pulse-like slip propagation. For comparison, the moment rate function from our model shows a similar triangular shape (Figure 7). We calculate this moment rate over a 43 km^2 fault patch covering a known LFE family (LFE 3) beneath the northern Olympic Peninsula (Chestler & Creager, 2017). A comparison of the model results of Nakata et al., (2011) with our geodetic slip evolution, is supportive of the idea that slow slip propagates along-strike in a partially crack-like manner, as opposed to a narrow slip pulse as concentrated as tremor. This comparison also suggests that, in northern Cascadia, the tremorgenic patches are dense and close together.

Studies on possible exhumed tremorgenic zones, may also support our interpretations and link them to modeling work. Exhumed subduction zones can provide constraints on the mechanical behavior of a tremorgenic zone (Fagereng & Diener, 2011; Fagereng et al., 2018; Ujiie et al., 2018). Some of the common characteristics are a wide zone of deformation, evidence for both brittle and ductile behavior, and evidence of fluids (i.e. extension veins). Fagereng et al., (2018) suggest that tremor recurrence is controlled by a cycle of fluid-pressure-driven failure and that healing and fluid production rates determine tremor behavior. After the initial vigorous tremor front passes over a fault patch, new cracks are formed, fluid pressure is reduced, effective strength increases, and the tremor/LFE patch is no longer near failure as it takes time for pore pressure to build up and the new cracks to reach a threshold stress state again.

This notion of a change in physical condition of tremor/ LFE patches after the passage of the main tremor front was also addressed in the ductile matrix model of Chestler & Creager (2017), dubbed the “chocolate chip cookie model”; it provides a useful framework to discuss our results. In Chestler & Creager’s model, some stronger or more brittle portions of the fault produce LFEs (the chocolate chips) and are surrounded by a weaker, more ductile matrix (the cookie). At the time of an ETS event, these patches are relatively close to failure. When the slip front begins to pass over the area, small initial stresses cause some of the patches to fail. The patches that do not immediately fail are loaded with more stress and brought even closer to failure (Sweet et al., 2019). The patches that are now closer to failure become increasingly sensitive to the passing stress due to tides, as has been inferred from the tremor record (Houston, 2015; Sweet et al., 2019). Eventually, the majority of the tremorgenic patches or chocolate chips have failed and are no longer close to failure. If the context of Fagereng et al.’s, (2018) proposal, the majority of the later slip, and therefore stress release, occurs with few LFEs or tremors because enough cracks have opened to drop the pore pressure well below the threshold of seismic failure. Linking our results to the numerical models, as well as geological observations, we might infer that the LFEs (chocolate chips) in northern Cascadia must be relatively densely packed in order to produce interactions similar to (Nakata et al., 2011). Additionally, if tremor recurrence is controlled by a cycle of fluid-pressure-driven failure (Fagereng et al., 2018), the length scale between tremorgenic patches would control the loading of nearby patches due to fluid migration from newly opened cracks.

3.4.4 *Outstanding Issues*

One of the challenges in comparing geodetic and seismic data is that the tremor catalog has much finer temporal resolution than GPS daily positions. The PNSN tremor catalog consists of detections in 5-minute time windows (Wech & Creager, 2008), whereas the daily GPS positions that we use average of a station’s position over a 24-hour period. In addition to that daily averaging in the GPS positions, the inversion procedure introduces additional temporal smoothing. Although our resolution tests show that there is minimal temporal lag introduced by the smoothing, there is still spatial smearing of the slip hampering our resolution. Analysis of a Mw 7.6 long-term slow slip event in Guerrero, Mexico suggests that the slow slip is more sporadic and clustered than previously thought (Frank et al., 2018). Perhaps our relatively short-term ETS events exhibit similar sporadic behavior on shorter time scales; however, we are limited by the temporal resolution of GPS data.

An implication of these limitations is that we are only able to suggest potential models that explain the macroscopic behaviors we observe (asymmetric tremor distributed asymetrically with respect to the fast-slipping regions), and are unable to discriminate between some of the “microscopic” behaviors of tremor. These microscopic behaviors include complicated sub-daily behaviors including propagation velocity changes (Ghosh et al., 2012), rapid tremor reversals (RTRs, Houston et al., 2011), and streaks (Ghosh et al., 2010). Two potential end-members of macroscopic slow slip behavior could generate the observed dynamic behaviors of tremor: 1) the slow slip is actually as spatiotemporally concentrated and episodic as the tremor, but those small increases in slow slip velocity associated with the individual bursts tremors are below the detection threshold of GPS data; 2) steady aseismic slow slip drives, but is also held back by, asperities of different strengths which interact in a complex fashion to generate bursts of tremor. Our results support endmember (2); specifically, our tremor-based resolution tests imply that the actual slip is not simply tracking the tremor. Using geodetic measurements with finer temporal resolutions (strainmeters or high-rate GPS) may allow us to distinguish between steady broad aseismic slip loading asperities of different strengths and impulsive slip generating impulsive seismic behavior.

3.5 CONCLUSION

We used the ENIF to solve time-dependent inversions of the transient surface displacements for the 2010 and 2012 ETS events. Our results are broadly consistent with the conventional notion that to first order, slow slip and tremor propagate together along-strike. However, our time-dependent inversions show that during the propagation phase of the ETS event, peak tremor density occurs on the leading edge of the slipping region and ahead of peak slip rates in both the 2010 and 2012 ETS events. Additionally, we find some slow slip occurring updip of tremor beneath the Olympic Peninsula, as shown in static geodetic inversions (Hall et al., 2018). This up-dip slow slip occurs several days behind the main tremor front, which is when large rapid tremor reversals tend to occur (Houston et al., 2011). We observe consistent behaviors for both the 2010 and 2012 events even though they propagate in opposite directions along strike, and hence infer that propagation direction does not influence our observed behaviors.

The key observation from our results is that tremor is concentrated on the leading edge of the propagating slipping region well ahead of peak slip rates. We found that the stress due to active slipping was the dominant signal in the stress rates, but we did observe small amounts of induced stress increase ahead of the peak stress release. Stress maps based on our inversion results show shear stress release rates on the order of kPa/day and stress drops on the order of 20 kPa. The spatial and temporal smoothing of slip makes features in the slip distribution that are smaller than 15 km in diameter difficult to resolve. Our results are permissive of a conceptual model in which some tremor can be triggered by induced stresses ahead of slip, but our resolution is insufficient to determine whether any initial tremor lies completely outside of an actively-slipping region, primarily because a sufficiently-precise slip front is not resolvable. Additionally, we observe significant aseismic slow slip continues well after the peak tremor activity, sometimes in the absence of any detected tremor. Comparison of our results with numerical modeling (Nakata et al, 2011) suggests that slow slip propagates along strike in a partially crack-like manner, rather than in a slip pulse as narrow as the occurrence of tremor.

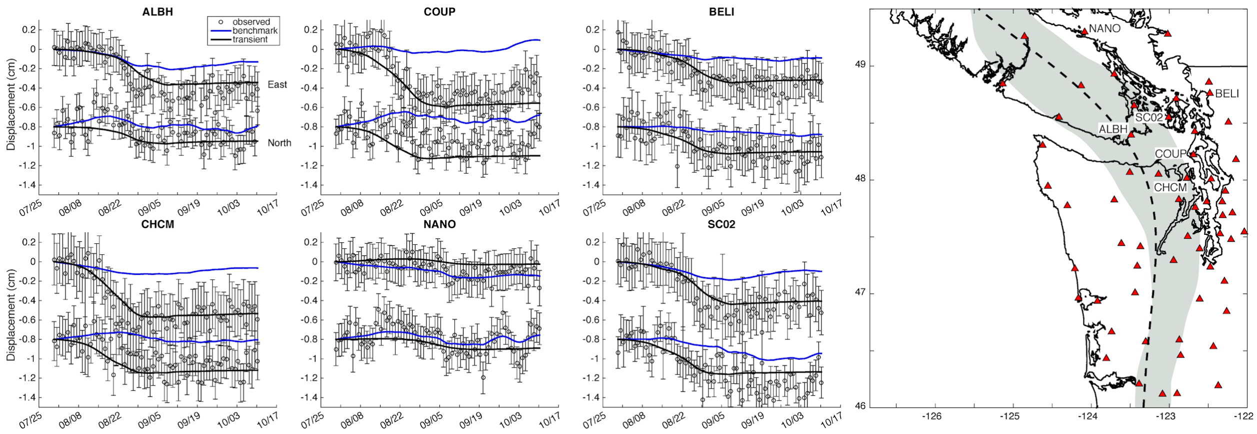

Figure 3.1: Observed (circles) and model predicted (black solid line) surface displacement time series at GPS stations (red triangles on map) for the 2010 slow slip event. Additional time series are shown in the supplementary materials. Black circles represent observed east and north data with error bars, with the north component offset by 1 cm for clarity. The blue line represents the benchmark motion from the model. The gray north-south band on the map denotes the approximate distribution of tremor. Dashed black line represents the 35 km depth contour.

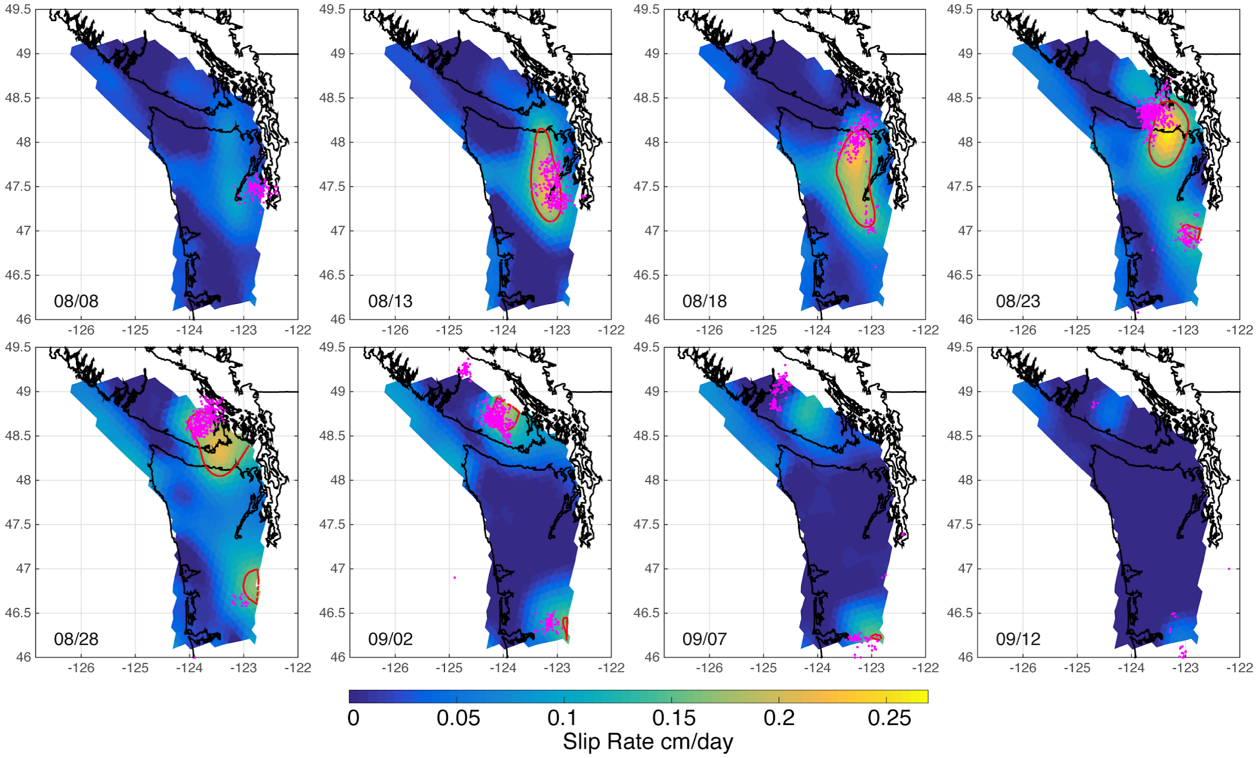

Figure 3.2: Resulting slip rate distributions generated by using the ENIF on GPS data from PANGA for the 2010 ETS event. The event propagates northward toward Vancouver Island. Each time slice represents the slip rate (cm/day) with a red contour at 0.15 cm/day. Pink dots represent the corresponding total daily tremor locations from the PNSN catalog. See the supplementary materials for a movie of the slip and tremor evolution.

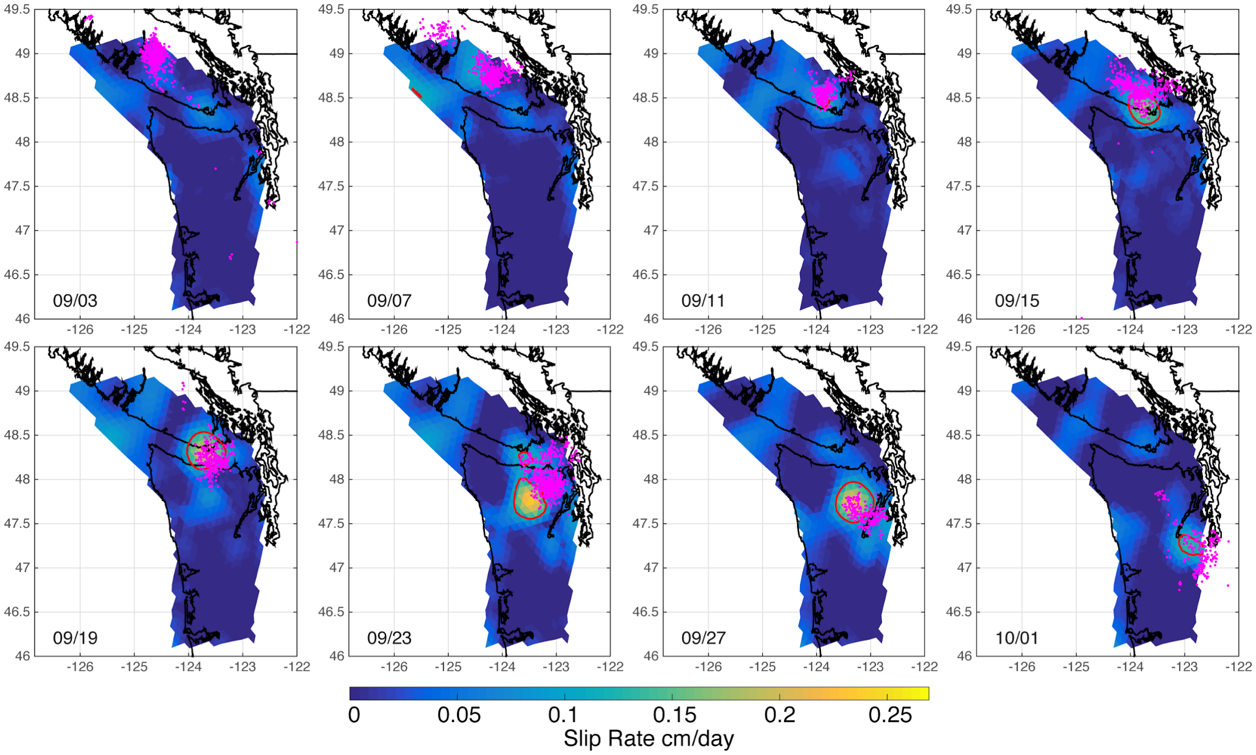

Figure 3.3: Slip rate distributions generated by using the ENIF on GPS data from PANGA for the 2012 ETS event. The event generally propagates southward toward the Puget Sound, but stalled for several days on the southern tip of Vancouver Island (9/11 - 9/15) before continuing southward. See the supplementary materials for a movie of the slip and tremor evolution.

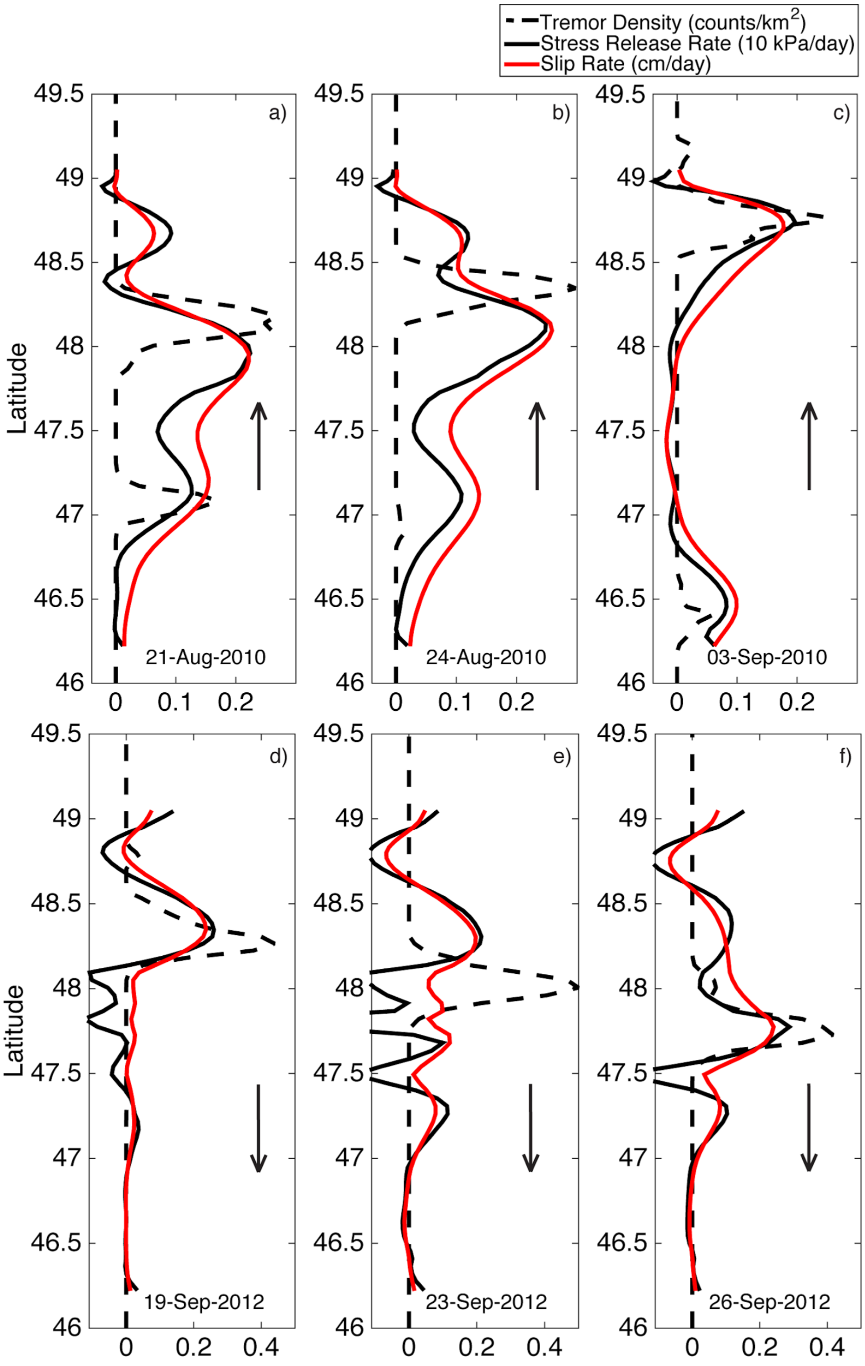

Figure 3.4: An along-strike plot of slip rate (red), stress release rate (solid black) and tremor density (dashed black) for the 2010 (a,b,c) and 2012 (d,e,f) ETS events. The along-strike profile follows the 35 km-depth profile on the plate interface as pictured in Figure 1. Arrows indicate propagation direction. Each panel represents a different stage of the event: a,d) the initial bilateral splitting of the tremor and slip during the events' initiation, b,e) the propagation of both slow slip and tremor beneath the Olympic Peninsula, and c,f) the termination of the event.

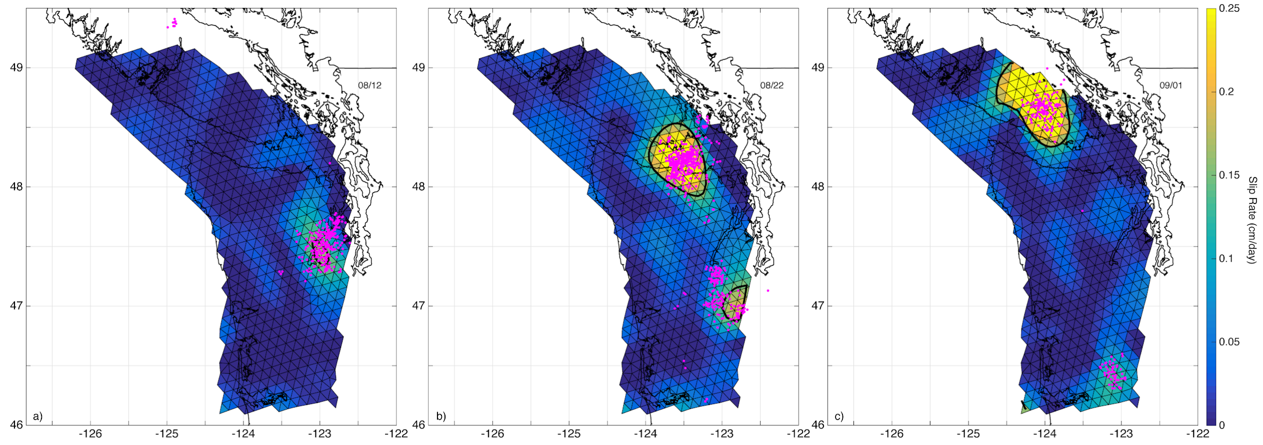

Figure 3.5: (a,b,c) Synthetic resolution test for an input slip distribution that emulates the 2010 event based on the tremor location and timing (pink dots). Black contour, 0.15 cm/day slip rate from ENIF inversion of synthetic surface displacement time series. Slip is somewhat damped and smeared by spatial smoothing, but temporal smoothing introduces minimal lag between the input slip (based on tremor) and the inverted slip (color scale).

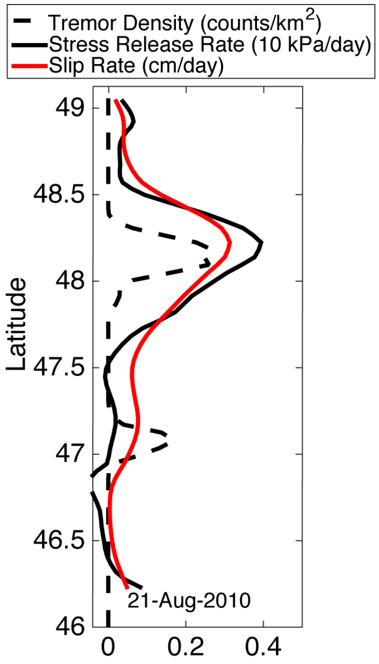

Figure 3.6: An assessment of temporal and spatial smoothing is performed using a SSE simulation where the input time-dependent synthetic slip model is constructed based on scaling the 2010 tremor density (black dotted line). An inversion of the predicted surface displacements results in the inferred slip rate (red line) and stress release rate (black line). The input slip model is spatially smoothed by the inversion (comparing the black dotted and red lines), but the peaks remain correlated, with minimal offset.

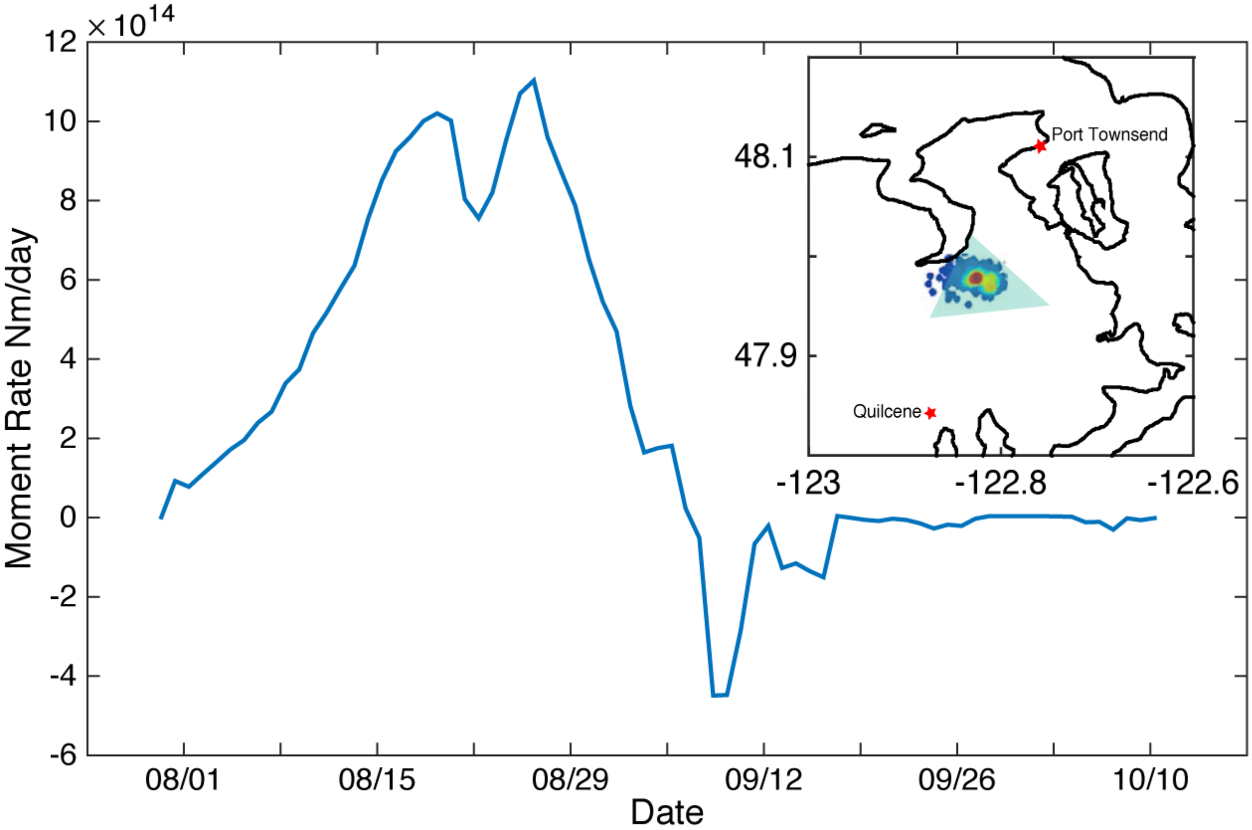

Figure 3.7: A moment rate function for the 2010 ETS event for a single fault patch in comparison with LFE detections in the same location. The inset shows the location of the fault patch (green triangle). This location corresponds to a known detections from the LFE 3 family, which is plotted in the inset map (Sweet et al., 2019). We consider a fault patch with LFE locations in order to compare our observations with numerical models created by (Nakata et al., 2011).

Chapter 4. EMPIRICAL SCALING RELATIONSHIPS FOR SMALL SLOW SLIP EVENTS IN CASCADIA

The content of this chapter is being prepared for submission to the journal of *Geochemistry, Geophysics, Geosystems.*

4.1 INTRODUCTION

The term "slow earthquakes" refers to a range of observable phenomena that have been seen around the world. Unlike regular earthquakes, which have Mo ~ T^3, "slow earthquakes" have Mo ~ T (Ide et al., 2007; Ide et al., 2008; Ide, 2014), where Mo is the seismic moment and T is the event duration. At durations of seconds-to-minutes, slow earthquakes are manifested as vLFEs, LFEs, and tremor (Shelly et al., 2006; Sweet et al., 2014). At durations of days-to-years, slow earthquakes are observed geodetically as slow slip events (SSEs) (Hall et al., 2018; Outerbridge et al., 2010).

Together, vLFE, LFEs, tremor, and SSEs are hypothesized to describe a continuum of slip modes (Peng & Gomberg, 2010). It is generally thought that tremor and slow slip are manifestations of the same large scale process of shear slip on the plate interface (Shelly et al., 2006) and that the presence of tremor implies some amount of slip on faults (Aguiar et al., 2009). Therefore, when we observe tremor, especially vigorous bursts of tremor, we would expect to observe some form of deformation. Previous work has shown empirical scaling relationships between the duration of tremor and the moment for large SSEs. Aguiar et al. (2009) found a linear relationship between hours of tremor and the moment of an event. Such a relationship is important because it has been difficult to robustly estimate the moment of tremor only from seismic observations, whereas geodetic observations have constrained the seismic moment for the largest SSEs. The lack of geodetic observations of smaller ($Mw < 6.0$) SSEs means that our known scaling relationships are limited to large SSEs.

In this paper, we use existing slip models for large SSEs in the Cascadia subduction zone to develop an empirical scaling relationship between fault slip and tremor detections. We then use the extensive tremor catalog for the Cascadia subduction zone to guide our search for smaller SSEs ($Mw<6.0$) that could potentially produce geodetically-observable deformation. Using both stacked GPS time series and local strainmeter data, we then test our empirical scaling relationship, which was determined for large SSEs, to observations of small SSEs. We show that a simple linear scaling between tremor counts and slip is able to accurately predict observed strainmeter records for several events. Our clustered tremor catalog suggests that there are slow earthquakes through most of the observational gap and that the large events (Mw 5.6+) obey a $Mo \sim T$ scaling.

4.2 EMPIRICAL SCALING RELATIONSHIPS

Several studies have developed empirical scalings between seismic and geodetic observations. For example, Aguiar et al. (2009) found a linear relationship between hours of tremor and the moment of an event. One of the long-standing debates is the relationship between moment and duration and how slow slips compare to regular earthquakes. Hawthorne & Bartlow (2018) explored whether large slow slip events are composed of a series of sub-events that follow a $Mo \sim T$ scaling. However, observational limitations prevented a full test of the subevent model. Nevertheless, they show that the moment rate power spectrum is consistent with a continuum of small to medium-sized subevents. Frank & Brodsky (2019) found a scaling relationship between LFEs and moment rate in Guerrerro, Mexico closer to that of ordinary earthquakes, Mo ~ T^3. Michel et al., (2019) generated a catalog of large SSEs for Cascadia and also found events scale similar to regular earthquakes. This is at odds with the moment-duration being governed by scale-limiting as suggested by Gomberg et al. (2017) for Cascadia. By looking at smaller events, we can begin to clarify what scaling relationship is most appropriate for slow slip in Cascadia.

In order to calculate our empirical scaling relationships, we use previously-obtained static slip models for large SSEs in northern Cascadia constrained by GPS (Hall et al., 2018). We compare either the total moments or the detailed slip distributions to the tremor locations from four major SSEs (August 2010, August 2011, September 2012, December 2015). For this work, we used the Cascadia tremor catalog (2009-2019) from the Pacific Northwest Seismic Network (PNSN), which uses the Envelope Cross-Correlation method from (Wech & Creager, 2008). This catalog includes over 360,000 tremor locations where each location represents a detection within a 5-minute window. We choose not to include events before August 2009 because the Wech catalog is not considered complete before this time.

For this analysis, we consider two possible scaling cases. The simplest assumption would be that the cumulative geodetic moment from the event is equally distributed to each tremor detection; we refer to this as the full-moment case. This case assigns all moment to tremor, including moment due to aseismic updip slip, which has been observed in northern Cascadia (Hall et al., 2018). Thus, the full-moment case is likely an upper bound of the relationship. For our second scaling case, we directly compare the geodetically-inferred fault slip distribution to the distribution of tremor detections for a discretized fault model where each grid cell has an approximate area of 64 km^2 (based on the McCrory et al. (2012) plate model); we refer to this as the slip case and find the best-fit line that represents the moment-per-tremor (Figure 1). In this second case, we consider only the slip on fault patches where tremor occurred. As previously mentioned, some aseismic slip occurs updip of tremor, and, furthermore, slip distributions have been spatially smoothed in order to stabilize the inversions, and occupy a footprint significantly larger than tremor. We also force the line to pass through the origin because a non-zero intercept would imply a fairly high level of slip with no accompanying tremor, which seems unphysical. Additionally, the spatial smoothing of the static slip inversions introduces a bias into the slip case such that patches with high levels of tremor can be observed in regions with damped levels of slip. This slip has been smoothed out and distributed to patches with less observed tremor. Therefore, the line fit is likely an underprediction of the actual relationship. The slip case likely produces a lower bound of the moment-per-tremor relationship. Both of these assumptions are reasonable first-order approximations. However, we note that either assumption may break down when examined at higher spatial resolution.

The red lines in Figure 1 show the scaling relationships for each hypothesis. However, Ulberg (2018) noted that the amplitude of tremor during small SSEs is about 50% of the amplitude during large SSEs. This suggests that they release ~50% of the energy. Because we are using scalings based on large SSEs we have to factor this 50% into our final scaling factors: full-moment case = $8.91 \pm 2.6*10^8$; slip case = $3.14 \pm 0.92 *10^8$ Nm per 5-minute tremor detection. As noted previously, the slip case likely has a bias towards underpredicting the relationship between moment and tremor. Therefore, we adopt the full-moment case as our preferred empirical scaling relationship for the subsequent analysis. For the full table of the scaling relationships based on each SSE individually, refer to the supplementary materials.

We can also compare our scaling relationships to the previous findings of Aguiar et al. (2009). They reported a moment release rate of $5.2 * 10^{16}$ Nm per hour of recorded tremor. We can convert that into our measurement of slip per counts of tremor by making some assumptions. The scaling factor from Aguiar et al. (2009) describes the overall moment of the entire event and our scaling factors represent a single fault patch. Based on our slip distributions that we used above, a single fault patch represents 0.23% of the area in a given event. We can then assume a shear modulus of 30 GPa and a fault patch size of 64 km^2 and convert moment release rate to fault slip rate of $6.23*10^{-5}$ m of slip per hour. Again, we have to consider that the Aguiar et al. (2009) refers to the total moment of a large SSE. We can estimate an average tremor rate for a large SSE of ~25 tremors per hour, based on our events used above. Lastly, as noted above that the energy release from large SSEs is twice that of small SSEs (Ulberg, 2018). This gives a final converted scaling rate of $14*10^8$ Nm per tremor detection for small SSEs, which is on the same order of magnitude as our full moment case. This gives us confidence that we are producing a reasonable scaling factor.

4.3 CLUSTERING THE TREMOR

Our goal was to determine if small SSEs behave similarly to large SSEs. We have empirical scalings derived from large SSEs, but we want to know if these are appropriate for smaller SSEs. It is clear upon visual inspection, Figure 2, that the tremor catalog can be divided into bursts of activity that are considered individual events. To do this, we need to cluster our tremor catalog, which we can then scale into slip distributions that predict deformations that can be compared to geodetic records.

Tremor has generally been interpreted as brittle failure on small asperities that are triggered by aseismic slip on surrounding sections of the fault (Chestler & Creager, 2017a). This conceptual model predicts that bursts of tremor activity should be spatially and temporally correlated when neighboring tremorgenic fault patches triggered by the same propagating slip event. Thus, our clustering process assumes that individual tremor detections can be associated with each other based on spatial and temporal thresholds.

To quantitatively cluster the tremor into separate events, we used a density clustering algorithm, DBSCAN (Ester et al., 1996) from the scikit-learn Python library (Pedregosa et al., 2011). DBSCAN has been used in the lightning detection community, for example, to cluster detections (e.g. Nikolay et al., 2016). Density clustering algorithms are based on the idea that objects which form a dense region in the parameter space should be grouped together. There are several advantages of using DBSCAN: (1) it requires very little prior domain knowledge (especially prior knowledge of the number of clusters, (2) unlike a k-nearest-neighbors algorithm), its ability to create clusters of arbitrary shapes, and (3) its efficiency on large databases.

To determine density, DBSCAN uses two parameters: the maximum Euclidean distance between two points to be considered in the same neighborhood (epsilon) and the minimum number of points (MNP) in a cluster. DBSCAN partitions the data into either a cluster or noise (ie unallocated detections) by searching for regions of high density in a feature space that are separated by regions of lower density. The algorithm is looking to find at least the minimum number of points that can be connected to one another by no more than the Euclidean distance defined by epsilon between any two detections.

Our objective with the clustering algorithm is to construct a catalog of SSEs over a range of magnitudes, especially small SSEs, and to use this catalog to identify small SSEs (Mw < 6.0) that could potentially produce enough surface deformation to be observed geodetically. We first project our tremor detections using Pyproj from latitude and longitude (EPSG 4326) to a local Cartesian reference frame (EPSG 32148), which has an origin at approximately -127.39, 46.81, so that distances are in units of meters. Because tremor detections are clustered into distinct events in both space and time, the feature space for the clustering of tremor is the horizontal position (meters) and time (seconds) of an individual tremor detection. DBSCAN is agnostic to the units of the feature space and thus treats time as if it were a third spatial axis when calculating distance. In order to overcome potential differences in the scaling of units influencing the cluster, we convert the time domain component into a spatial domain by multiplying the time by the propagation speed of a typical slow slip event (10 km/day), which we converted into meters/second. Using parameters of (epsilon = 38,000 meters, MNP = 10), DBSCAN divides the tremor catalog into 1109 clusters, with 1% of the tremor detections not allocated to a cluster. It is important to note that our algorithm is less successful at parsing events in southern Cascadia. The tremor catalog of Wech & Creager (2008) likely contains some less reliable detections in southern California before 2015 due to possible instrument issues and false detections in prior years.

4.4 TREMOR-DERIVED SLOW SLIP CATALOG

After clustering, the 1109 tremor clusters are interpreted as SSEs whose magnitude can be estimated with our slip-per-tremor scaling relationship. We use the full-moment case as described above (section 2) as our empirical scaling factor. For each clustered event found in the catalog, we scaled the number of tremor detections into slip distributions for each clustered event based on our previously-determined scaling factors and calculated an inferred moment. It is important to note that this scaling is inherently tied to the tremor detection method (envelope cross-correlation) and the region of detection (Cascadia).

The catalog contains a substantial number of events whose predicted moments are below the current geodetic observation level. This supports the hypothesis that there is a continuum of magnitude-durations (Hawthorne & Bartlow, 2018). It is notable that our catalog does not entirely fill the observational gap between seismically-observable and geodetically-observable events. This is likely due to the clustering algorithm, which sets a minimum number of points necessary for a cluster and therefore a minimum moment based on our scaling relationship. See the supplementary materials for information on the completeness of the catalog, as well as the b-value.

We can compare our scaled moments and durations to known attributes of slow earthquakes (Figure 3). It remains an outstanding question whether slow earthquakes scale like regular earthquakes which have Mo ~ T^3 (Michel et al., 2019) or whether slow earthquakes have moment proportional to duration (Ide et al., 2007). Figure 3 shows that our clustered-tremor catalog produced large (Mw 5.6) events that follow a moment-duration relationship similar to large SSEs and a clear linear upper bound of moments. Our largest duration events follow a path somewhat similar to that in Michel et al., (2019), who determined a relationship of Mo ~ T^3. However, our shorter duration events form more of a cloud. Additionally, we observe a strong Mo ~ T upper bound for moments over that range of the catalog. This is similar to findings in Gomberg et al. (2017), where they suggest a transition from unbounded growth to bounded growth (Mo ~ T) with increasing size. Smaller events need not fill the width of the deep slow slip region, and therefore their growth can occur both along strike and along-dip. Larger events, however, potentially fill the width and thus their growth is bounded in one direction. It is important to note that this unbounded interpretation is predicated on the assumption of constant rupture velocity.

4.5 RESOLVABILITY OF MW 5 SSES IN THE GEODETIC RECORD

In order to validate our empirical scaling relationship for small SSEs, we seek to compare it to the geodetic observations. Our tremor catalog suggests that there are a significant number of events that should range in magnitude from Mw 4.5 - 6.0. In practice, observing the surface deformation to confirm these scaling relationships at the lower range of magnitudes is complicated by the noise levels of geodetic instrumentation. As noted in Peng & Gomberg (2010), there is a range of moments (10^{15} - 10^{18} Nm) over which no tectonic slow earthquakes have been observed. Peng and Gomberg (2010) hypothesized that this gap in detected events is created by the observational limits of geodetic and seismic data.

Given the prevalence of GPS networks in most major subduction zones, GPS is the most common means to measure the crustal deformation from SSEs. Across the globe, the smallest SSEs constrained by GPS are all larger than Mw 6.0. For example, Cascadia - Mw 6.2 (Wang et al., 2008); Mexico - Mw 6.4 (Frank et al., 2015); Japan - Mw 6.3 (Ozawa et al., 2013). Other geodetic methods such as borehole tiltmeters have been shown to be sensitive to much smaller events. Sekine et al. (2010) found events using borehole tiltmeter data in Japan down to Mw 5.4. In Cascadia, we are limited to GPS and a limited number of borehole strainmeters. However, our tremor-based catalog suggests that there are potential smaller events that have yet to be observed. We explore whether it is possible to observe these small events by stacking events and employing data analysis methods to increase the signal-to-noise.

A requirement for the successful stacking of GPS time series (i.e. Frank et al, 2015) is that individual events rupture approximately the same fault area such that the surface deformation pattern remains consistent and coherent. Our clustered catalog allows us to identify SSEs that may meet this spatial criterion. Within our catalog, large SSEs (>Mw 6.0) stand out as long-duration, spatially-extensive clusters of activity, extending along strike (gray dots in Figure 2). Because we are searching for small SSEs (Mw < 6.0), we remove events with durations longer than 15 days from our catalog. In northern Cascadia, these excluded events correspond to the known large SSEs. After removing these 47 large SSEs, we were left with 1062 events in the clustered catalog.

With this catalog of potential SSEs characterized by magnitude and location, we can systematically search for repeating events with Mw <6.0 and stack the geodetic time series of these events. We expect that events of similar moment magnitudes occurring in the same region will generate similar surface displacement observed by GPS, and when these signals are stacked they should add constructively, while the noise cancels out. Our goal is to group our events such that all the events in a group produce similar surface deformation. To do this, we calculated the centroid of each event by averaging the locations of all the tremors within an event in x-y space. We assume that if two events have similarly-located centroids, they will produce similar surface deformation patterns. Tremor is generally constrained to a relatively narrow along-dip band of the subduction zone, (Wech & Creager, 2011). Therefore, we can bin our events' centroids by their y (along-strike) position and can expect reasonably well-constrained locations of all the centroids within a given patch. We divide the catalog into 20 distinct bins, which are numbered and shown in Figure 2. In order to determine the stackability of a given patch, we calculate the standard deviation of the latitudes/longitudes of all the tremor detections within this patch. The larger the standard deviation the more dispersed a patch is and the less likely the signal would stack coherently. We only consider patches with standard deviations in the tremor locations of less than 0.3 degrees. This ensures that the expected moment will be spatially concentrated. Additionally, we count the total number of tremor detections associated with a given patch and only consider patches that have more than 2000 tremors to increase the likelihood of detectable surface displacement. This narrowed our number of “stackable” patches to just five patches (5, 7, 15, 16, 19). We have included our clustered catalog in the supplementary material. We chose to focus our study on the most vigorous patch located in northern Cascadia (Patch 5), where our scaling relationship has been calibrated. Additionally, this patch has minimal competing tectonic signals such as small crustal earthquakes (unlike southern Cascadia), which could potentially mask the small signals we are looking for.

4.5.1 *GPS Data Analysis*

In this section, we perform an analysis of the surface displacement data in order to constrain the average moment associated with a series of small SSEs. Patch 5, which is located beneath the Olympic Peninsula, hosted 16 small events within the period from 2010-2019 with durations of 3+ days. To increase the likelihood of producing a coherent stack, we further filter these 16 events down to 9 events with a similar number of tremor detections.

In order to maximize the signal-to-noise ratio of the GPS time series, we attempt to remove possible sources of noise. First, we extracted a time period that extended 1 month before and after each clustered event. Then, we removed the long term (>1 month) trends by removing any linear trends on each component of each station. We removed individual days where the error for the daily position is more than three times the mean error for the whole time series. We then took a 3-day moving mean to identify and remove any outliers, defined as daily solutions that are 3σ from the moving-average. If an event had more than 5 days removed, we did not include that station for that event. However, if 5 days or less were removed and those days were not within 5 days of the peak of tremor, we replaced the missing data using linear interpolation. Network GPS solutions often exhibit broad regional signals that are non-tectonic in origin (e.g.

atmospheric water vapor) that show up as coherent signals across the network (S. Williams et al., 2004). To remove these, we applied a common mode filter, in which we averaged the time series for 16 stations below 47.5°N latitude, which are well out of the area of expected deformation, and then subtracted that signal from all the stations in the network. See the supplementary materials for more information. Finally, we demeaned all of the time series prior to stacking.

4.5.2 *Results*

Once all the GPS time series were processed for the 9 events, we stacked them and calculated the offsets for the east and north components (Figure 5). Each time series for a given station was time-aligned such that the day with peak daily tremor density in a given event was set to be day “zero”. We calculated offsets by the difference between the 10 days before and 10 days after the event, assuming a standard event was four days long. These values were selected by trying possible windows ranging from 0 to 15 days before and after the event and ranging from 3 to 10 days in length, generating 121 possible window choices, and choosing values that minimize the misfit to the predicted surface displacements scaled by a station's distance to the centroid of the patch. Some stations did not have complete time series during all the events. Therefore, all offsets were then stacked and normalized by the number of events where a given station had data. For individual time series, the offset is generally masked by noise and only becomes resolvable once multiple times series are stacked. For example, several GPS stations near Port Townsend observe ~ 4 mm of westward displacement, while stations that are outside the area of tremor produce small and randomly oriented offsets, as expected (Figure 6).

4.5.3 *Forward Model and Sensitivity Test*

We then estimated the errors associated with the stacking of the time series. First, we take the mean of error in daily positions for each station for each event. Then we take the sum *in quadrature* of the average error in daily position for each station for all events in the patch. This produced the stacked error ellipses (Figure 4). Any signals within the ellipse will be obscured by the noise of a given station. As expected, the noisiest stations (eg MKAH) would require a very large signal to be seen above the noise.

As the potential signals are very close to the noise level of GPS, we used our scaled slip distributions for the events to forward model the surface displacement for the 9 events on Patch 5. We used our scaling relationship determined above to convert tremor detections to fault slip, and then used Green's functions generated with Okada (1992) and a discretized fault model (McCrory et al., 2012) to calculate expected surface displacement. This produced predicted cumulative displacement vectors at 61 Pacific Northwest Geodetic Array (PANGA) and the Plate Boundary Observatory (PBO) stations for the 9 stacked events (Figure 4). The vectors represent the expected surface displacement given no noise and can be used as a method of quantitatively validating our offset selection methods. Figure 4 compares the cumulative predicted surface displacements from our tremor-based slip distributions to the minimum signal necessary to be seen above the noise and shows that Patch 5, which is beneath the Olympic Peninsula, has several stations that could potentially produce signals above the stacked station noise of ~5 mm (e.g. P435, P064, P436). This forward modeling of scaled tremor distribution predicts significant stacked surface displacements. A comparison of these displacements to the noise levels shows that there should be a coherent westward signal on the stations closest to the tremor activity.

4.5.4 *Geodetically-observed Average Moment*

Given the stacked surface displacement, we can now estimate the average moment and slip distribution associated with the repeating small SSEs on Patch 5 and compare these to our tremor-scaled slip moment. We followed the methods from Hall et al. (2018) to solve for fault slip based on observed GPS average surface displacements for each station. We performed a non-negative least-squares static inversion to solve for the predicted fault slip as constrained by the average surface displacements. Elastic Green's functions were calculated using Okada (1992) assuming a shear modulus of 30 GPa. A three-dimensional fault model of the Cascadia plate interface was constructed from the McCrory et al. (2012) plate model and discretized into 8 x 8 km subfaults. A second-order Tikhonov regularization was imposed on the slip inversion to minimize fault roughness. Additionally, slip minimization was applied to the edges of the fault model.

The predicted average slip distribution from the scaled-tremor model corresponds to Mw 5.8 with a peak slip of 0.65 cm on a 50 km x 50 km patch. In comparison, the stacked GPS model inversion predicts an average moment of Mw 5.5 with a peak slip of 0.6 cm. The slip from this model is concentrated in a much smaller area (30 km x 30 km) ~ 20 km to the northeast. This is likely due to the underestimation of slip at SC03 by the stacked GPS. Overall, the slip distribution inferred from the observed stacked GPS records underpredicts the tremor-predicted magnitude, area, and peak slip of the average event.

As an additional test to the robustness of the signal, we extracted random time series from 2009 to 2016 on which to select and align GPS signals, choosing new random times for 20 iterations. When we ran the same processing and offset selection methods, we found that the resulting inferred surface displacements were randomly oriented (see the supplementary material). This provides confidence that aligning and stacking the GPS signals of several small/mid-sized events produces a real and spatially coherent signal.

4.5.5 *Comparisons with Strainmeter Data*

As we have shown above, the signals produced by small SSEs (Mw < 6.0) are at the noise threshold for GPS. It is only by stacking nine events that we are just able to resolve a signal above the noise. Therefore, it is useful to consider an independent observation to confirm the deformation and validate our predicted scaling relationships. Borehole strainmeters are highly sensitive, with nanostrain resolution on the order of minutes-to-days. Strainmeters have been shown to see signals from rapid tremor reversals, sub-events within larger ETS events that have ~Mw 5.0 (J. C. Hawthorne et al., 2016). This enhanced sensitivity suggests that nearby strainmeters may be able to record the ~Mw 5.8 SSEs from Patch 5.

We looked at data for three PBO borehole strainmeters along the Olympic Peninsula to see if an individual small event was resolvable. Although strainmeters are capable of capturing small tectonic signals, these tectonic signals can be masked by larger hydrological signals. We, therefore, focused our search on times when there was minimal precipitation, leaving us with one event (8/2 - 9/6/2010). The data were cleaned and processed following the methods of Roeloffs (2010). The strainmeter data were decimated from 10-minute samples to 30-minute samples to coincide with the 30-minute interval of the barometric pressure record. Obvious outliers (points > 2 sigma above the mean) were removed along with obvious spurious steps, which were estimated and corrected for. Then the raw strainmeter output was converted to gauge elongation. Strain is generally thought to respond linearly to the barometric signal. Therefore the barometric signal can be removed using a single coefficient, which can be found on the PBO website as part of their Level 2 data products (Hodgkinson et al., 2013). Lastly, any long-term linear trends were removed.

Least-squares optimization was used to solve for the amplitudes and phases of known tidal constituents in the 34-day strain time series, and these amplitudes and phases were used to construct a tidal correction time series that was subtracted from the data. The gauges were then combined into strains using different subsets of the three gauges because using nominal conversions for tidal calibrations are not very accurate for strainmeters near the coast (Roeloffs, 2010). These subsets were then rotated into an E-N coordinate system based on orientation corrections derived from responses to Love waves (Roeloffs, 2010). In cases where a given subset of channels was too noisy, the subset was excluded from our analysis.

As a test of our scaling relationships, we created tremor-scaled synthetic time series where the cumulative strain is calculated at the same 30 min sampling interval as the strain data. The strain Green's functions were calculated using the same methods as the displacement Green's functions. For all plots, we use the convention where extension is positive. We found that for a single SSE, our tremor-scaled strains are comparable to the observed strains, suggesting our simple linear scaling relationship effectively reproduces the observed strains (Figure 8).

The clearest signals are seen on B005 and B007, which are collocated and positioned above most of the tremor activity (Figure 8). We included data from B004, which is located ~100 km west of the tremorgenic area, to illustrate that there is little to no observed strain signal that far from the slipping region. This is also predicted by our tremor-scaled strains. Most of the strain signal (15-20 nanostrain) is observed on γ_1 with very little signal predicted or observed on γ_2.

The clear signal of an individual small SSE on the strainmeter allows us to discern which of our scaling relationships best represent the observations. As described above, we had two potential cases: 1) the total moment is equally distributed to every tremor (full-moment case) or 2) the ratio for each fault patch of tremor detections to fault slip is calculated individually and then averaged (slip case). Figure 8 shows the comparison of the predicted strain times given the two scaling models, as well as the average of the two scaling factors. We see that, to first order, both scaling relationships effectively capture the sign and magnitude of strain on multiple stations. However, the full-moment model does the best job of reproducing the observed strains.

For further validation of the full-moment scaling relationship, we looked for a large event that was in a different patch. We chose an event whose predicted scaled magnitude was Mw 5.88 and performed a similar analysis to events in Patch 5. This event on Patch 6 is located further south near the southern end of the Puget Sound, providing a check of our scaling relationship to show that it works for multiple events and multiple patches. In this area, there is only one strainmeter located close enough to observe the event, B018. Figure 9 shows the observed and tremor-predicted strains. Once again, we see that both of our scaling relationships for tremor to slip successfully captures the orientation of strain for a ~Mw 5.9 event. This provides confidence in generalizing our scaling relationship and the completeness of our clustered tremor catalog. Our strainmeter observations for both patches show that our full-moment scaling factor best predicts the observed strains. As a reminder, one of the base assumptions, in this case, was that the moment was equally divided between all the tremor. Our full-moment case supports the idea that to first order each tremor contributes equally to surface deformation.

Our strainmeter observations prefer the full-moment case. This case assumed that tremor amplitudes, and therefore energy, during small SSEs is about 50% of the amplitude of large

SSEs. If we consider tremor to be a superposition of LFEs (Shelly et al., 2007), this potentially suggests that there are fewer LFEs contributing to each tremor. This is supported by the observations of Sweet et al, (2019) who show that only the largest SSEs activate the updip LFE families. Further work is needed, potentially with the aid of strainmeters, to parse the influence of tremor amplitude on scaled slip distributions.

4.6 DISCUSSION

Our scaled tremor catalog suggests that small SSEs at least partially fill the gap between seismically-observed and aseismically-observed slow earthquakes. We have shown that noise-reduction techniques applied to GPS time series, such as stacking, are necessary to resolve SSEs with Mw < 6.0. By stacking 9 events, the data are at the threshold of resolving a Mw 5.8 event. As noted previously, Sekine et al. (2010) were able to resolve events as small as Mw 5.4 using tiltmeter data in Japan. However, strainmeters are capable of clearly observing events with Mw < 6.0, and we observed an individual Mw 5.8 event that produced ~20 nanostrain. Although strainmeters are very useful for confirming the timing and size of a known event, the lack of a dense spatial array makes them less useful for determining overall slip distributions.

If we consider an event with moment an order of magnitude smaller, it would produce strains that are right at the noise level of the strainmeters, barring any spurious noise signals. Hawthorne et al. (2016) observed rapid tremor reversals (~Mw 5.0) in the strainmeter data, which is approximately the predicted magnitude of our smallest events from the clustered tremor catalog. Therefore, we would expect that strainmeters could, given the right meteorological conditions and proximity to the event, observe the majority of the SSEs in our catalog that are below the geodetically observable threshold for GPS. Figure 3 confirms that there are events within this observational "gap" and that the largest events (Mw > 5.6) follow a Mo ~ T scaling relationship similar to the well-known scaling of larger slow earthquakes (Ide et al., 2007). However, as do (Gomberg et al., 2016), we observe a bend in our events (Figure 3). This is interpreted as due to the bounded vs. unbounded nature of large vs. small events.

As noted previously, Figure 3 shows that there still is a gap in our catalog between the smallest SSEs (Mw < 4.6) and the threshold of seismic detection for large VLFEs (Mw 3.7) (Ghosh et al., 2015). This is likely due to the limitations of the clustering algorithm, but it also hints at the limitations of the tremor catalog ability to see smaller events. Our smallest events in the catalog have durations of hours and the Wech catalog is made up of 5-minute detection windows. This puts a limit on how far we can push our scaling for smaller events. Recently Frank & Brodsky, (2019) have scaled LFEs in Guerrero, Mexico and found that they scale more similarly to regular earthquakes. However, in their paper, they are comparing LFE amplitude to geodetic moment.

Generally, tremor is thought to be made up of the superposition of many LFEs (Shelly et al., 2007). Therefore, two or three tremor detections, which could be considered noise by the clustering algorithm, could contain numerous clustered LFEs. Although individual LFEs have previously been assigned magnitudes (Ghosh et al., 2015; Sweet et al., 2019; Chestler & Creager, 2017), there are bursts of LFE activity that have yet to be observed geodetically. Given how small individual LFEs are, Mw ~ 1 to 2, they can often only be found through template matching or using arrays of arrays. In Cascadia, the LFE catalog only exists from 2009-2011 when the CAFE array and Array of Arrays were installed and only contains ~35,000 LFEs (Chestler & Creager, 2017b), about an order of magnitude less than the number of tremor detections.

4.7 CONCLUSION

We investigated whether empirical scaling relationships derived from slip and tremor distributions within large SSEs (Mw > 6.0) accurately represent small SSEs (Mw < 6.0). We used known slip distributions from four large SSEs in northern Cascadia (Hall et al., 2018) to calculate two alternative scaling factors: a full-moment case and a slip case. We then clustered the PNSN tremor catalog into 1109 events ranging in scaled-moment magnitude from Mw. 4.5 to 6.5, using the full-moment scaling factor. For Mw > 5.6 these events follow the previously-proposed moment-duration scaling for slow earthquakes, Mo ~ T. The clustered event catalog identifies SSEs within the observational gap between geodetic methods and seismic methods. To validate our tremor-to-slip scaling relationship, we used stacking to push the signal-to-noise ratio of geodetic observations to detect small SSEs (~Mw 5.5 - 6.0). We aligned GPS records at the times of nine small SSEs with durations of 3+ days on a patch beneath the Olympic Peninsula. This patch produces events with an average moment of Mw 5.8, as shown by slip inversions of both stacked GPS displacement offsets and tremor-predicted offsets. Due to the high level of noise of the GPS data, this patch is likely at the threshold for GPS detection. Therefore, we examined nearby strainmeter records to confirm the detection of individual events and to validate our inferred scaling relationship. We found that our tremor-scaled slip distribution accurately predicted the magnitude and sign of strain for two events on two different patches. Specifically, the observed strains are best matched by tremor-to-slip scaling based on the full-moment case. Our results suggest that linear scaling of tremor detections to moment is sufficient to reproduce observed strains. They further suggest that our tremor-scaled catalog is robust and that there are events just below the threshold of geodetic detection which still follow the known Mo ~ T scaling laws for slow earthquakes.

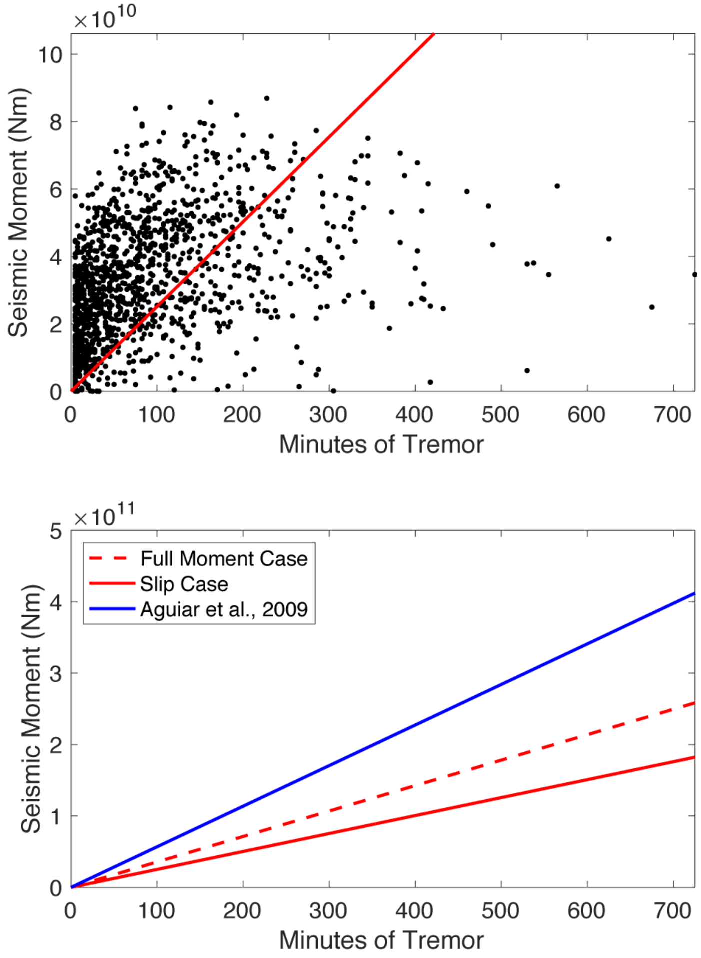

Figure 4.1: (top) A plot of the inverted slip on each 8 km x 8 km fault element (black dot) versus the number of tremor detections in that same element for four large SSEs (August 2010, August 2011, September 2012, December 2015). The solid red line represents best-fit line using the L1 norm constrained to pass through the origin. (bottom) A comparison of the scaling factors used in this analysis and the previous work (blue line) of Aguiar et al., (2009). The dashed red line represents the full-moment case where the entire moment of each of the large SSEs is equally distributed to each tremor. The solid red line represents the slip model found above.

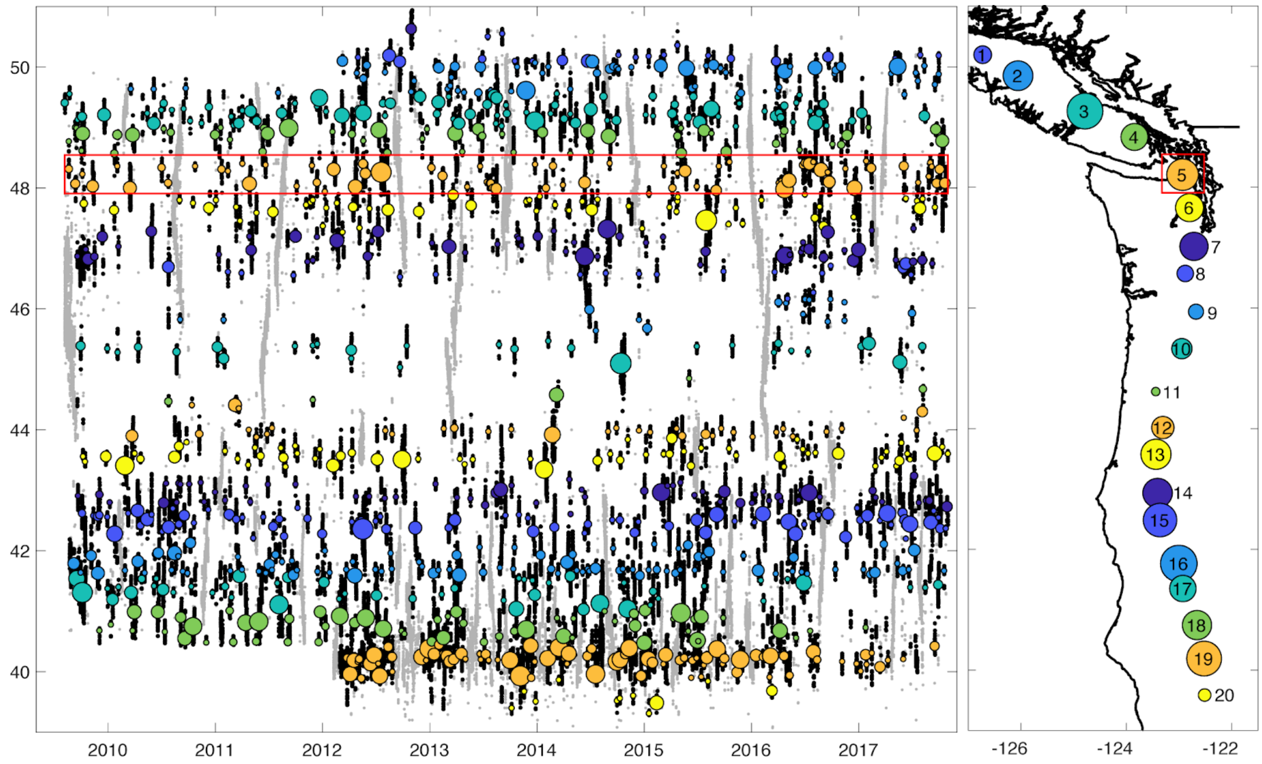

Figure 4.2: A clustered tremor catalog (left) for the Cascadia subduction zone based on tremor locations from the PNSN (black). The catalog is clustered into segments composed of similarly located events (colored circles) whose color corresponds to a patch located on the map (right). On the left, the circle size corresponds to the number of tremors in the cluster. On the right, the circle size corresponds to the number of events in a patch. Events longer than 14 days are considered large SSEs (grey) and are excluded from the map on the right. Our analysis focuses on a patch on the Olympic Peninsula (red box).

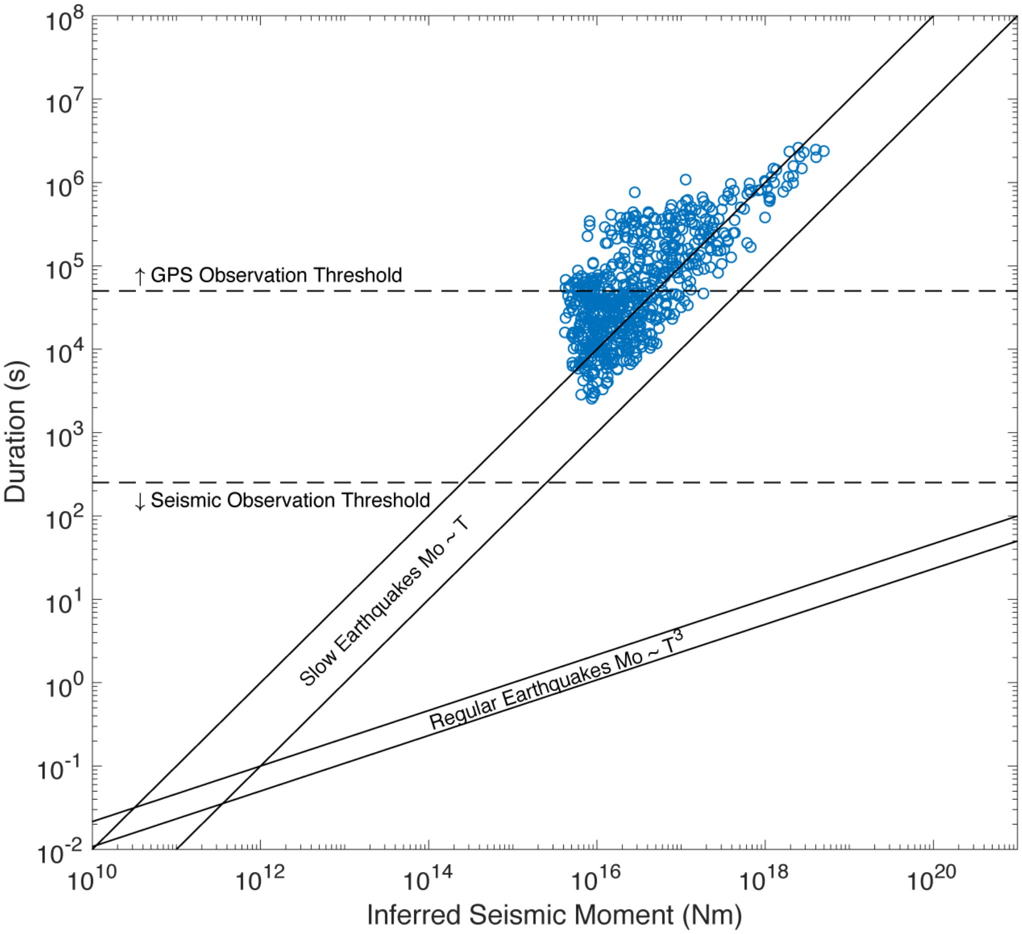

Figure 4.3: A modified version of a figure from Peng & Gomberg (2010), which shows the two scalings between moment and duration (diagonal bands) for regular earthquakes and slow earthquakes. Blue dots represent the inferred moment-durations for the events found from clustering the PNSN tremor catalog. Note that our clustering algorithm requires at least 10 detections to be considered a unique event, which introduces a lower bound to the moments we observe. Solid horizontal lines represent the lower and upper thresholds for geodetic and seismic detection, respectively.

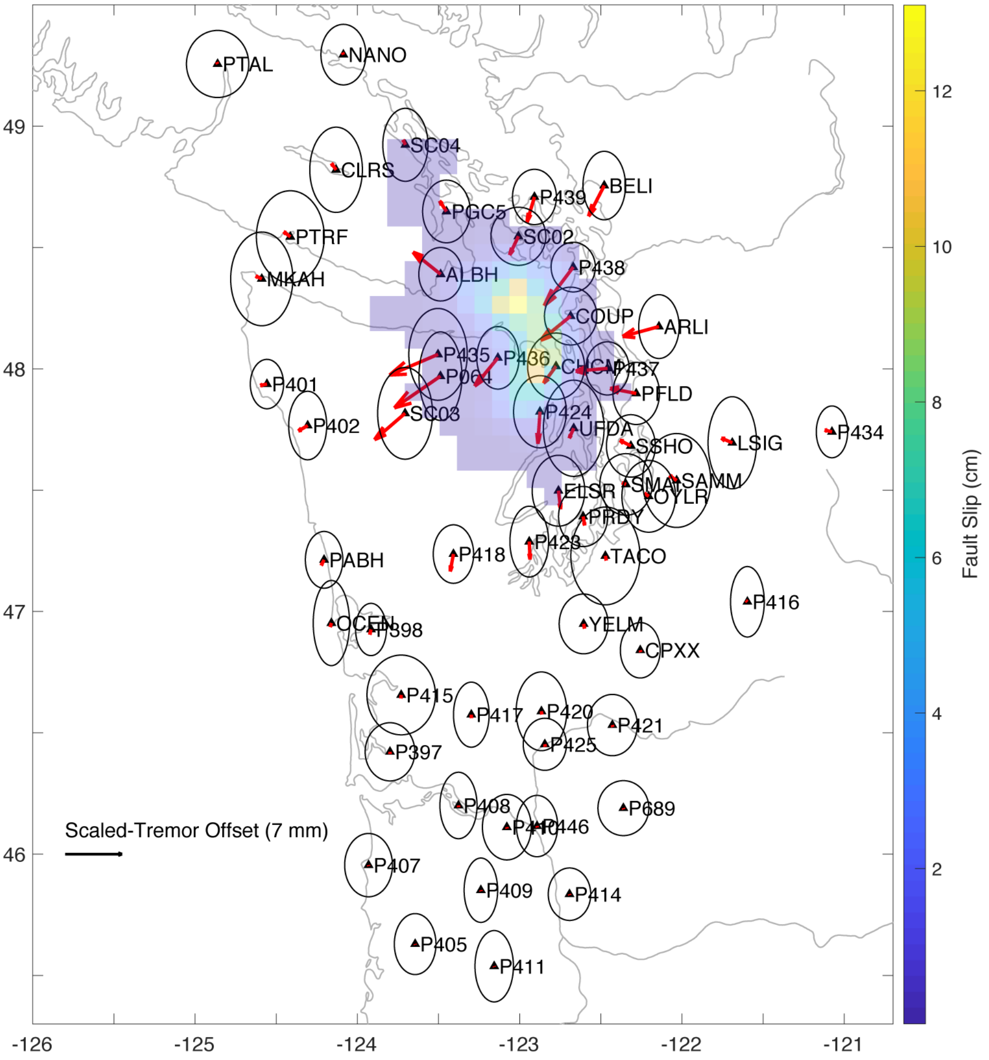

Figure 4.4: A map of synthetic stacked displacements for nine small SSEs for Patch 5, beneath the Olympic Peninsula. The ellipses represent each station's stacked noise levels. Arrows within these ellipses will be indistinguishable from the noise.

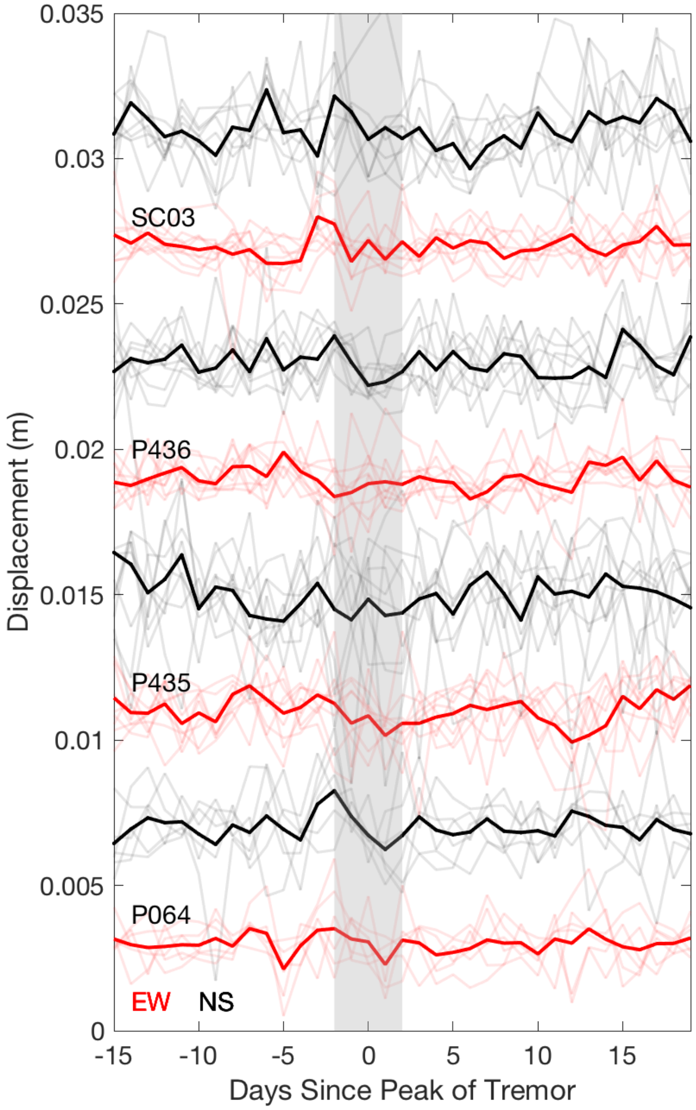

Figure 4.5: Average of the stacked GPS time series (black - NS; red - EW) for nine individual events centered on peak tremor (shaded grey box). Offsets on each component are measured by taking the difference between the average of ten days before and days after the tremor.

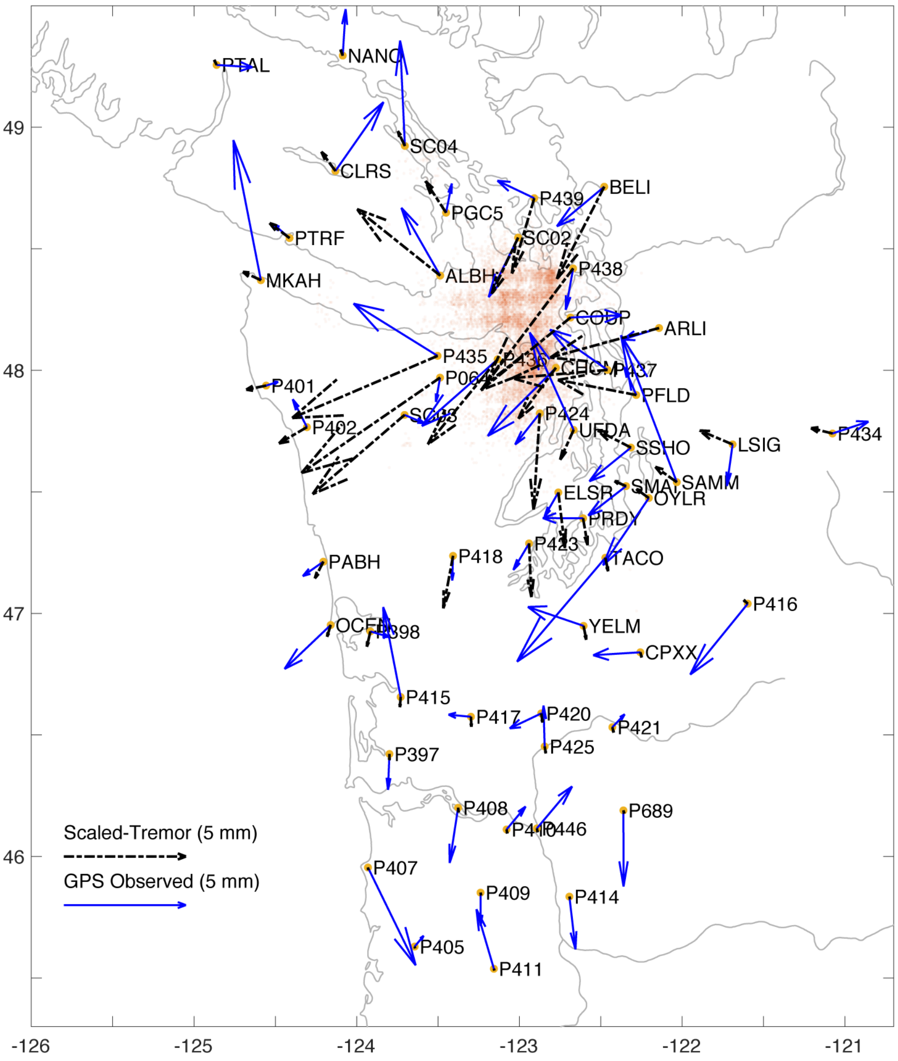

Figure 4.6: A comparison of the synthetic stacked offsets (dashed black) and the observed stacked offsets (blue) for nine events. Stations near the peak tremor activity (orange dots) show coherent westward displacement. Stations outside this area are either randomly oriented or close to zero. Note that the recto-linear pattern in the tremor detections (orange dots) is an artifact of the tremor detection algorithm.

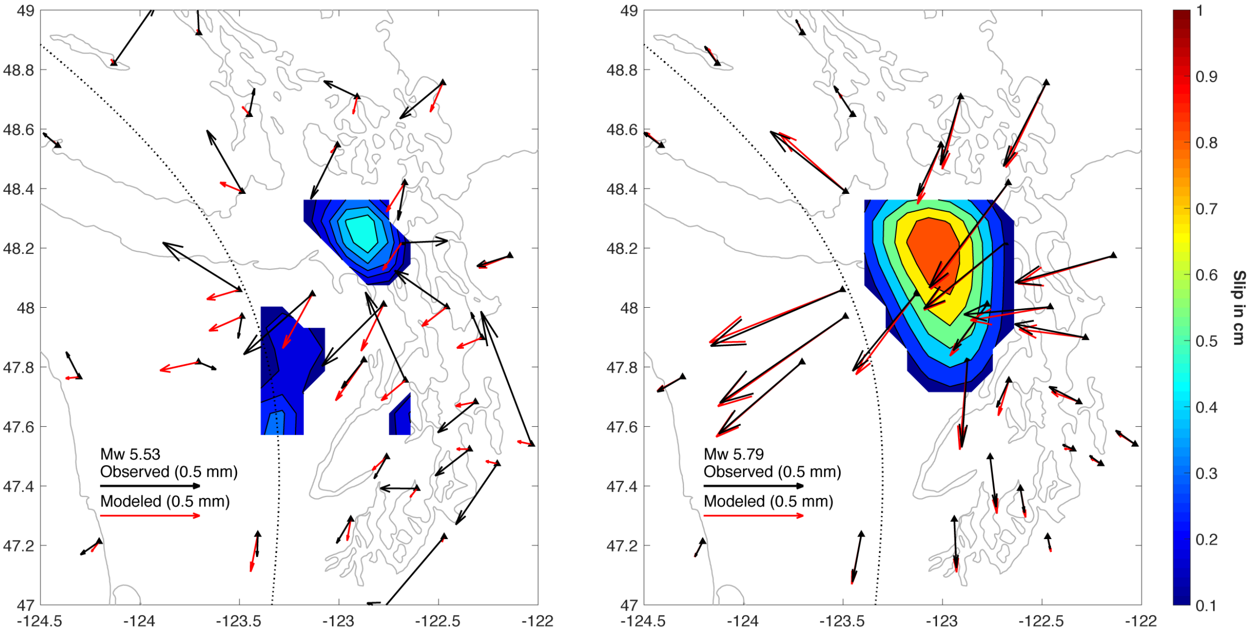

Figure 4.7: Average slip models for the GPS-observed (left) and scaled-tremor (right) displacements from an SSE with a predicted magnitude of Mw 5.8 beneath the Olympic Peninsula. The black arrows show the input displacements as compared to the resulting modeled surface displacements (red). The dashed grey line represents the 35-km depth contour for reference.

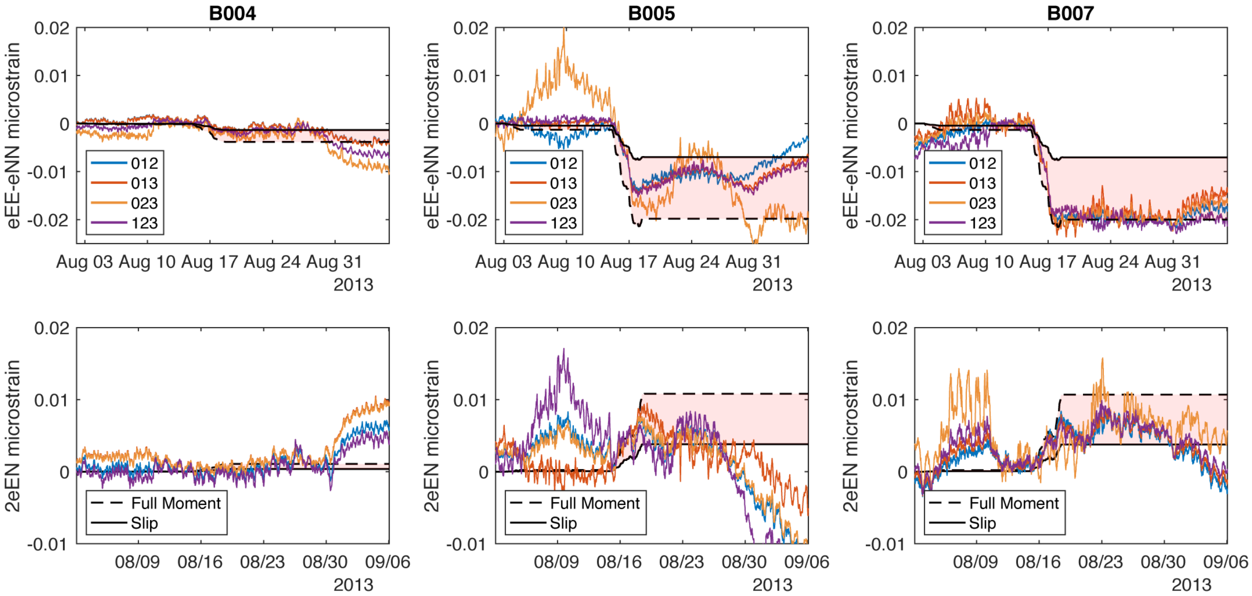

Figure 4.8: A comparison of synthetic strain time series for two different scaling relationships (full moment - dashed black; slip - solid black) to real PBO borehole strainmeter data (colored lines) for both components of shear strain γ_1 (top row) and γ_2 (bottom row) corresponding to a single SSE on Patch 5.

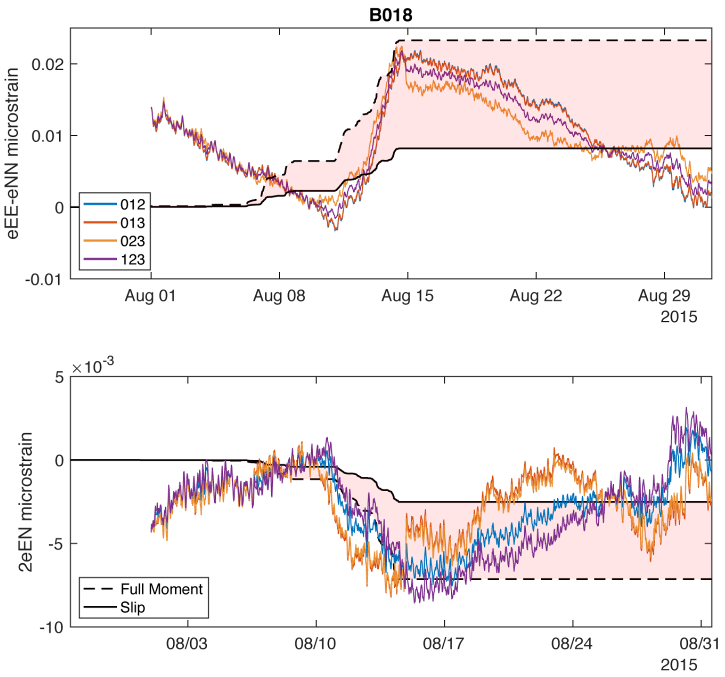

Figure 4.9: A comparison of synthetic strain time series for two different scaling relationships (full moment - dashed black; slip - solid black) to real PBO borehole strainmeter data (colored lines) for both components of shear strain γ_1 (top row) and γ_2 (bottom row) corresponding to a single SSE on Patch 6.

Chapter 5. SUMMARY AND FUTURE WORK

This chapter summarizes findings presented in the previous three chapters and presents potential future avenues of research suggested by this dissertation. This work seeks to test the limits of assuming that tremor can serve as a proxy for slow slip. I confirmed that, to first order, tremor is a sufficient proxy for slow slip. However, it is the instances when this proxy breaks down that we are able to deepen our understanding of either the underlying state of the fault or of the mechanics that drive slow slip and tremor.

This work depended on geodetic observations (GPS and strainmeters) to help quantify the spatial and temporal patterns of slip on the plate interface and constrain seismic moment release. These empirical observations and findings only represent behavior for a single subduction zone. There remain outstanding questions about the universality of these observations that can only be answered by further laboratory tests, modelling, and study of other subduction zones.

Both Chapters 2 and 3 explore instances when tremor is not a perfect proxy for slow slip. In Chapter 2, I found that there is persistent slow slip occurring up dip of tremor during large slow slip events in northern Cascadia. This is likely due to increasing fault strength up dip, which requires increasingly greater stress perturbations to generate brittle failure. This observation serves as a test case for the modeling community to attempt to reproduce persistent up dip slow slip. The Olympic Peninsula is shown to play host to the majority of the updip slip. This is likely due to the lithology of the overriding Olympic Accretionary Complex. This chapter suggests that either changes in permeability or composition of the overriding crust could alter the strength of the fault and change the behavior of tremor and slow slip. In particular, looking to other subduction zones across the world to see how lithology influences tremor and slow slip behavior. Additionally, further laboratory studies to test the influence of these characteristics on fault strength. Typical laboratory frictional experiments are on a relatively small (< 1 m) spatial scale and on relatively homogenous rock. However, we know that subduction zones are very heterogeneous (Fagereng et al., 2018). Our results suggest that the heterogeneous nature of the lithology leads to the range of slow slip behaviors. Perhaps larger scale rock samples with a more heterogeneous composition may provide insight to where and when slow slip and tremor are happening.

In Chapter 3, I found tremor leads peak slip rates during the propagation of large SSEs in northern Cascadia. I suggest that some tremor is triggered by driving stresses ahead of the propagating slip pulse, but given the smoothing required for a time-dependent inversion, it is difficult to say this definitively. In addition to tremor leading peak slip rates, we also observed significant ongoing slip after the main tremor front passed through a region. When compared with the modeling work of Nakata et al. (2011), tremor leading peak slip rates is suggestive of widening of the slip pulse and propagation in a crack-like manner.

One of the limitations of this analysis was the temporal resolution of the daily GPS positions. Tremor detections consist of 5-minute moving windows in the Wech (2008) method and contain much more detail than can be observed by daily GPS. As I showed in Chapter 4, the temporal resolution of strainmeters is much finer (~30 min) than daily GPS. In addition, strainmeters are very sensitive to the relative location of slip. Therefore, the small array of strainmeters along the Olympic Peninsula seem ideally situated to determine, through future studies, whether some portion of the tremor is being triggered ahead of the propagating slip pulse.

In Chapter 4, I tested empirical scaling relationships based on several assumptions about how tremor is related to slow slip in large SSEs (Mw > 6.0). The goal of this chapter is to determine whether small SSEs scale similarly to large SSEs, and thus whether the scaling law is appropriate over two orders of magnitudes in seismic moment. I found that an empirical linear scaling relationship between tremor and slow slip is capable of reproducing observed strain signals for several Mw 5.8 events. This empirical scaling relationship is tuned specifically to Cascadia using the tremor detection catalog of Wech (2010). An avenue of future research would be to test its viability elsewhere along the subduction zone as well as comparing to other subduction zones.

On the macro scale (10s of km and days-weeks) slow slip and tremor are good proxies for one another. On finer temporal and spatial scales, this proxy breaks down. As is suggested in Chestler & Creager (2017), the actual fault structure is likely very heterogeneous with stronger more brittle fault patches surrounded by a more ductile matrix. This is supported by evidence in exhumed subduction zones (Fagereng et al., 2018). Our results suggest that future studies of instances where there is not a good one-to-one correlation between tremor and slow slip will provide greater insight into the state of the subduction zone.

BIBLIOGRAPHY

Aguiar, A. C., Melbourne, T. I., & Scrivner, C. W. (2009). Moment release rate of Cascadia tremor constrained by GPS. *Journal of Geophysical Research: Solid Earth*, *114*(B7), B00A05. https://doi.org/10.1029/2008JB005909

Aki, K., & Richards, P. G. (2002). Quantitative Seismology, 2nd Ed. *Quantitative Seismology, 2nd Ed., by Keiiti Aki and Paul G. Richards. Published by University Science Books, ISBN 0-935702-96-2, 704pp, 2002.* Retrieved from http://adsabs.harvard.edu/abs/2002quse.book.....A

Audet, P., & Bürgmann, R. (2014). Possible control of subduction zone slow-earthquake periodicity by silica enrichment. *Nature*, *510*(7505), 389–392. https://doi.org/10.1038/nature13391

Audet, P., & Kim, Y. (2016). Teleseismic constraints on the geological environment of deep episodic slow earthquakes in subduction zone forearcs: A review. *Tectonophysics*, *670*, 1–15. https://doi.org/10.1016/j.tecto.2016.01.005

Audet, P., Bostock, M. G., Christensen, N. I., & Peacock, S. M. (2009). Seismic evidence for overpressured subducted oceanic crust and megathrust fault sealing. *Nature*, *457*(7225), 76–78. https://doi.org/10.1038/nature07650

Audet, P., Bostock, M. G., Boyarko, D. C., Brudzinski, M. R., & Allen, R. M. (2010). Slab morphology in the Cascadia fore arc and its relation to episodic tremor and slip. *Journal of Geophysical Research: Solid Earth*, *115*(B4), B00A16. https://doi.org/10.1029/2008JB006053

Babcock, R. S., Burmester, R. F., Engebretson, D. C., Warnock, A., & Clark, K. P. (1992). A rifted margin origin for the crescent basalts and related rocks in the northern Coast Range Volcanic Province, Washington and British Columbia. *Journal of Geophysical Research: Solid Earth*, *97*(B5), 6799–6821. https://doi.org/10.1029/91JB02926

Bartlow, N. M., Miyazaki, S., Bradley, A. M., & Segall, P. (2011). Space-time correlation of slip and tremor during the 2009 Cascadia slow slip event. *Geophysical Research Letters*, *38*(18), L18309. https://doi.org/10.1029/2011GL048714

Blakely, R. J., Brocher, T. M., & Wells, R. E. (2005). Subduction-zone magnetic anomalies and implications for hydrated forearc mantle. *Geology*, *33*(6), 445–448. https://doi.org/10.1130/G21447.1

Brandon, M. T., Roden-Tice, M. K., & Garver, J. I. (1998). Late Cenozoic exhumation of the Cascadia accretionary wedge in the Olympic Mountains, northwest Washington State. *GSA Bulletin*, *110*(8), 985–1009. https://doi.org/10.1130/0016-7606(1998)110<0985:LCEOTC>2.3.CO;2

Brudzinski, M. R., & Allen, R. M. (2007). Segmentation in episodic tremor and slip all along Cascadia. *Geology*, *35*(10), 907–910. https://doi.org/10.1130/G23740A.1

Chen, C., Zhao, D., & Wu, S. (2015). Tomographic imaging of the Cascadia subduction zone: Constraints on the Juan de Fuca slab. *Tectonophysics*, *647–648*, 73–88. https://doi.org/10.1016/j.tecto.2015.02.012

Chestler, S. R., & Creager, K. C. (2017a). A Model for Low-Frequency Earthquake Slip. *Geochemistry, Geophysics, Geosystems*. https://doi.org/10.1002/2017GC007253

Chestler, S. R., & Creager, K. C. (2017b). Evidence for a scale-limited low-frequency earthquake source process. *Journal of Geophysical Research: Solid Earth*, *122*(4), 2016JB013717. https://doi.org/10.1002/2016JB013717

Christensen, N. I. (1996). Poisson's ratio and crustal seismology. *Journal of Geophysical Research: Solid Earth*, *101*(B2), 3139–3156. https://doi.org/10.1029/95JB03446

Dragert, H., Wang, K., & Rogers, G. (2004). Geodetic and seismic signatures of episodic tremor and slip in the northern Cascadia subduction zone. *Earth, Planets and Space*, *56*(12), 1143–1150.

Fagereng, Å., Diener, J. F. A., Meneghini, F., Harris, C., & Kvadsheim, A. (2018). Quartz vein formation by local dehydration embrittlement along the deep, tremorgenic subduction thrust interface. *Geology*, *46*(1), 67–70. https://doi.org/10.1130/G39649.1

Fisher, D. M., & Brantley, S. L. (2014). The role of silica redistribution in the evolution of slip instabilities along subduction interfaces: Constraints from the Kodiak accretionary complex, Alaska. *Journal of Structural Geology*, *69*, 395–414. https://doi.org/10.1016/j.jsg.2014.03.010

Frank, W. B., Shapiro, N. M., Husker, A. L., Kostoglodov, V., Bhat, H. S., & Campillo, M. (2015). Along-fault pore-pressure evolution during a slow-slip event in Guerrero, Mexico. *Earth and Planetary Science Letters*, *413*, 135–143. https://doi.org/10.1016/j.epsl.2014.12.051

Frank, William B., Radiguet, M., Rousset, B., Shapiro, N. M., Husker, A. L., Kostoglodov, V., et al. (2015). Uncovering the geodetic signature of silent slip through repeating earthquakes. *Geophysical Research Letters*, *42*(8), 2015GL063685. https://doi.org/10.1002/2015GL063685

Ghosh, A., Huesca-Pérez, E., Brodsky, E., & Ito, Y. (2015). Very low frequency earthquakes in Cascadia migrate with tremor. *Geophysical Research Letters*, *42*(9), 2015GL063286. https://doi.org/10.1002/2015GL063286

Giger, S. B., Tenthorey, E., Cox, S. F., & Fitz Gerald, J. D. (2007). Permeability evolution in quartz fault gouges under hydrothermal conditions. *Journal of Geophysical Research: Solid Earth*, *112*(B7), B07202. https://doi.org/10.1029/2006JB004828

Gomberg, J., Wech, A., Creager, K., Obara, K., & Agnew, D. (2016). Reconsidering earthquake scaling. *Geophysical Research Letters*, 6243–6251. https://doi.org/10.1002/2016GL069967@10.1002/(ISSN)1944-8007.2016GRLEDHIGH

Gomberg, Joan. (2010). Slow-slip phenomena in Cascadia from 2007 and beyond: A review. *Geological Society of America Bulletin*, *122*(7–8), 963–978. https://doi.org/10.1130/B30287.1

Hall, K., Houston, H., & Schmidt, D. (2018). Spatial Comparisons of Tremor and Slow Slip as a Constraint on Fault Strength in the Northern Cascadia Subduction Zone. *Geochemistry, Geophysics, Geosystems*, *19*(8), 2706–2718. https://doi.org/10.1029/2018GC007694

Hawthorne, J., & Rubin, A. (2013). Tidal modulation and back-propagating fronts in slow slip events simulated with a velocity-weakening to velocity-strengthening friction law. *Journal of Geophysical Research: Solid Earth*, *118*(3), 1216–1239. https://doi.org/10.1002/jgrb.50107

Hawthorne, J. C., Bostock, M. G., Royer, A. A., & Thomas, A. M. (2016). Variations in slow slip moment rate associated with rapid tremor reversals in Cascadia. *Geochemistry, Geophysics, Geosystems*, *17*(12), 4899–4919. https://doi.org/10.1002/2016GC006489

Hodgkinson, K., Langbein, J., Henderson, B., Mencin, D., & Borsa, A. (2013). Tidal calibration of plate boundary observatory borehole strainmeters. *Journal of Geophysical Research: Solid Earth*, *118*(1), 447–458. https://doi.org/10.1029/2012JB009651

Houston, H. (2015). Low friction and fault weakening revealed by rising sensitivity of tremor to tidal stress. *Nature Geoscience*, *8*(5), 409–415. https://doi.org/10.1038/ngeo2419

Houston, H., Delbridge, B. G., Wech, A. G., & Creager, K. C. (2011). Rapid tremor reversals in Cascadia generated by a weakened plate interface. *Nature Geoscience*, *4*(6), 404–409. https://doi.org/10.1038/ngeo1157

Husker, A. L., Kostoglodov, V., Cruz-Atienza, V. M., Legrand, D., Shapiro, N. M., Payero, J. S., et al. (2012). Temporal variations of non-volcanic tremor (NVT) locations in the Mexican subduction zone: Finding the NVT sweet spot. *Geochemistry, Geophysics, Geosystems*, *13*(3), Q03011. https://doi.org/10.1029/2011GC003916

Hyndman, R. D., & Wang, K. (1993). Thermal constraints on the zone of major thrust earthquake failure: The Cascadia Subduction Zone. *Journal of Geophysical Research: Solid Earth*, *98*(B2), 2039–2060. https://doi.org/10.1029/92JB02279

Ide, S., Shelly, D. R., & Beroza, G. C. (2007). Mechanism of deep low frequency earthquakes: Further evidence that deep non-volcanic tremor is generated by shear slip on the plate interface. *Geophysical Research Letters*, *34*(3), L03308. https://doi.org/10.1029/2006GL028890

Ikari, M. J., Marone, C., & Saffer, D. M. (2011). On the relation between fault strength and frictional stability. *Geology*, *39*(1), 83–86. https://doi.org/10.1130/G31416.1

Jolliffe, I. (2014). Principal Component Analysis. In *Wiley StatsRef: Statistics Reference Online*. John Wiley & Sons, Ltd. https://doi.org/10.1002/9781118445112.stat06472

Kato, A., Obara, K., Igarashi, T., Tsuruoka, H., Nakagawa, S., & Hirata, N. (2012). Propagation of Slow Slip Leading Up to the 2011 Mw 9.0 Tohoku-Oki Earthquake. *Science*, *335*(6069), 705–708. https://doi.org/10.1126/science.1215141

Kitajima, H., & Saffer, D. M. (2012). Elevated pore pressure and anomalously low stress in regions of low frequency earthquakes along the Nankai Trough subduction megathrust. *Geophysical Research Letters*, *39*(23), L23301. https://doi.org/10.1029/2012GL053793

Kodaira, S., Iidaka, T., Kato, A., Jin-Oh, P., & al, et. (2004). High Pore Fluid Pressure May Cause Silent Slip in the Nankai Trough. *Science; Washington*, *304*(5675), 1295–8.

Kostoglodov, V., Husker, A., Shapiro, N. M., Payero, J. S., Campillo, M., Cotte, N., & Clayton, R. (2010). The 2006 slow slip event and nonvolcanic tremor in the Mexican subduction zone. *Geophysical Research Letters*, *37*(24). https://doi.org/10.1029/2010GL045424

Leeman, J. R., Saffer, D. M., Scuderi, M. M., & Marone, C. (2016). Laboratory observations of slow earthquakes and the spectrum of tectonic fault slip modes. *Nature Communications*, *7*, 11104. https://doi.org/10.1038/ncomms11104

Lowry, A. R., & Pérez-Gussinyé, M. (2011). The role of crustal quartz in controlling Cordilleran deformation. *Nature*, *471*(7338), 353–357. https://doi.org/10.1038/nature09912

Matsuzawa, T., Shibazaki, B., Obara, K., & Hirose, H. (2013). Comprehensive model of short- and long-term slow slip events in the Shikoku region of Japan, incorporating a realistic plate configuration. *Geophysical Research Letters*, *40*(19), 5125–5130. https://doi.org/10.1002/grl.51006

McCrory, P. A., Blair, J. L., Waldhauser, F., & Oppenheimer, D. H. (2012). Juan de Fuca slab geometry and its relation to Wadati-Benioff zone seismicity. *Journal of Geophysical Research: Solid Earth*, *117*(B9). https://doi.org/10.1029/2012JB009407

Michel, S., Gualandi, A., & Avouac, J.-P. (2019). Similar scaling laws for earthquakes and Cascadia slow-slip events. *Nature*, *574*(7779), 522–526. https://doi.org/10.1038/s41586-019-1673-6

Nakajima, J., & Uchida, N. (2018). Repeated drainage from megathrusts during episodic slow slip. *Nature Geoscience*, *11*(5), 351–356. https://doi.org/10.1038/s41561-018-0090-z

Obara, K. (2011). Characteristics and interactions between non-volcanic tremor and related slow earthquakes in the Nankai subduction zone, southwest Japan. *Journal of Geodynamics*, *52*(3), 229–248. https://doi.org/10.1016/j.jog.2011.04.002

Obara, K., Hirose, H., Yamamizu, F., & Kasahara, K. (2004). Episodic slow slip events accompanied by non-volcanic tremors in southwest Japan subduction zone. *Geophysical Research Letters*, *31*(23), L23602. https://doi.org/10.1029/2004GL020848

Okada, Y. (1992). Internal deformation due to shear and tensile faults in a half-space. *Bulletin of the Seismological Society of America*, *82*(2), 1018–1040.

Oleskevich, D. A., Hyndman, R. D., & Wang, K. (1999). The updip and downdip limits to great subduction earthquakes: Thermal and structural models of Cascadia, south Alaska, SW Japan, and Chile. *Journal of Geophysical Research: Solid Earth*, *104*(B7), 14965–14991. https://doi.org/10.1029/1999JB900060

Orange, D. L., Geddes, D. S., & Moore, J. C. (1993). Structural and fluid evolution of a young accretionary complex: The Hoh rock assemblage of the western Olympic Peninsula, Washington. *Geological Society of America Bulletin*, *105*(8), 1053–1075. https://doi.org/10.1130/0016-7606(1993)105<1053:SAFEOA>2.3.CO;2

Outerbridge, K. C., Dixon, T. H., Schwartz, S. Y., Walter, J. I., Protti, M., Gonzalez, V., et al. (2010). A tremor and slip event on the Cocos-Caribbean subduction zone as measured by a global positioning system (GPS) and seismic network on the Nicoya Peninsula, Costa Rica. *Journal of Geophysical Research: Solid Earth*, *115*(B10), B10408. https://doi.org/10.1029/2009JB006845

Ozawa, S., Murakami, M., & Tada, T. (2001). Time-dependent inversion study of the slow thrust event in the Nankai trough subduction zone, southwestern Japan. *Journal of Geophysical Research: Solid Earth*, *106*(B1), 787–802. https://doi.org/10.1029/2000JB900317

Peacock, S. M. (2009). Thermal and metamorphic environment of subduction zone episodic tremor and slip. *Journal of Geophysical Research: Solid Earth*, *114*(B8), B00A07. https://doi.org/10.1029/2008JB005978

Rice, J. R., Lapusta, N., & Ranjith, K. (2001). Rate and state dependent friction and the stability of sliding between elastically deformable solids. *Journal of the Mechanics and Physics of Solids*, *49*(9), 1865–1898. https://doi.org/10.1016/S0022-5096(01)00042-4

Roeloffs, E. (2010). Tidal calibration of Plate Boundary Observatory borehole strainmeters: Roles of vertical and shear coupling. *Journal of Geophysical Research: Solid Earth*, *115*(B6). https://doi.org/10.1029/2009JB006407

Rogers, G., & Dragert, H. (2003). Episodic Tremor and Slip on the Cascadia Subduction Zone: The Chatter of Silent Slip. *Science*, *300*(5627), 1942–1943. https://doi.org/10.1126/science.1084783

Saffer, D. M., & Wallace, L. M. (2015). The frictional, hydrologic, metamorphic and thermal habitat of shallow slow earthquakes. *Nature Geoscience*, *8*(8), 594–600. https://doi.org/10.1038/ngeo2490

Schmalzle, G. M., McCaffrey, R., & Creager, K. C. (2014). Central Cascadia subduction zone creep. *Geochemistry, Geophysics, Geosystems*, *15*(4), 1515–1532. https://doi.org/10.1002/2013GC005172

Scholz, C. H. (1998). Earthquakes and friction laws. *Nature*, *391*(6662), 37–42. https://doi.org/10.1038/34097

Sekine, S., Hirose, H., & Obara, K. (2010). Along-strike variations in short-term slow slip events in the southwest Japan subduction zone. *Journal of Geophysical Research: Solid Earth*, *115*(B9). https://doi.org/10.1029/2008JB006059

Shelly, D. R., Beroza, G. C., Ide, S., & Nakamula, S. (2006). Low-frequency earthquakes in Shikoku, Japan, and their relationship to episodic tremor and slip. *Nature*, *442*(7099), 188–191. https://doi.org/10.1038/nature04931

Shelly, D. R., Beroza, G. C., & Ide, S. (2007). Non-volcanic tremor and low-frequency earthquake swarms. *Nature*, *446*(7133), 305–307. https://doi.org/10.1038/nature05666

Song, T.-R. A., Helmberger, D. V., Brudzinski, M. R., Clayton, R. W., Davis, P., Pérez-Campos, X., & Singh, S. K. (2009). Subducting Slab Ultra-Slow Velocity Layer Coincident with Silent Earthquakes in Southern Mexico. *Science*, *324*(5926), 502–506. https://doi.org/10.1126/science.1167595

Sweet, J. R., Creager, K. C., & Houston, H. (2014). A family of repeating low-frequency earthquakes at the downdip edge of tremor and slip. *Geochemistry, Geophysics, Geosystems*, *15*(9), 3713–3721. https://doi.org/10.1002/2014GC005449

Sweet, J. R., Creager, K. C., Houston, H., & Chestler, S. R. (2019). Variations in Cascadia Low-Frequency Earthquake Behavior With Downdip Distance. *Geochemistry, Geophysics, Geosystems*, *20*(2), 1202–1217. https://doi.org/10.1029/2018GC007998

Szeliga, W., Melbourne, T., Santillan, M., & Miller, M. (2008). GPS constraints on 34 slow slip events within the Cascadia subduction zone, 1997–2005. *Journal of Geophysical Research: Solid Earth*, *113*(B4), n/a–n/a. https://doi.org/10.1029/2007JB004948

Tauzin, B., Reynard, B., Perrillat, J.-P., Debayle, E., & Bodin, T. (2017). Deep crustal fracture zones control fluid escape and the seismic cycle in the Cascadia subduction zone. *Earth and Planetary Science Letters*, *460*, 1–11. https://doi.org/10.1016/j.epsl.2016.12.007

Wada, I., Wang, K., He, J., & Hyndman, R. D. (2008). Weakening of the subduction interface and its effects on surface heat flow, slab dehydration, and mantle wedge serpentinization. *Journal of Geophysical Research: Solid Earth*, *113*(B4), B04402. https://doi.org/10.1029/2007JB005190

Wallace, L. M., & Beavan, J. (2010). Diverse slow slip behavior at the Hikurangi subduction margin, New Zealand. *Journal of Geophysical Research: Solid Earth*, *115*(B12), B12402. https://doi.org/10.1029/2010JB007717

Wallace, L. M., Beavan, J., Bannister, S., & Williams, C. (2012). Simultaneous long-term and short-term slow slip events at the Hikurangi subduction margin, New Zealand: Implications for processes that control slow slip event occurrence, duration, and migration. *Journal of Geophysical Research: Solid Earth*, *117*(B11). https://doi.org/10.1029/2012JB009489

Wang, K., Dragert, H., Kao, H., & Roeloffs, E. (2008). Characterizing an “uncharacteristic” ETS event in northern Cascadia. *Geophysical Research Letters*, *35*(15), L15303. https://doi.org/10.1029/2008GL034415

Wech, A. G. (2010). Interactive Tremor Monitoring. *Seismological Research Letters*, *81*(4), 664–669. https://doi.org/10.1785/gssrl.81.4.664

Wech, A. G., & Bartlow, N. M. (2014). Slip rate and tremor genesis in Cascadia. *Geophysical Research Letters*, *41*(2), 2013GL058607. https://doi.org/10.1002/2013GL058607

Wech, A. G., & Creager, K. C. (2011). A continuum of stress, strength and slip in the Cascadia subduction zone. *Nature Geoscience*, *4*(9), 624–628. https://doi.org/10.1038/ngeo1215

Wech, A. G., Creager, K. C., & Melbourne, T. I. (2009). Seismic and geodetic constraints on Cascadia slow slip. *Journal of Geophysical Research: Solid Earth*, *114*(B10), B10316. https://doi.org/10.1029/2008JB006090

Wells, R. E., & Simpson, R. W. (2001). Northward migration of the Cascadia forearc in the northwestern U.S. and implications for subduction deformation. *Earth, Planets and Space*, *53*(4), 275–283. https://doi.org/10.1186/BF03352384

Wells, R. E., Blakely, R. J., Wech, A. G., McCrory, P. A., & Michael, A. (2017). Cascadia subduction tremor muted by crustal faults. *Geology*, *45*(6), 515–518. https://doi.org/10.1130/G38835.1

Williams, C. A., & Wallace, L. M. (2015). Effects of material property variations on slip estimates for subduction interface slow-slip events. *Geophysical Research Letters*, *42*(4), 2014GL062505. https://doi.org/10.1002/2014GL062505

Williams, S., Bock, Y., Fang, P., Jamason, P., Nikolaidis, R. M., Prawirodirdjo, L., et al. (2004). Error analysis of continuous GPS position time series. *Journal of Geophysical Research: Solid Earth*, *109*(B3). https://doi.org/10.1029/2003JB002741

Yabe, S., Ide, S., & Yoshioka, S. (2014). Along-strike variations in temperature and tectonic tremor activity along the Hikurangi subduction zone, New Zealand. *Earth, Planets and Space*, *66*(1), 142. https://doi.org/10.1186/s40623-014-0142-6

APPENDIX 1: SUPPLEMENTARY MATERIALS FOR CHAPTER 2

Text A1.1:

In order to test the robustness of PCA, we performed several tests on synthetic GPS time series. The synthetic time series represents a demeaned yearlong record, which is on the lower end of recurrence intervals for ETS in northern Cascadia (Brudzinski & Allen, 2007). Each record contains a transient offset signal lasting 7 days that occurs halfway through the year. White noise based on the real station errors from the PANGA data set and random walk noise (1 mm/√yr) are added to this idealized signal. We tested how well PCA recovered a range of offsets, as well as how sensitive the method was to the length of the record before and after the transient motion associated with the slow slip (Figure A1.1).

PCA was successful at recovering all offsets, but underestimated the offset with insufficient time before and after the transient, with the ideal time intervals on each side being ~35 days. With shorter time intervals before and after the transient, the data points during the transient begin to outweigh those at the beginning and end that provide stable starting and ending positions. Including very long time intervals before and after the transient would result in little offset detected because of the de-meaned base signal. PCA is also sensitive to uneven amounts of data before and after the transient. Figure A1.2 shows that as the time series becomes more uneven PCA is less accurate at estimating the offset.

Text A1.2:

In order to compare the URI and TRI we performed an F-test to compare the two inversions. The null hypothesis of the F-test is that the two inversions fit the data equally well. In order to perform the F-test we needed to calculate the degrees of freedom. In the most basic least squares inversion, with no smoothing, the problem is under-constrained because there are significantly more model parameters (subfaults) than data. However, we have introduced both smoothing and a border constraint with our Tikhonov Regularization. This means that each model parameter is no longer independent. Therefore, to determine the effective independent model parameters, we performed a checkerboard test, varying the size of the input squares. We then calculated the residuals from all the checkerboards, and made a plot of grid size versus fit (Figure 2.5). We then selected the minimum grid size that had an adequately small residual. We then decimated the number of model parameters by the square of the grid size. Using these new pseudo-degrees of freedom, we then calculated the F-values and compared them to the critical F-value at a 95% confidence level. We found that our F-values significantly exceeded the critical value, as was expected given the factor of two difference in residuals. This gives confidence that the residual norm is a sufficiently robust comparison of the two inversions despite the difference in model size.

Text A1.3:

Using a first-order model of heat flow from the MATLAB PDE Toolbox, we constructed a three-block thermal model consisting of two adjacent blocks (Figure A1.5) with thermal conductivity comparable to the lithologies of the Olympic Accretionary Complex (metamorphosed sediments = 3.62 Wm^{-1}K^{-1}) and the Crescent Terrane (basalt = 4.93 Wm^{-1}K^{-1}) (Robertson, 1988) which both sit atop an oceanic slab. We assumed that there was no convective or advective heat transfer, and that the lateral boundaries of the blocks were completely insulated, and enforced two boundary conditions, setting the temperature at the base of the slab based on thermal models (Hyndman & Wang, 1993) and the temperature at the surface.

Our thermal model shows that meta-sediments closer to the basalt have a higher temperature than those far away from the basalt, and the less conductive meta-sediments have colder temperatures relative to the regions beneath the basalt (Figure A1.5). Our model shows a lateral distance of about +/- 14 km around the boundary between these two materials that is affected by the difference in conduction with a range of 30 °C change in temperature (Figure A1.6). This change in temperature is on the order of magnitude of the change between seismic and aseismic regions in major subduction zones (Brace & Byerlee, 1970).

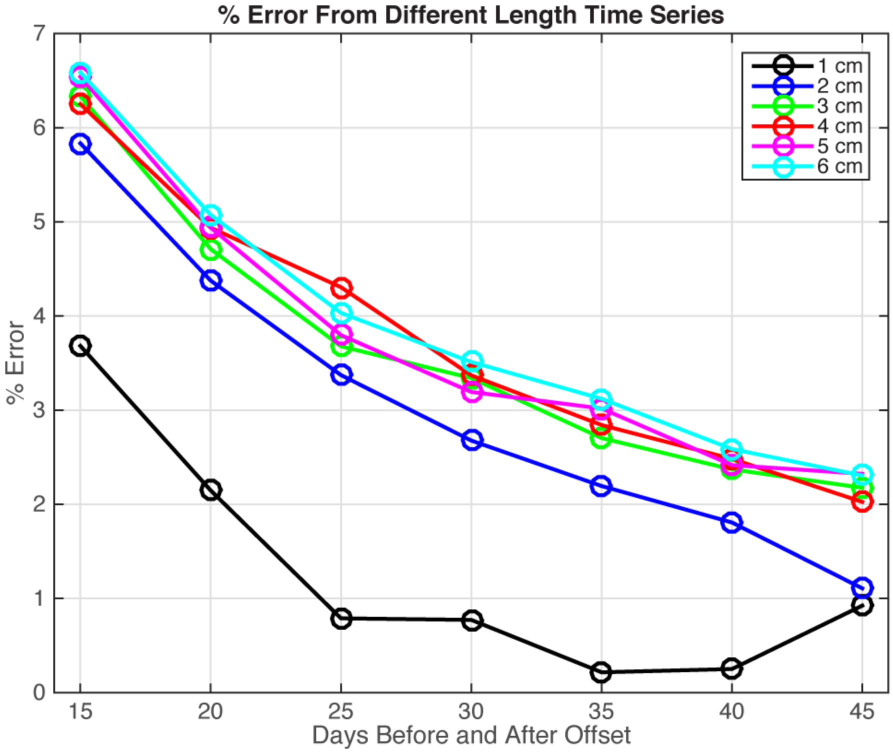

Figure A1.1: A test of the PCA method of offset selection with respect to the number of days in the time series before and after the displacement transient at the station. Each color corresponds to a different amount of slip. As the number of days before and after the offset increases (up to 45), the percent error decreases.

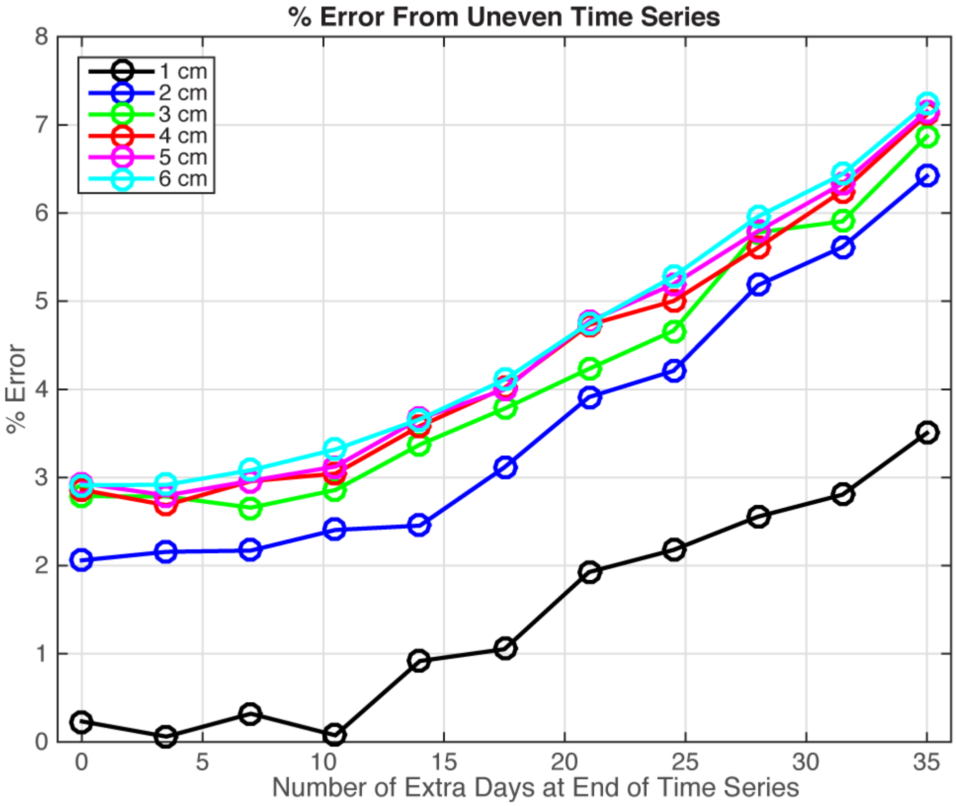

Figure A1.2: A test of the effect of having an uneven length of time before and after the slow slip event. Each color corresponds to a different amount of slip. As unevenness of the time series relative to the timing of the offset increases the percent error of the offset selection increases.

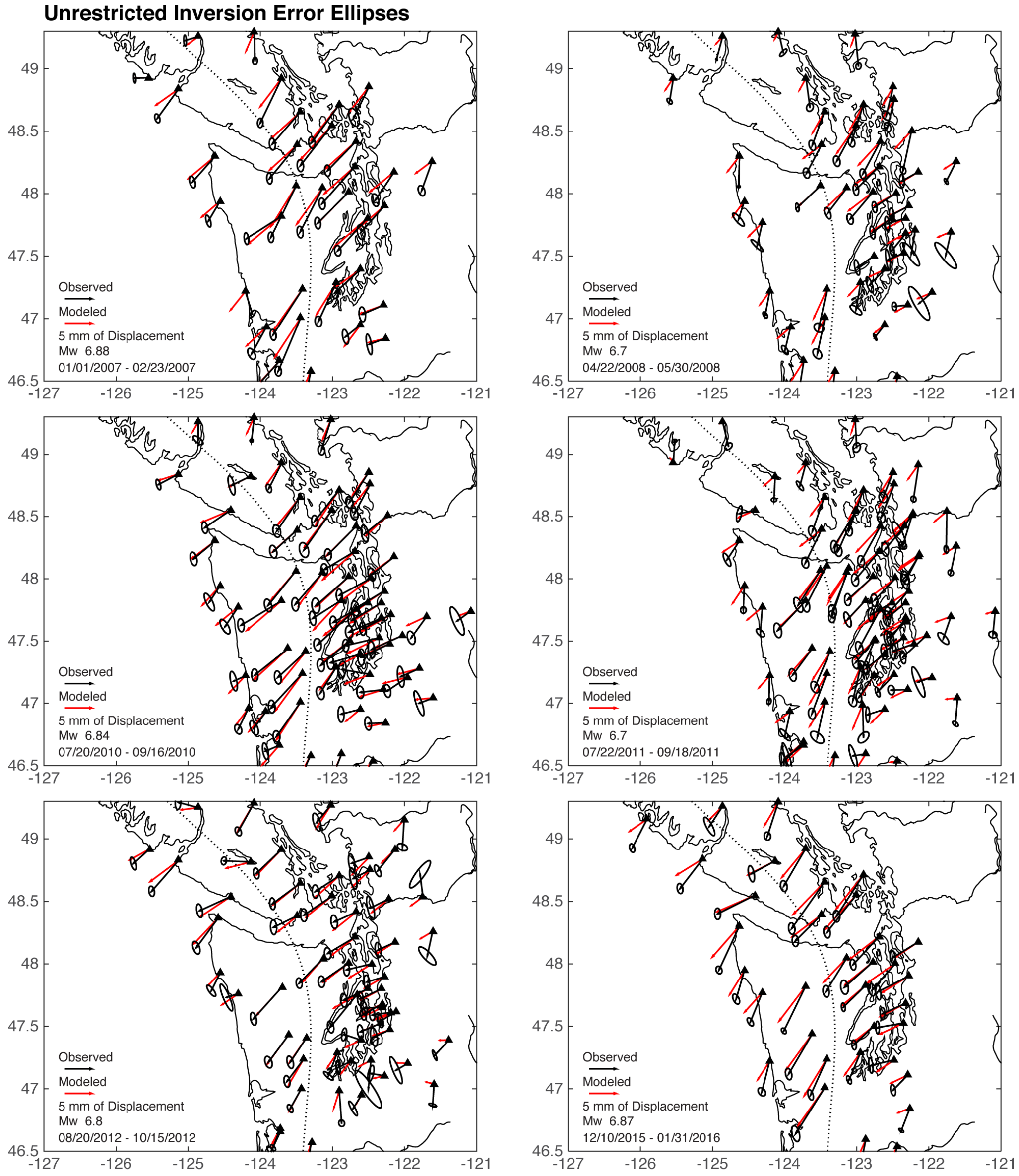

Figure A1.3: Arrows show modeled (red) and observed (black) surface displacements from unrestricted inversions (URI) of slow slip from ETSs between 2007 and 2016, with error ellipses representing the 95% confidence interval of the PCA method. Dashed black line represents the 35 km depth contour of the plate interface.

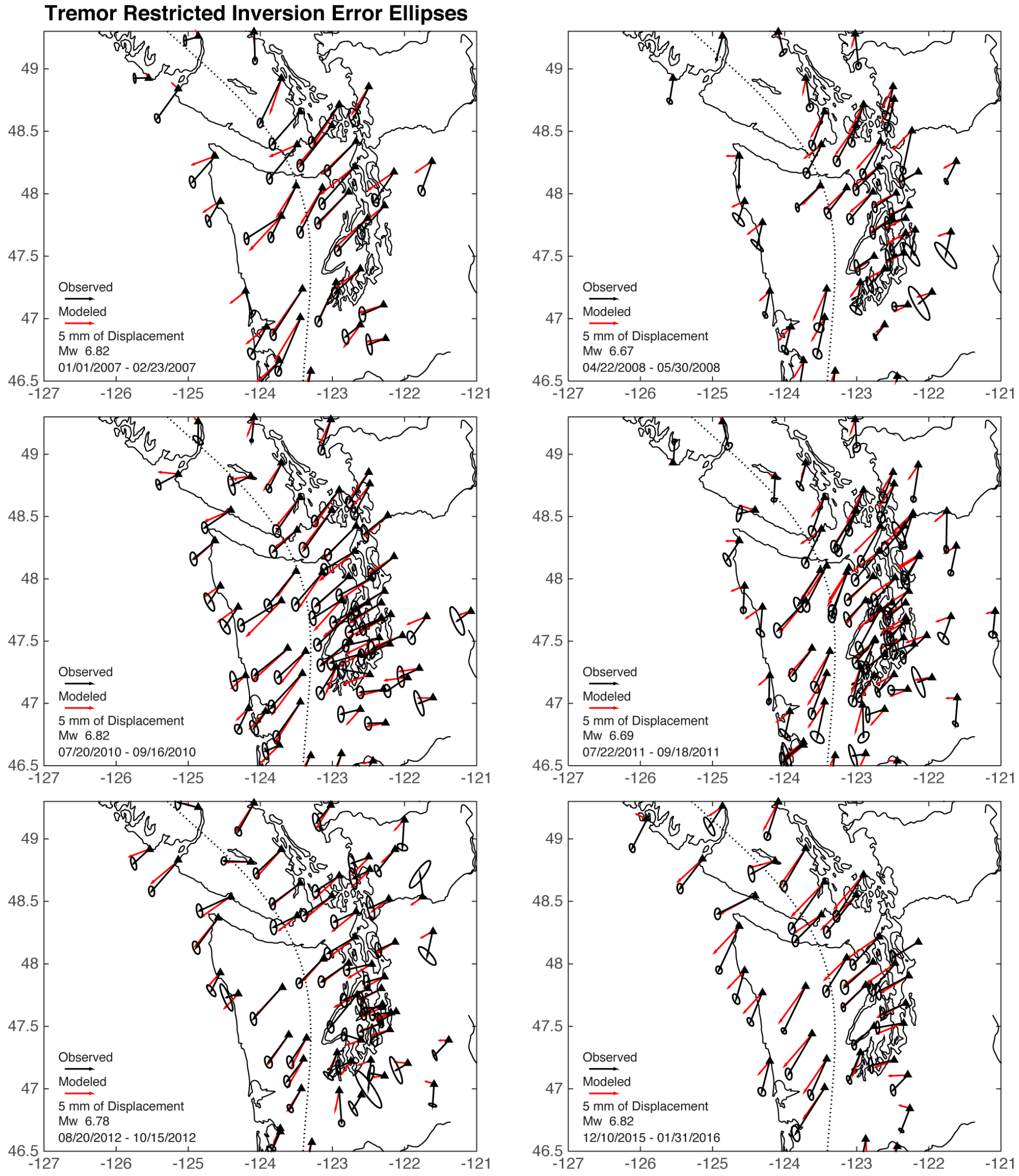

Figure A1.4: Arrows show modeled (red) and observed (black) surface displacements from unrestricted inversions (TRI) of slow slip from ETSs between 2007 and 2016, with error ellipses representing the 95% confidence interval of the PCA method. Dashed black line represents the 35 km depth contour of the plate interface.

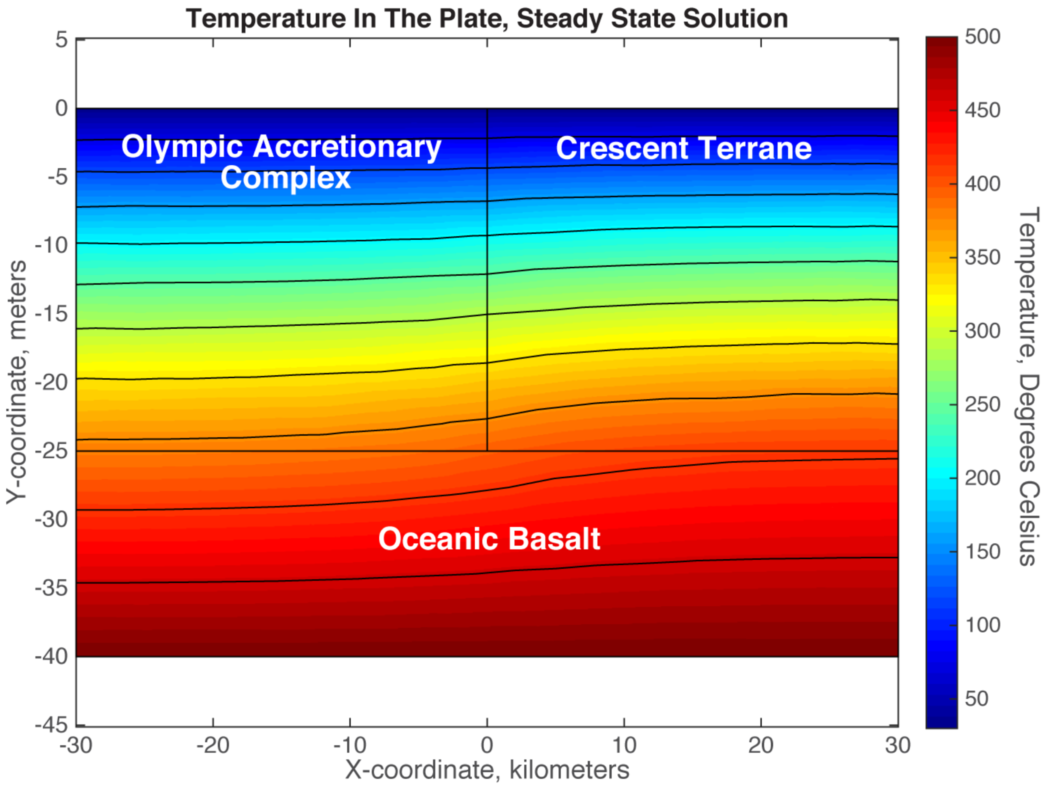

Figure A1.5: Thermal model consisting of three blocks; contours every 40°C. The bottom block represents an oceanic slab with thermal properties of oceanic basalt. The left block represents the accretionary complex beneath the Olympic Peninsula, and the right block represents the basalts of the Crescent terrane. The higher conductivity of the Crescent terrane allows for higher temperatures within and near it.

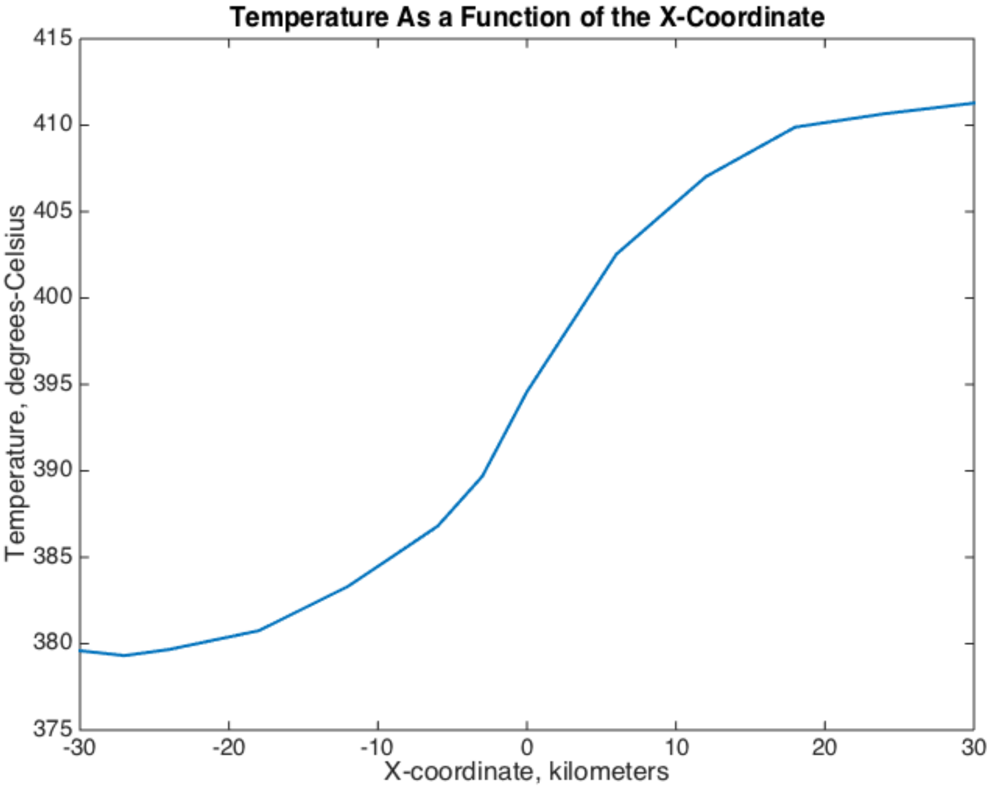

Figure A1.6: A cross-section of temperature across the base of the two blocks. The variation in temperature due to the difference in conduction spans approximately 30 km. Absolute temperatures are dependent on the basal temperature and the thickness of the oceanic slab, but the relative change in temperature and its spatial extent is robust.

APPENDIX 2: SUPPLEMENTARY MATERIALS FOR CHAPTER 3

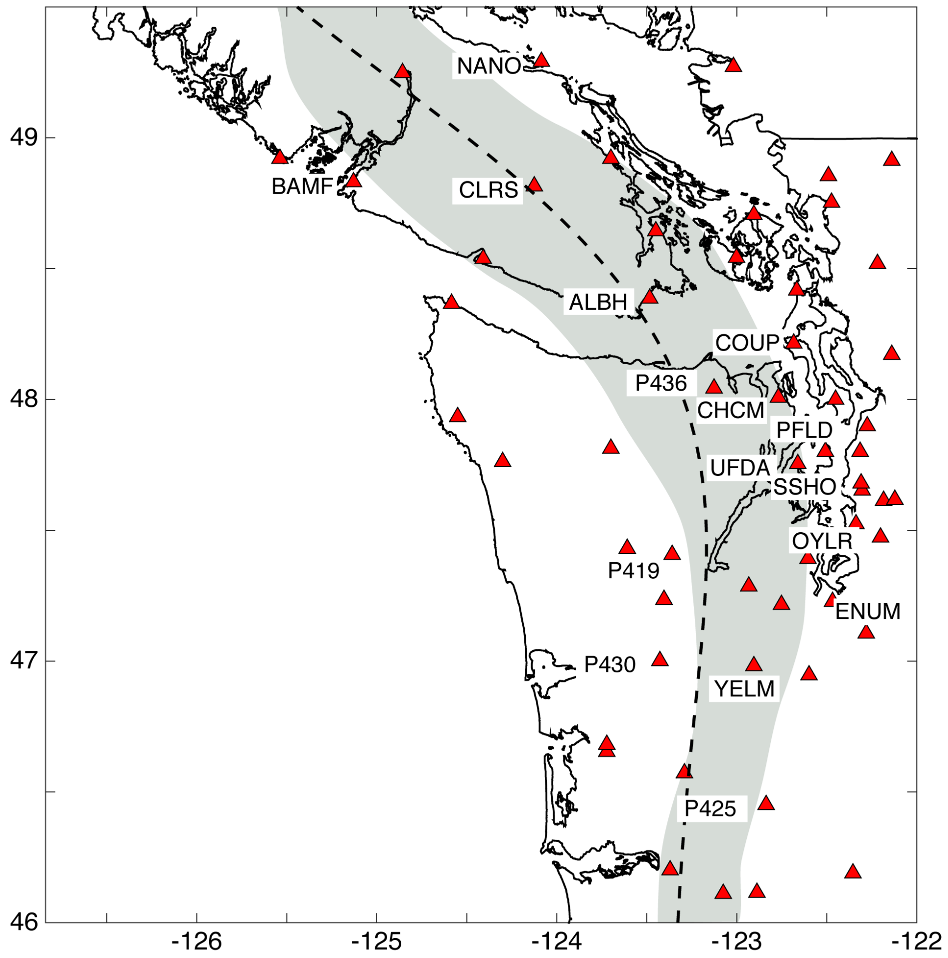

Figure A2.1: GPS stations (red triangles on map) used in the time dependent inversion for the 2010 and 2012 ETS events. Time series fits for the labeled stations are shown in supplementary figures 1 and 2. The gray north-south band on the map denotes the approximate location of tremor. Dashed black line represents the 35 km depth contour

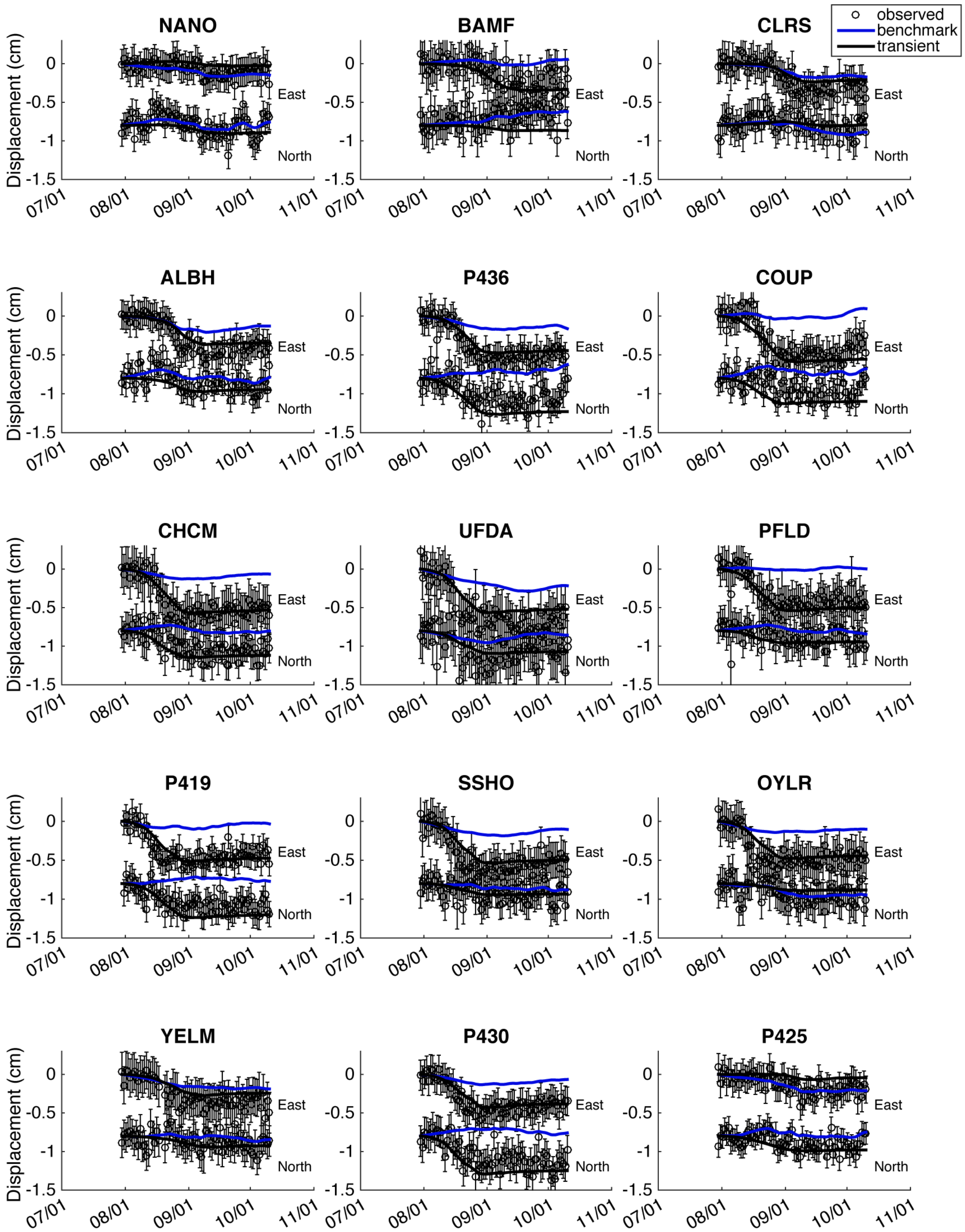

Figure A2.2: Observed (circles) and model predicted (black solid line) surface displacement time series at GPS stations shown in A2.3 for the 2010 slow slip event. Black circles represent observed east and north data with 1σ error bars; with the north component offset by 1 cm for clarity. The blue line represents the predicted predicted benchmark motion from the model.

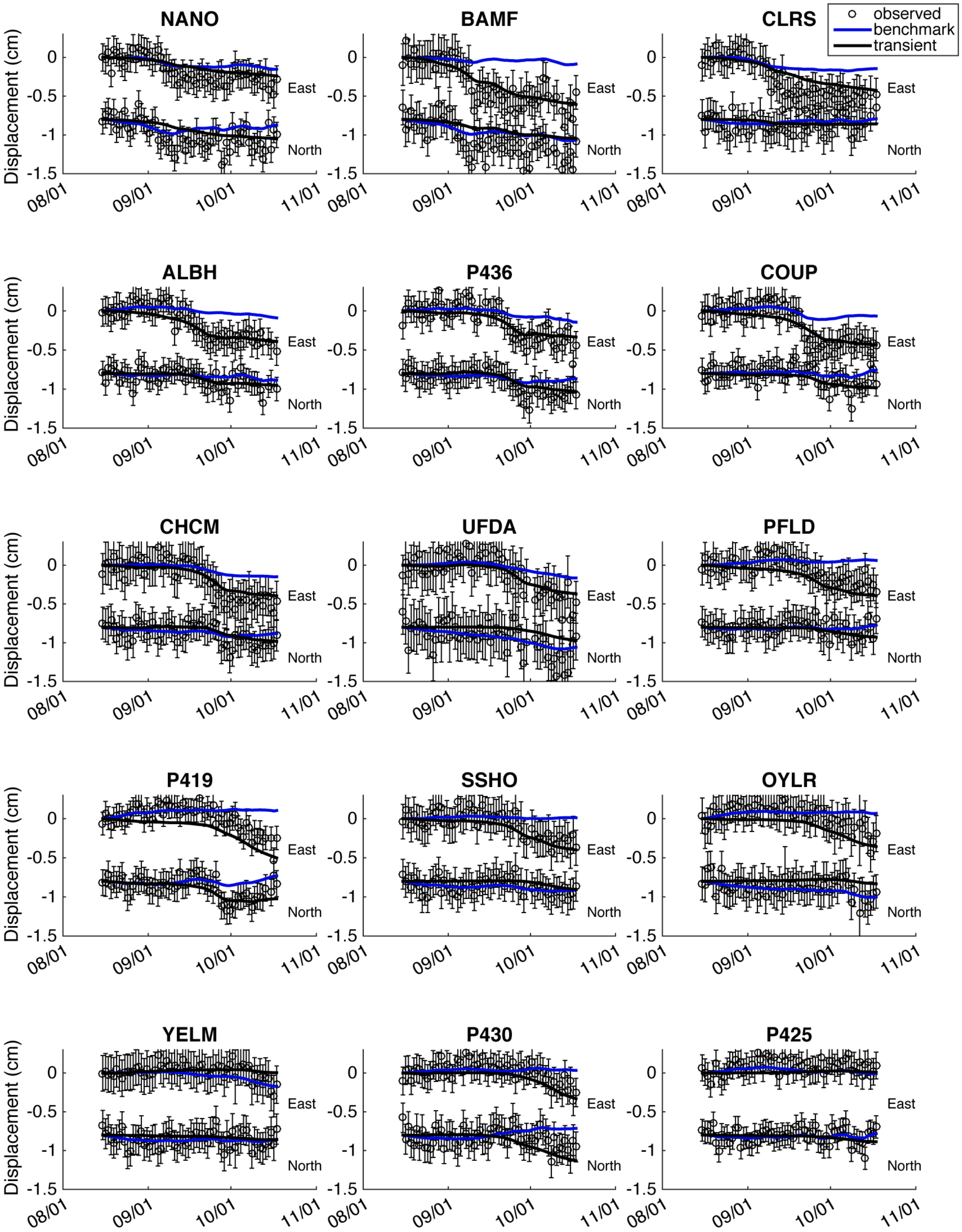

Figure A2.3: Observed (circles) and model predicted (black solid line) surface displacement time series at GPS stations shown in A2.3 for the 2012 slow slip event. Black circles represent observed east and north data with error bars; with the north component offset by 1 cm for clarity. The blue line represents the predicted benchmark motion from the model.

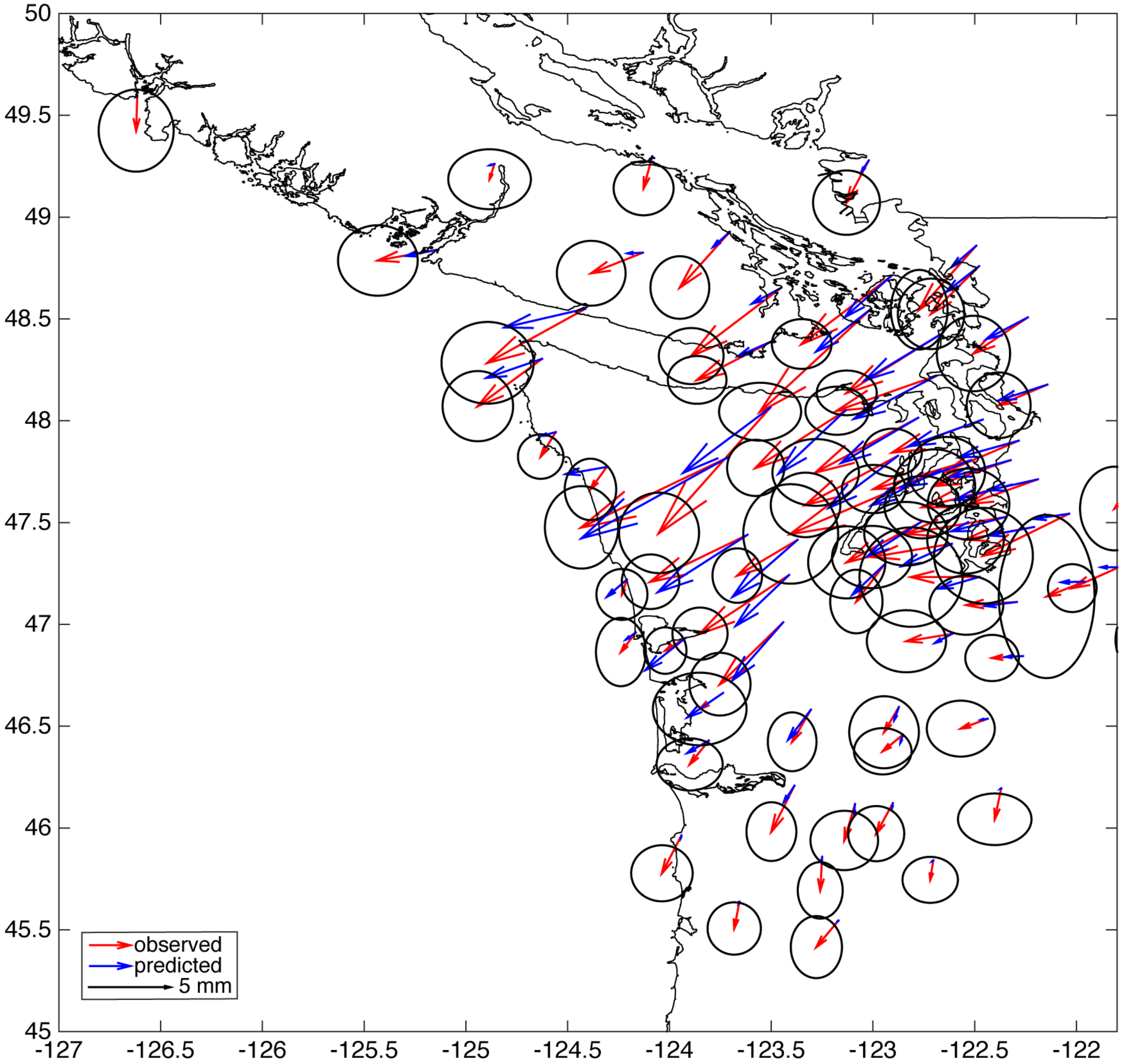

Figure A2.4: A comparison of the observed (red arrows) and predicted (blue arrows) offsets for the 2010 ETS event with 1σ error ellipses (black).

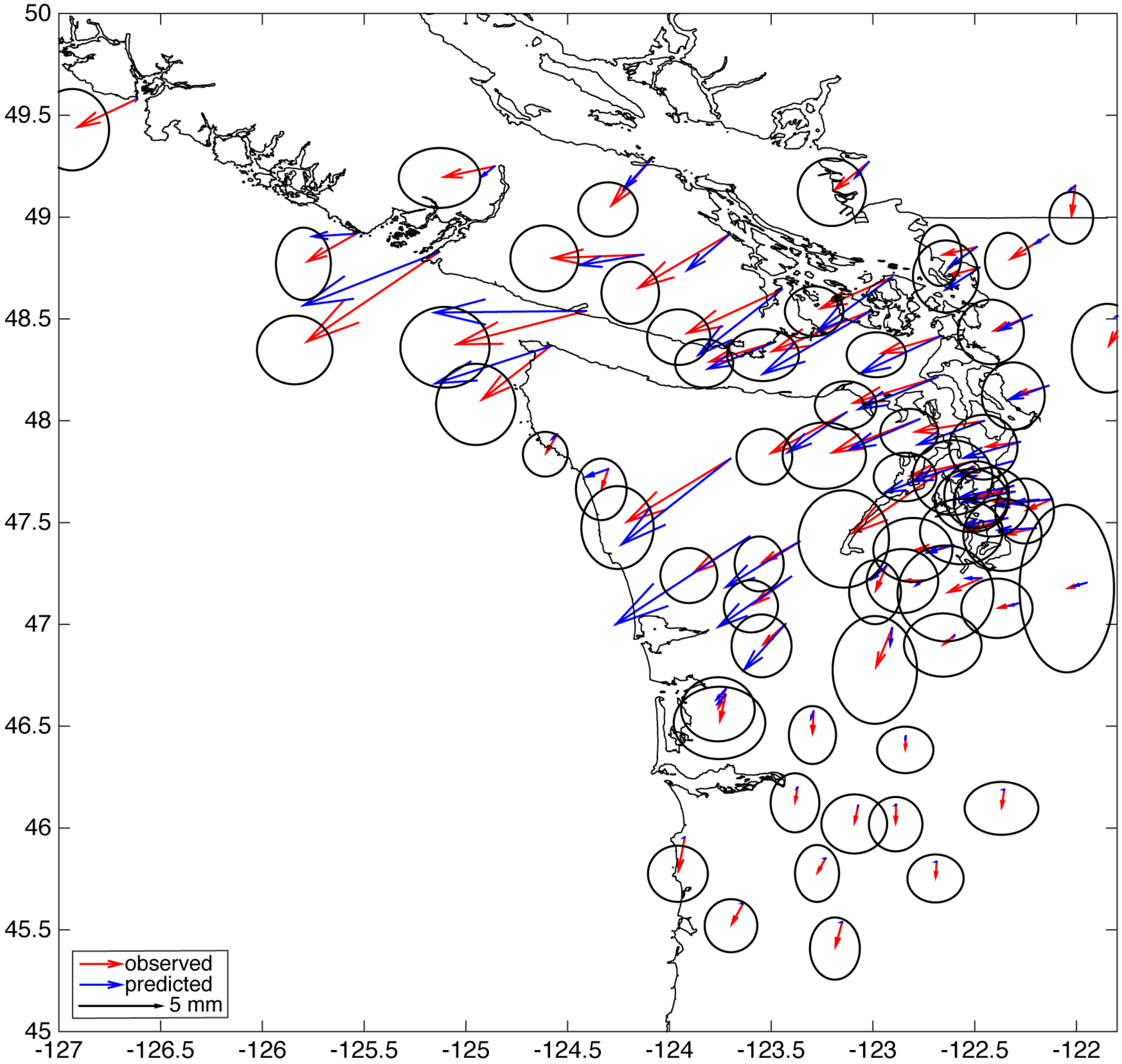

Figure A2.5: A comparison of the observed (red arrows) and predicted (blue arrows) offsets for the 2012 ETS event with 1σ error ellipses (black).

Movie A2.6: A movie of the resulting slip rate distributions generated by using the ENIF on GPS data from PANGA for the 2010 ETS event. The event propagates northward toward Vancouver Island. Each time slice represents the slip rate (cm/day) with a red contour at 0.15 cm/day. Pink dots represent the corresponding total daily tremor locations from the PNSN catalog.

Movie A2.7: A movie of the slip rate distributions generated by using the ENIF on GPS data from PANGA for the 2012 ETS event. The event propagates southward toward the Puget Sound. The 2012 event stalled for several days on the southern tip of Vancouver Island (9/11 - 9/15) before continuing southward.

Text A2.8 Our analysis is highly dependent on the tremor locations in the PNSN catalog. We are confident that our analysis is not influenced by biases in the tremor catalog. In the tremor location method of Wech and Creager (2008), the envelopes of 5-minute windows of seismic signals are cross-correlated. When the tremor is louder, it still tends to wax and wane over times scales of tens of seconds (i.e., much shorter than 5 minutes). Two of the major biases in the catalog occur on the sub-daily time scales. There are more detections in the evenings due to lower noise levels, and detections are modulated by the tides (Houston 2015). The catalog shows continued and, in fact, increased modulation due to tides during ETS slip at a given spot, which suggests that envelope cross-correlation continues to effectively detect tremor locations throughout the ETS.

Additionally, during large ETS events the amplitude of the envelopes is higher (i.e. louder and it is easier to detect) than smaller episodes. We have looked at several times series of tremor and, if anything, the louder periods tend to vary more than the quieter periods, which, at least in Cascadia, do not seem to exhibit more impulsive tremor.

To test the robustness of our observations, we explored several other catalogs of tremor/LFE detections generated with different methods [Ghosh et al., 2010; Peng & Rubin, 2016; Sweet et al., 2019]. Although each of these methods produced somewhat different catalogs, they broadly agree when tremor is binned daily (as we do in our methods). See the figure below for a comparison of our tremor catalog to the Peng & Rubin (2016) catalog. This gives us confidence that our observation of diminished tremor during peak slip is robust.

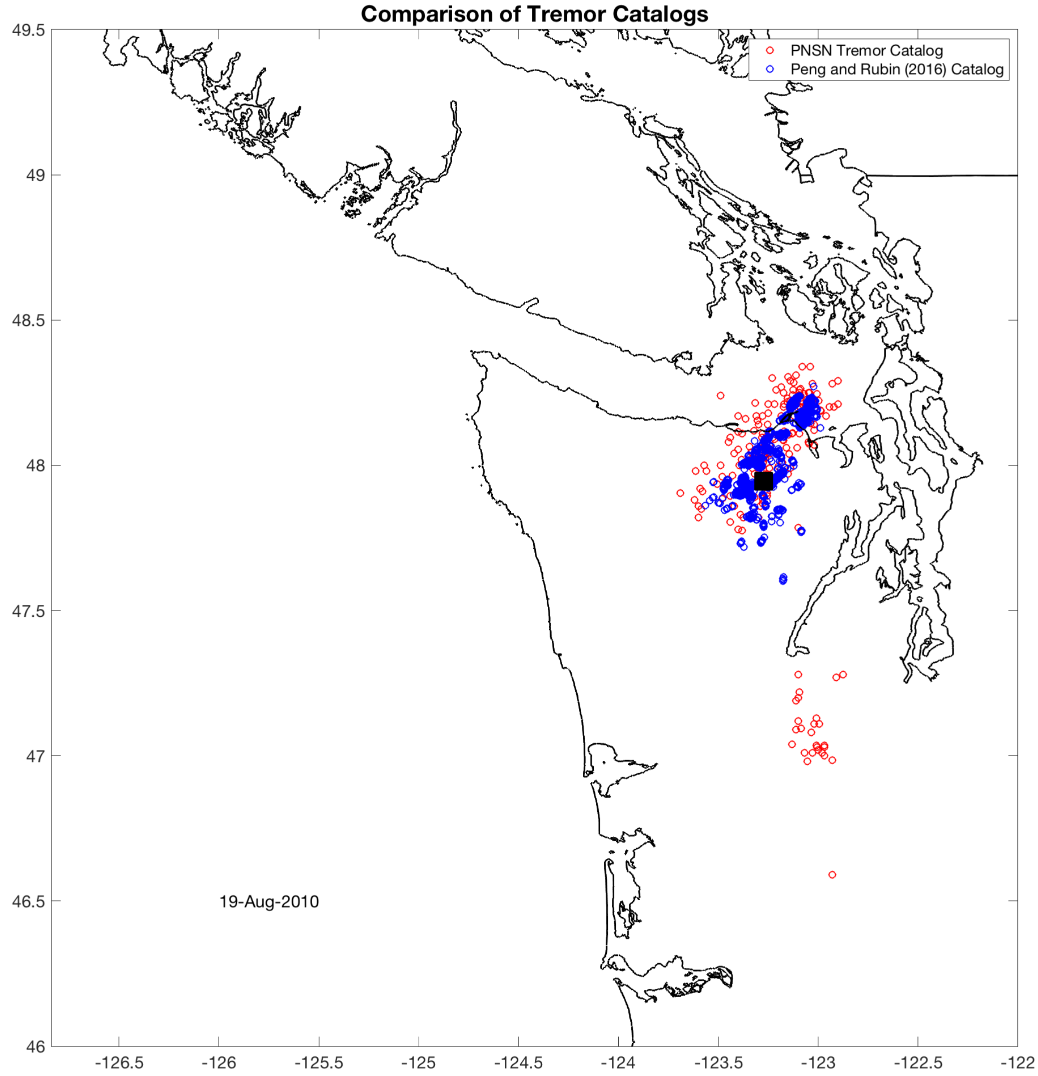

Figure A2.9: A daily slice of tremor locations from two different tremor catalogs. The PNSN catalog (red) is created on the envelope cross-correlation method using the PNSN seismic network. The Peng & Rubin (2016) catalog (blue) is created using cross-correlations of Array of Arrays seismic data. The black square represents the fault patch used for Figure A2.10.

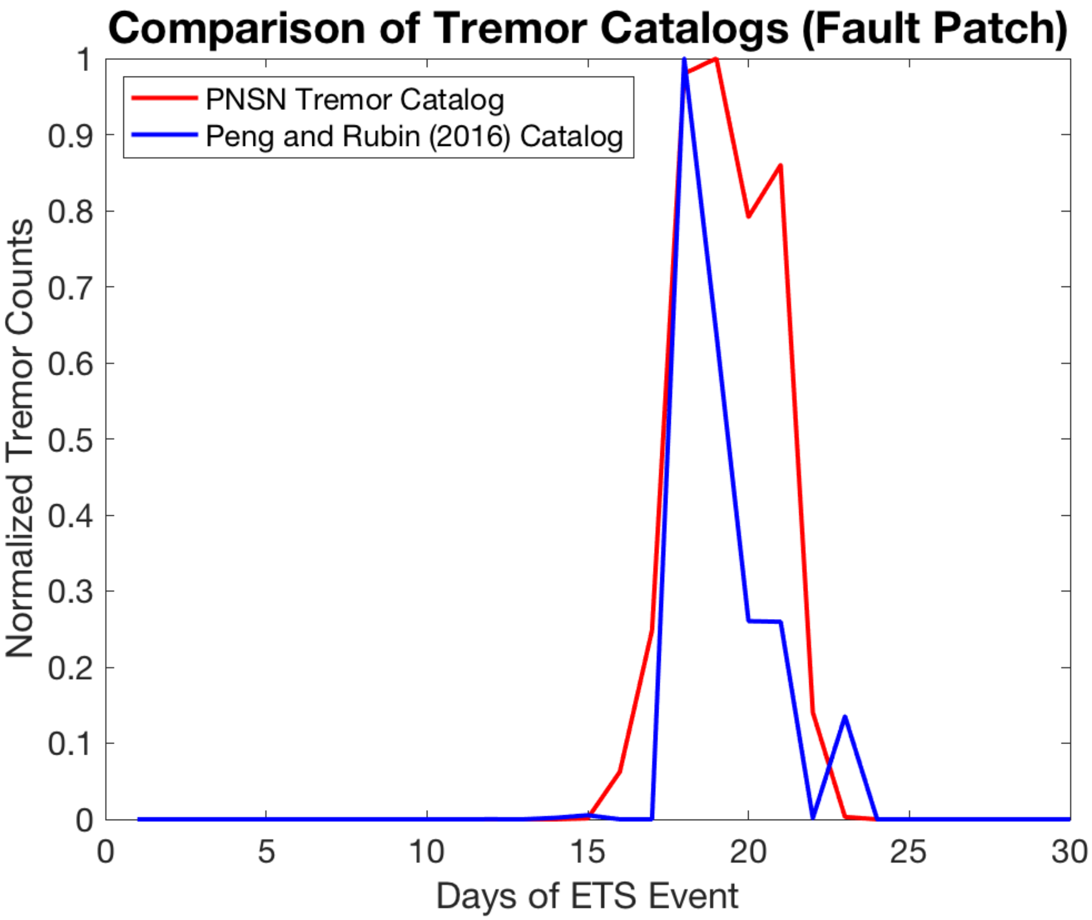

Figure A2.10: A plot of normalized tremor densities of the PNSN seismic network catalog (red) and the Peng & Rubin (2016) catalog (blue) for a given 8 km x 8 km fault patch based on the McCrory et al., (2012) fault model (black square in Figure A2.9). We chose to normalize the catalogs because the Peng and Rubin Catalog has significantly more detections due to its use of the high-density array of arrays. However, the peaks of the two catalogs are well aligned in the timing of tremor activity.

APPENDIX 3: SUPPLEMENTARY MATERIALS FOR CHAPTER 4

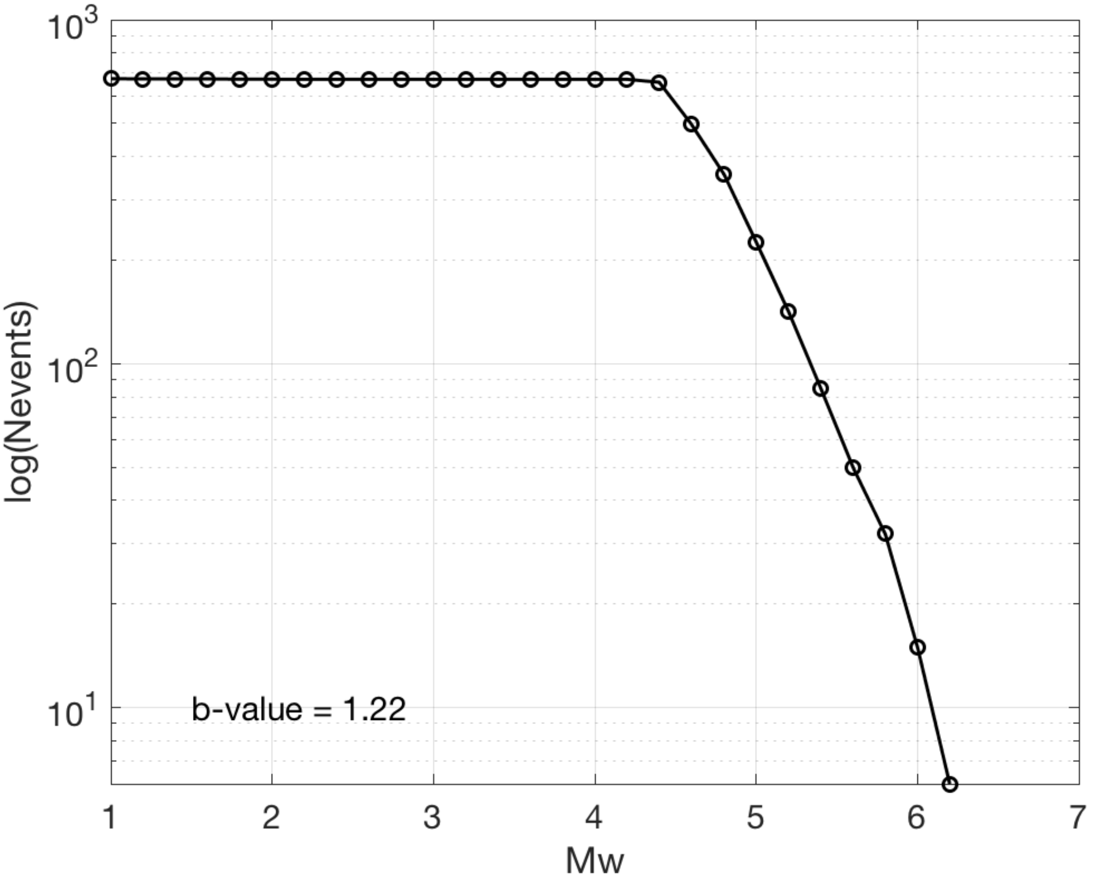

Figure A3.1: A plot of the cumulative number of events greater than a given magnitude for our scaled clustered tremor catalog. All Mw's are calculated using a scaled slip distribution based on the tremor distribution and a value of 30 GPa for the shear modulus. Based on this figure we estimate a b-value of 1.04, which is similar to b-values of typical earthquakes, and we infer that our catalog is complete down to ~Mw 4.3.

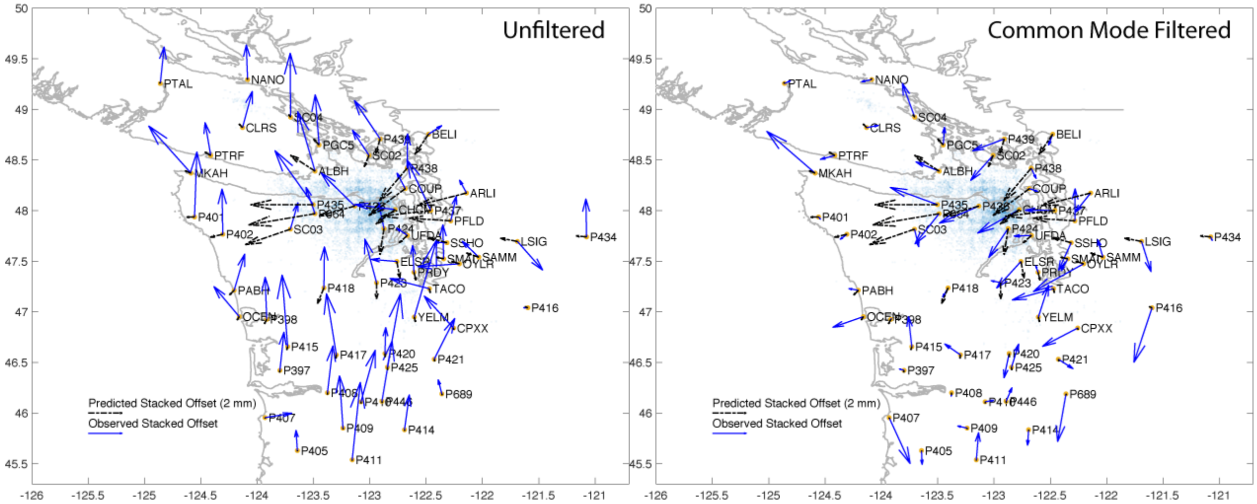

Figure A3.2: Effect of the common-mode signal. A comparison of the stacked displacements for the 7 events in Patch 5. The unfiltered time series (left) shows a strong northward signal across all stations, as compared to the displacements with the common-mode removed(right).

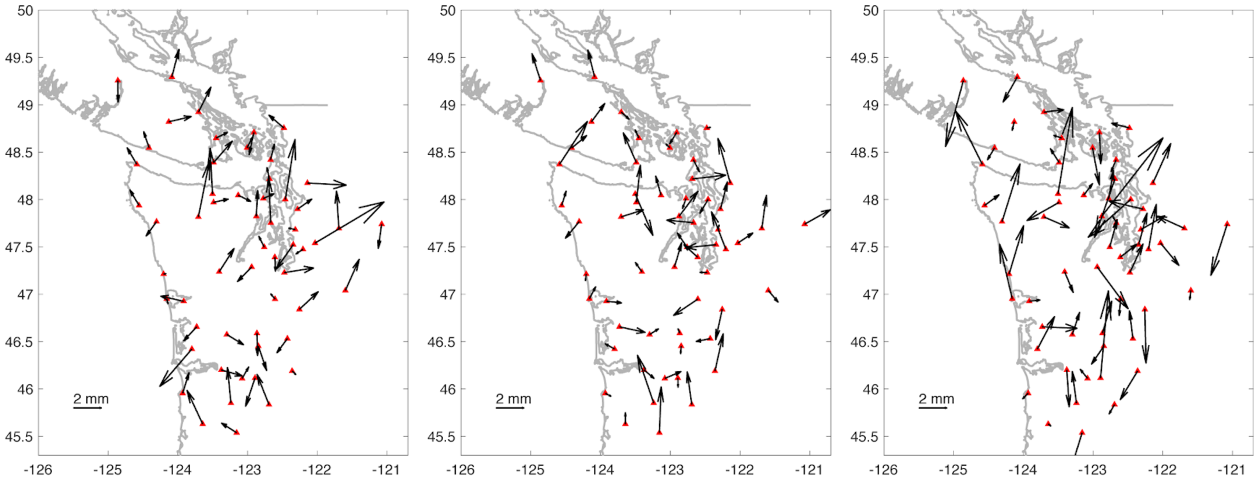

Figure A3.3: Three realizations of stacking GPS time series from seven random time windows from 2009 -2016, each 34 days in length, based on the method outlined in the main text. The same PANGA stations are shown in each panel (red triangles). As we would expect, none of the inferred offsets from these realizations show any coherent signal, unlike the inferred offsets based on the tremor-aligned stacks (Figures 4.5 and 4.6).

YEARS	FULL MOMENT	SLIP CASE
2010	5.00E+08	4.44E+08
2011	9.36E+08	3.47E+08
2012	5.02E+08	3.26E+08
2016	1.63E+09	5.25E+08

Table A3.1: A table of the scaling factors in (Nm per 5-minute tremor detection) for four large SSEs (August 2010, August 2011, September 2012, December 2015). The methods for determining these scale factors are outlined in the main text.

VITA

Kelley Hall was born and raised in Seattle, WA. She received her Bachelors in Geology-Physics combined with a Mathematics minor from Whitman College in 2013. She is passionate about using mathematics and physics to further our understanding of the natural world. This led her to pursue a PhD in geophysics, focusing on slow earthquakes in the Cascadia subduction zone. During her PhD, she also played for and coached the University of Washington Women's Ultimate Frisbee Team, Element.